Research Highlights

CHEMIN: A Miniaturized X-ray Diffraction and X-ray Fluorescence Instrument

D. L. Bish (bish@lanl.gov), S. J. Chipera, and D. T. Vaniman (EES-6)

Approximately 100 elements exist in our universe, and these elements can combine to form at least 3,800 minerals (naturally formed crystals). Using chemical analysis, one can identify the elements in a material, but most often, this method cannot be used to identify the crystalline structure, which can be crucial for establishing the properties of a mineral or synthetic crystal. In addition, knowing which minerals are present in a sample can help determine the mineral's alteration history. In this article, we will discuss CHEMIN, a prototype miniature instrument we developed that can identify both the CHEMistry and MINeralogy (crystalline structure) of a sample.

CHEMIN was originally developed for space travel to Mars and is the first miniature instrument to perform these two identifications using both x-ray diffraction (XRD) and x-ray fluorescence (XRF) analysis. In 1999, we received an R&D 100 award for the CHEMIN instrument. Its potential uses extend far beyond Mars to many applications on Earth, including portable field instruments, robots that analyze contaminants in hazardous areas, and machines that perform on-line analyses of solid phases in production facilities.

History

Geoscientists in EES Division have been interested in miniaturized XRD/XRF instrumentation since 1990. Early in the decade, research in our division focused on both isotopic and tube-source instruments, as well as a variety of detector systems integrated in an instrument that passed x-rays through a sample (transmission geometry) rather than diffracting them off the sample (reflection geometry). At this time, we are improving CHEMIN as a potential flight instrument for the exploration of extraterrestrial bodies.

Space Exploration

The origins and histories of planetary, asteroidal, and cometary bodies are reflected in their constituent minerals. This tremendous variety of mineralogy carries stories of pressure, temperature, oxygen fugacity, and solution chemistry, all intertwined with histories of sedimentation, igneous activity, metamorphism, impacts, and surface weathering. The science objectives of determining simultaneous chemistry and mineralogy thus span the full history of planetary, asteroidal, and cometary formation and evolution.

Fegley et al. suggested in 1992 that the CHEMIN concept could be a valuable means to resolve mineralogic uncertainties for Venus. More recently, it was pointed out by Rietmeijer that to perform successful in situ study of an active comet nucleus, one must use an instrument like CHEMIN for unambiguous mineral identification.

The CHEMIN Instrument

CHEMIN is a miniaturized, simultaneous-XRD/XRF instrument based on a charge-coupled device

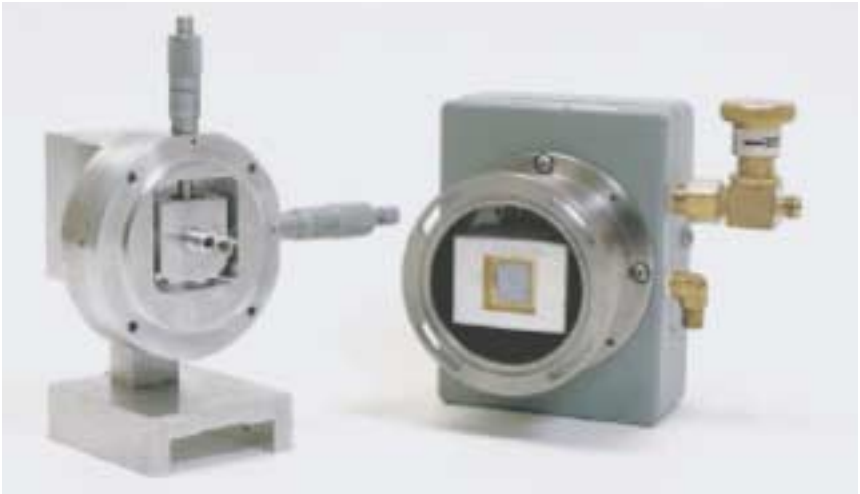

Figure 1. CHEMIN Instrument.
The prototype with collimator and sample holder on the left and charge-coupled device (CCD) on the right.

(CCD) that exists in prototype form (Figure 1). The intrument is designed to characterize elemental composition and mineralogy from small fine-grained or powder samples.

We have obtained usable diffraction data from the instrument in only a few minutes, and we predict that a flight instrument should be able to collect data in 1 to 2 hours. CHEMIN discriminates between diffracted and fluoresced x-rays by operating the CCD in what is known as "single-photon-counting" mode, with photons of the x-ray tube characteristic energy (e.g., Cu Kα or Cu Kβ) ascribed to diffraction events. The instrument is operated in this mode by exposing the CCD detector to repeated short bursts of x-rays. When using short exposure times (~10 to 60 s), ideally no more than one photon strikes each pixel (or picture element) of the 512 × 512 pixel CCD. Under these conditions, the charge deposited in each pixel is proportional to the energy of the x-ray photon striking the pixel, providing the option to analyze the photon energy on a pixel-by-pixel basis.

CHEMIN distinguishes between diffracted characteristic photons and fluorescence photons based on the fact that diffracted photons have the characteristic energy of the incident x-rays whereas fluorescence x-rays are characteristic of the sample chemistry and have different energies (Figure 2).

The XRD data, which are measured in transmission geometry, yield concentric rings on the CCD detector (Figure 2), providing information on phase structure. The XRF signals strike the CCD uniformly across the detector and can be combined to provide elemental information. The CCD detector in our current design is encased in an instrument measuring 15 × 12 × 22 cm. A flight instrument would weigh less than 1 kg, have a volume of 500 cm^3, and have power requirements of 2 W.

Figure 3 shows the spatial relationships between components in existing CHEMIN instruments. The advanced CHEMIN instrument, capable of operating in space or remotely on earth is illustrated in Figure 4. It is can be described as a series of subsystems: (1) an x-ray tube source, (2) a sample-manipulation system, and (3) a CCD detector that simultaneously records both energy and position of x-rays on the two-dimensional CCD detector.

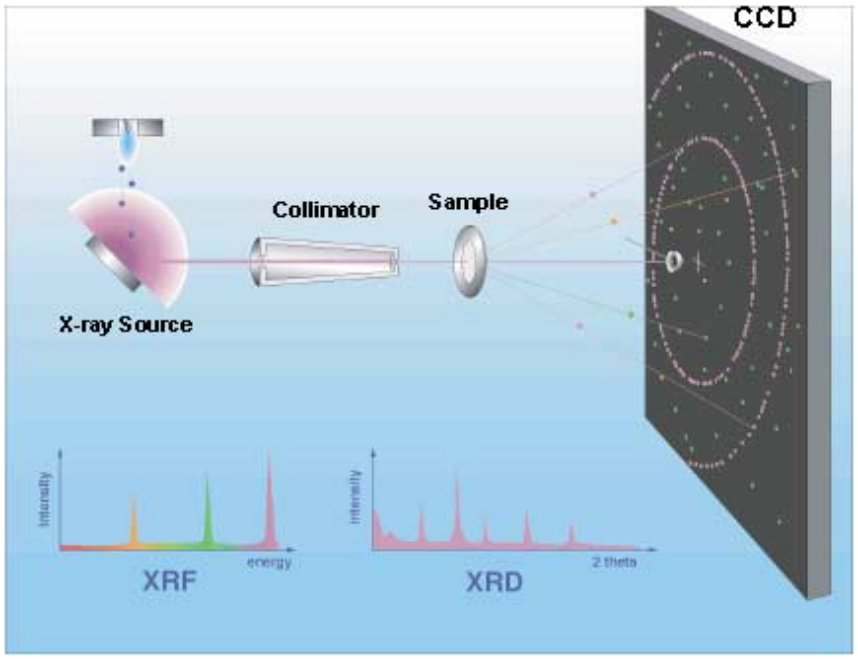

Figure 2. Generation and Measurement of X-ray Diffraction and Fluorescence Signals from a Single Sample.
X-rays impinging on the CCD detector are indicated by colored dots, and their energy distribution is shown at the bottom in the XRF spectrum. The violet dots indicate the diffracted x-rays that are characteristic of the x-ray source and, hence, diffracted from the sample. Dots of other colors do not fall in a fixed pattern and represent x-rays fluoresced from various elements within the sample. Note that the violet dots fall in a pattern of concentric circles, the position of which is reflective of the crystal structure of the sample. The two-dimensional XRD pattern at the bottom, obtained by circumferential integration of the violet rings, corresponds to a conventional XRD pattern.

Field-Emission X-ray Tube. At present, a standard laboratory x-ray tube is used with CHEMIN. The x-ray source component is shown as a standard tube in Figure 3. For a flight instrument, we propose using a sealed, high-vacuum envelope housing a micromachined-field-emitter (MMFE) array, an electrostatic focusing element, and an anode, onto which a small focused beam of electrons is accelerated. The MMFE concept has already been used successfully in devices such as flat-panel color monitors. In operating mode, a continuous electrostatic potential of 20 keV is applied between the anode and the MMFE array, and an electron current is created by impressing a potential of ~50 V on the extraction anode of the MMFE array.

Sample-Manipulation System. Mechanical handling of rock, soil, and ice samples is one of the more difficult problems in robotic analysis of extraterrestrial bodies. Both eolian dusts and soils can be collected easily and analyzed without extensive processing; however, to analyze solid geologic media fully, one will almost always require a method to obtain the geologic media

in powder form. We are considering two methods for obtaining powders: piezoelectric microdrilling and explosive powdering systems. Both methods have been developed and have prototype systems available that can be tested against a variety of target lithologies.

CCD Detector Array. The third component and the heart of CHEMIN is the CCD detector array and electronics. The ideal CCD would be based on the CUBIC (cosmic undefined background instrument with CCDs) detector built and flown by the Jet Propulsion Laboratory in their x-ray astronomy studies. The array in the planned instrument consists of a matrix of 1024×1024 pixels in a front-illuminated CCD. Important characteristics of the device are listed in Tables 1 and 2. In most applications, CHEMIN can be operated in shaded or in local nighttime Martian conditions, when the ambient temperature is sufficiently low to reduce background to an acceptable level without any additional cooling.

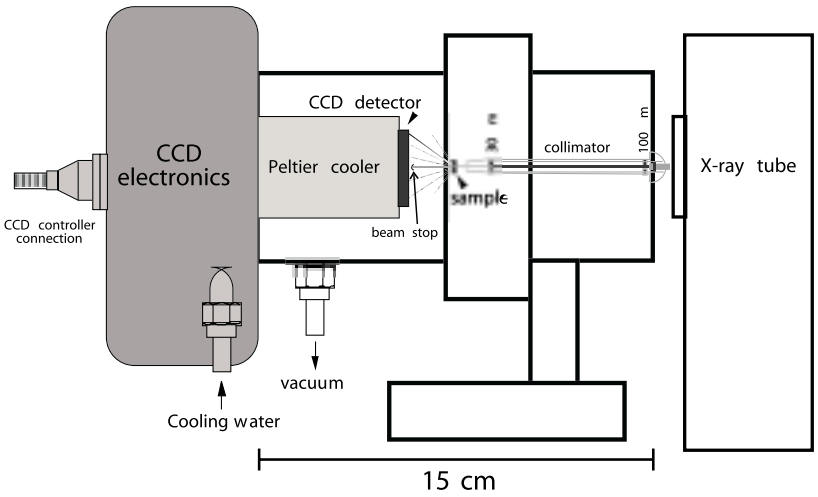

Figure 3. Prototype CHEMIN. Schematic of the existing instrument.

Data Collection and Analysis

During data collection, a collimated x-ray beam strikes a thin-film substrate sample holder held in the second component of the system, which is a multiposition sample carousel. The carousel disc is the only moving part in the CHEMIN instrument. The carousel can be precisely and continuously rotated 360° by a stepper motor. The substrates are x-ray-thin (~2 μm) Mylar films made sticky on the top surface by a thin film of vacuum grease or the like. A protective cover is removed from the greased Mylar as it advances into the sample collection port. A sample is dumped into the sample collection port, and powder adheres to the sticky surface of the Mylar, whereas excess powder and larger grains roll off the inclined substrate. The carousel is then rotated into position for analysis between the x-ray source and the CCD detector array. While in the position for analysis, 50-μm diameter regions are illuminated by the collimated x-ray beam. Approximately 50 exposures are collected of each area, after which the motor steps ~100 μm so that a new area of sample material on the same substrate is analyzed. An "exposure" is made by providing a pulse of 50 V to the extraction anode of the x-ray tube, flooding the CCD with diffracted and fluoresced x-ray photons. As we already mentioned, the CCD is operated in single-photon counting mode to measure both diffraction and fluorescence data simultaneously.

Figure 5 illustrates the flat-plate diffraction data obtained for Al_2O_3 from CHEMIN, before circumferential integration. CHEMIN's diffraction methodology is particularly good with poorly prepared samples such as natural dusts or soils. The advantage of the CHEMIN geometry is illustrated in Figure 6, which

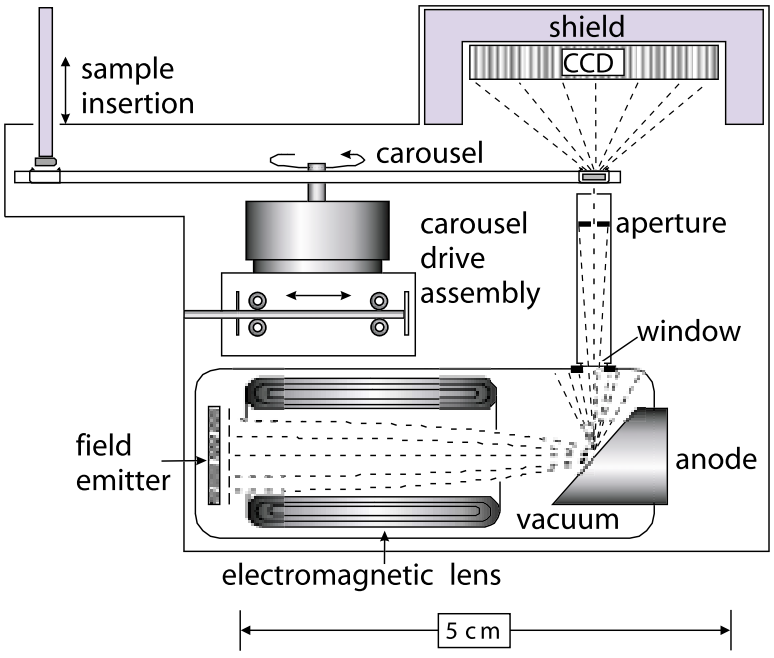

Figure 4. Advanced CHEMIN.
Schematic of the proposed advanced CHEMIN instrument showing the spatial relationships among the three components that are critical to the operation of CHEMIN.

Table 1. Characteristics of the Proposed CHEMIN CCD

Format	1024 x 1024
Pixel size (μm)	18
Number of readout channels	4
Readout noise, e^- (rms)	0.5

Energy (eV)	Quantum Efficiency	Energy Resolution (FWHM) (eV)
277	0.15	38
1000	0.70	60
5400	0.15	115
8000	0.05	130

Table 2. Overall Instrument Parameters for Proposed CHEMIN

Detector	X-ray sensitive (thin polygate) CCD
X-ray tube electron source	Field-effect emitter array
Range (degrees 2θ)	5 to 55°
Diffraction resolution	<0.2° 2θ
Mass (kg)	0.8
Power (W)	2.0

shows a CHEMIN XRD pattern of aragonite at the top. CHEMIN accumulates part or all of the Debye rings out to about 50° 2θ (Cu Kα). Circumferential integration of each ring compensates for poor powder preparation (i.e., spotty Debye rings), such as might be produced by robotic sampling systems. Simulations of conventional diffractometer data (stippled line) and Debye-Scherrer film data are shown at the bottom of Figure 6, illustrating the loss of diffraction signal averaging that can take place when the full Debye rings are not used.

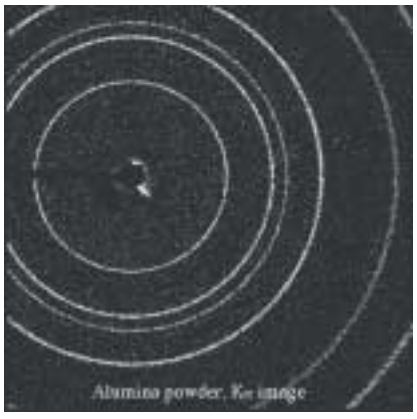

Figure 5. Flat-plate Diffraction.
Data for Al_2O_3 (corundum) obtained using the prototype CHEMIN instrument.

Further data processing using circumferential integration produces a diffraction pattern like that shown in Figure 7, which illustrates a comparison between the CHEMIN diffraction pattern of quartz and the pattern obtained on a conventional laboratory diffractometer. XRF data

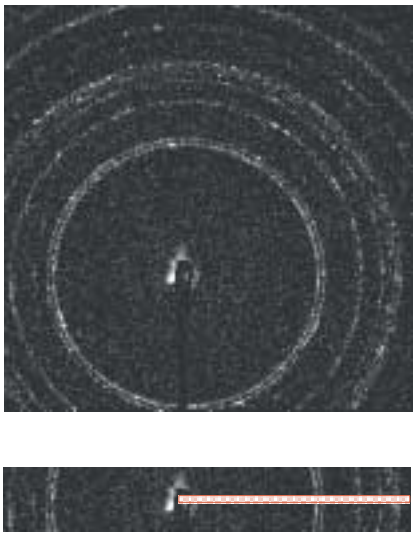

Figure 6. Comparison of Techniques.
The figure shows relative amounts of diffraction data for aragonite resulting from CHEMIN (upper square), a Debye-Scherrer camera (lower strip), and a conventional laboratory diffractometer (stippled red region).

as well as XRD data are collected even with the test CCD in CHEMIN at the Los Alamos National Laboratory, although XRF data of higher quality are obtained with the CUBIC CCD at the Jet Propulsion Laboratory. An example of an XRF spectrum measured on aragonite, $CaCO_3$, is shown in Figure 8. The spectrum is remarkable in the presence of the C and O lines, in addition to Ca; Cu and Al arise from the sample holder. Conventional x-ray fluorescence instruments are typically incapable of detecting C and O x-rays.

Advantages of CHEMIN

In Table 3, we compare two XRD analyses with a normative calculation for a terrestrial basalt sample. We obtained one of the XRD analyses with the prototype CHEMIN instrument (Figures 1 and 3); the other we obtained with a Siemens laboratory diffractometer. Although the CHEMIN analysis has poorer peak resolution, the data we obtained are sufficient not only to determine the mineral phases present but also to apply Rietveld analysis to estimate the relative proportions of mineral phases in the sample. (Rietveld analysis involves calculating a model diffraction pattern based on the crystal structures of the known phases in a mixture. The quality of fit between the observed and calculated diffraction patterns is then improved using a least-squares process in which relative amounts of each phase and the crystal structural parameters are varied.)

We have developed software to combine both the chemical XRF data and the XRD data to perform this operation more rigorously. The analysis represented in Figure 9 uses only the XRD data. The goodness of fit for a Rietveld analysis of the XRD data is usually expressed using statistical parameters but can also be visualized as a difference pattern, shown at the bottom of Figure 9.

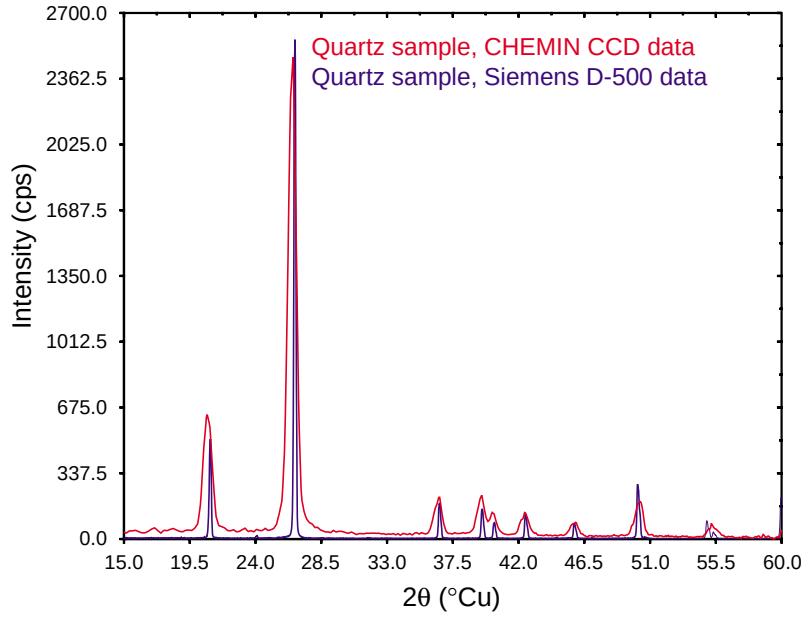

Figure 7. Quartz Diffraction.
Diffraction pattern of quartz from circumferential integration of flat-plate CHEMIN data (red) compared with pattern from a conventional laboratory diffractometer (blue).

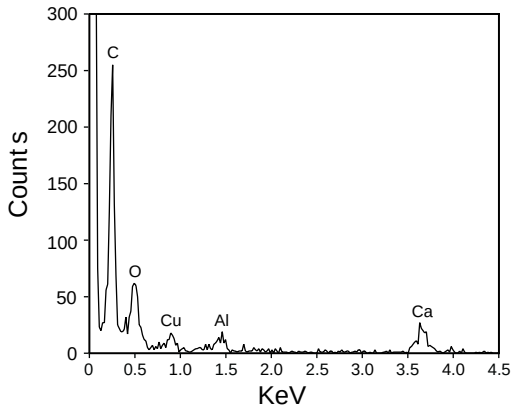

Figure 8. Aragonite X-ray Fluorescence.
The XRF spectrum of aragonite, $CaCO_3$, measured with the CUBIC CCD, which shows the presence of the carbon and oxygen lines.

To find the weight proportions of the minerals that best match the measured XRD data, we must vary the ratios in which the calculated minerals are mixed to reproduce the observed crystal pattern. These weight proportions are listed in Table 3, calculated for both the CHEMIN XRD pattern as shown in Figure 9 and for XRD data from the same sample collected on a laboratory diffractometer. The errors listed are calculated statistical errors of approximately 2θ. Note that the relative error varies not only with mineral abundance but also with mineral type.

Clearly some mineral abundances can be more precisely measured than others. For example, the feldspars are complicated by ternary cation exchange (Ca, Na, K) and associated framework Al/Si ratio variations. In addition, in high-alumina basalts such as this sample, they also form as phenocryst and groundmass phases, with separate exsolution histories, which results in superposed complex mixtures of high- and low-temperature structural types. Although this makes the feldspar calculations more error prone and, in this sample, of greater abundance than should be present (compare the calculated normative value in Table 3), in fact, the complexity of the pattern indicates a wealth of information.

It should also be noted that, in some respects, the Rietveld data are more accurate than a normative calculation. The normative calculation is exceptionally sensitive to SiO_2 content, and the norm shown in the third column of Table 3 reports less olivine and more oxide minerals than the sample petrography allows. This discrepancy reflects the magnitude of the errors commonly associated with instrumental determinations of SiO_2 content in rock samples. In this instance, the Rietveld determinations of mineral abundance are likely closer to reality. The XRD-based analysis also identifies phlogopite, which is not recognized in the normative calculation, and it does not assume spurious occurrences of ilmenite and hematite.

Conclusions

Our prototype CHEMIN instrument, which has been in operation since July 1996, has confirmed the principle of CCD-based simultaneous XRD and XRF. Unfortunately, some of the components in this prototype do not allow CHEMIN's full capabilities to be realized as they would be with an optimized instrument. Nevertheless, using CHEMIN, we have been able to detect and quantify minerals at abundances as low as 1%, as well as to provide quantitative chemistry and mineralogy from complex mixtures (Table 3). We have tested this instrument with numerous pure minerals and mineral mixtures to examine its potential in mineralogic characterization of extraterrestrial bodies. We have applied Rietveld refinement methods to XRD data to determine unit-cell parameters and quantitative phase information from <1-mg-sized samples. Combining Rietveld quantitative mineralogical analyses and XRF data on a single sample has the potential to provide accurate mineralogical data for remote or extraterrestrial samples. For example, such diffraction data would remove the ambiguity regarding the mineralogy of the Martian surface that results from the availability of chemical information only. ■

Table 3. Rietveld Analyses of Basalt Using XRD Data from CHEMIN and a Laboratory Diffractometer Compared with a Normative Calculation (all data in weight percent; statistical error of ~2σ in parentheses)

	CHEMIN	Laboratory Diffractometer	Normative Calculation
forsterite	7.5 (3.0)	9.3 (2.0)	2.7
albite	28.09 (7.0)	22.2 (5.0)	35.2
anorthite	17.5 (5.0)	27.3 (3.0)	20.7
sanidine	37.9 (8.0)	28.8 (6.0)	17.5
augite	4.7 (2.0)	9.3 (2.0)	10.5
magnetite	1.9 (1.0)	1.1 (1.0)	3.3
ilmenite	—	—	3.4
hematite	—	—	4.2
fluorapatite	1.6 (1.0)	2.1 (1.0)	2.3
phlogopite	0.1 (0.1)	0.1 (0.1)	—

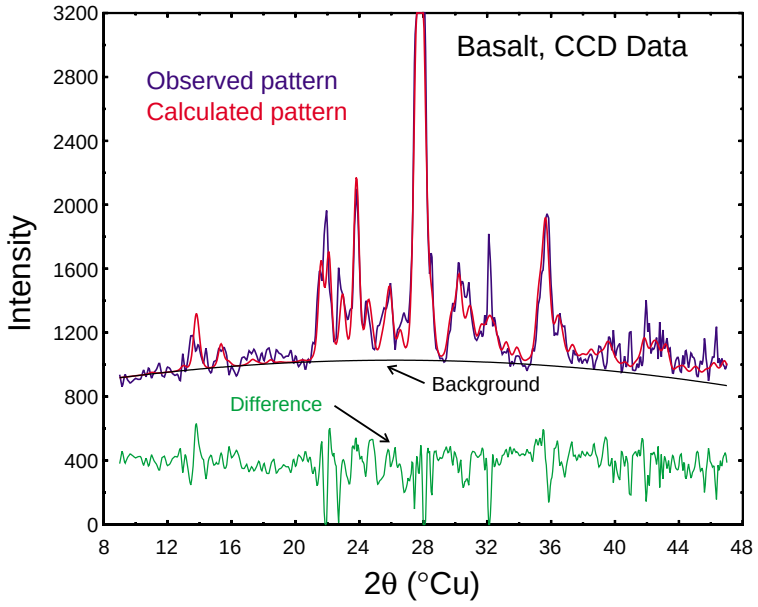

Figure 9. Rietveld Refinement of Basalt Diffraction Using CHEMIN. Observed diffraction data are blue, the pattern calculated based on the crystal structures of the component minerals is red, the difference between the calculated and observed patterns is green, and the calculated background is black.

Further Reading

Bish, D. L., and J. E. Post. 1989. *Modern Powder Diffraction*. *Reviews in Mineralogy*, vol. 20, 369 pp. Washington, D.C.: Mineralogical Society of America.

Bish, D. L., and J. E. Post. 1993. Quantitative mineralogical analysis using the Rietveld full-pattern fitting method. *American Mineralogist* **78**: 932–942.

Blake, D. F., et al. 1992a. Design of an x-ray diffraction/x-ray fluorescence instrument for planetary applications. *Lunar and Planetary Science Conference* **XXIII**: 117–118.

Blake, D. F., et al. 1992b. CHEMIN: Chemical and mineralogical analysis for planetary exploration using combined x-ray fluorescence and x-ray diffraction. *Discovery Mission Workshop, San Juan Capistrano, CA.*

Blake, D. F., et al. 1993. X-ray diffraction apparatus. U.S. Patent No. 5,491,738.

Blake, D. F., et al. 1994. A mineralogical instrument for planetary applications. *Lunar and Planetary Science Conference* **XXV**: 121–122.

Clark, B. C., and D. C. VanHart. 1981. The salts of Mars. *Icarus* **45**: 370–378.

Fegley, B., Jr., A. H. Treiman, and V. L. Sharpton. 1992. Venus surface mineralogy: Observational and theoretical constraints. *Proceedings of Lunar and Planetary Science* **22**: 3–19.

Kraft, R. P. 1994. Soft x-ray spectroscopy using charge-coupled devices with thin poly gates and floating gate output amplifiers. *Proceedings of SPIE—The International Society for Optical Engineering* **2280**.

Rietmeijer, F. J. M. 2000. What we can expect to learn from robotic exploration of a comet nucleus surface. In *Space 2000, Proceedings of the Conference, American Society of Civil Engineers, February 27-March 2, 2000, Albuquerque, New Mexico*, pp. 695–702.

Spindt, C. A. 1992. Microfabricated field-emission and field-ionization sources. *Surface Science* **266**: 145–154.

Vaniman, D. T., et al. 1991a. Integrated XRD and XRF data from a single instrument for planetary surface exploration. *Clay Minerals Society 28th Annual Meeting* 157.

Vaniman, D. T., et al. 1991b. In-situ planetary surface analyses: The potential of x-ray diffraction with simultaneous x-ray fluorescence. *Lunar and Planetary Science* **XXII**: 1429–1430.

Vaniman, D. T., D. Bish, D. Blake, S. A. Collins, P. Sarrazin, S. T. Elliott, and S. Chipera. 1998. Landed XRD/XRF analysis of prime targets in the search for past or present Martian life. *Journal of Geophysical Research, Planets* **103**: 31, 477–431, 490.

A Geoscience Approach to Rock-Solid Concrete

G. D. Guthrie (gguthrie@lanl.gov) and J. W. Carey (EES-6)

Concrete, a composite of sand and gravel bound by hydrated cement, is one of the most used construction materials, worldwide. Concrete is used so extensively because it is easy to produce, has high compressive strength, and is durable, which makes it economical in the long term. The quality of durability can be significantly compromised by a number of physical and chemical processes, leading to premature degradation of a concrete structure. When concrete degrades prematurely, the cost of a structure will increase dramatically, and the degraded concrete can pose safety and environmental risks as well. Hence, increasing the durability of concrete is a critical concern in applications ranging from the transportation infrastructure to the isolation of hazardous and radioactive waste and as it turns out, improving the durability of cement-based composites will help with the atmospheric carbon-dioxide (CO_2) problem.

An important, though indirect, consequence of premature concrete degradation is the unnecessary emission of CO_2. Cement production is the largest industrial source of atmospheric CO_2 that is not associated with energy production. Figure 1, a photo of a cement plant in Tijeras, New Mexico, shows the stacks from which the CO_2 is emitted into the atmosphere.

Despite the long history of the use of concrete, a mechanistic approach (that is, understanding the entire cement/aggregate system) to control durability has remained elusive. Instead, a prescriptive approach has been used; prescriptions (specifications) have been based on a combination of field experience and laboratory experiments, both of which are limited with respect to duration, properties of the materials, environmental factors, and other variables that affect durability.

In contrast, a mechanistic approach to designing cement-based composites would rely on predicting the physical and chemical evolution of a concrete mix placed in a particular environment. Such an approach has often been viewed as unachievable, given the chemical and structural complexity of a cement-based composite. However, the two primary barriers to this goal (computational and theoretical) are not insurmountable. Recent advances in computational power and methods (e.g., dual-continuum codes for modeling reactive transport in matrix and fractures) have removed these barriers to predicting the evolution of a concrete structure as it interacts with its environment. The theoretical barrier can be lowered by borrowing tools and approaches used in the geosciences, where they have addressed similar complexities in a mechanistic way.

For example, in many respects, the chemical and physical evolution of a cement-based composite resembles what occurs in natural environments. Most of the materials in a composite like concrete are either earth materials or derived from earth materials. Likewise, the processes that occur during cement hydration or that occur as the composite interacts with its environment can also be directly related to geological analogs. Hence, the methods used to describe geological materials and processes at a fundamental level may prove useful in laying the foundation for a mechanistic approach to concrete evolution.

This concept is the basis for our initiative to develop a geochemical model of the evolution of cement-based composites. The model would allow the prediction of how a concrete mix performs in a particular environment. In other words, one could optimize a mix design prior to placement. En route to this model, we have been developing a number of geochemical and geophysical methods for characterizing cement-based composites. One of our methods, ASR Detect™, recently received an R&D 100 Award.

Alkali-Silica Reaction

One of the leading causes of premature degradation in concrete worldwide is the alkali-silica reaction (ASR) between alkali cations, hydroxide anions, and siliceous aggregates. In this reaction, silica dissolves in the high-pH pore fluids and precipitates as a gel along fractures, in voids, and around reactive aggregates in the concrete. Although this phenomenon has been recognized in degrading concrete for over 60 years, ASR remains poorly understood, and the problems it causes have been handled primarily using prescriptions that have been known for decades, which are to minimize the alkali content of the cement and avoid reactive aggregates. These prescriptions are not always successful, and ASR-plagued concrete continues to be produced today (Figure 2). Furthermore, low alkali levels in cement are difficult to achieve in some regions, particularly in light of new regulations that have led to the re-incorporation of alkali-

rich dusts trapped from the exit gases of a kiln. In addition, nonreactive aggregates are not always locally available, and this deficiency will become more of a problem as quality aggregates become depleted.

Several recent treatments offer promise for inhibiting ASR in new structures and even slowing the progression of ASR in existing structures. For example, lithium salts used as admixtures at appropriate levels in a concrete mix appear to inhibit ASR, and soaking a structure with an aqueous solution of lithium may arrest degradation.

The Geochemistry of ASR

In the field, ASR is conspicuous because it causes a network of surface fractures that are often filled with a white precipitate. The interior of a structure suffering from extensive ASR is also riddled with fractures, along which white precipitate can be seen associated with some aggregates and filling some voids. Unfortunately, these characteristics are not unique to ASR, so a diagnosis typically requires a time-consuming petrographic analysis (for example, verifying the presence of an isotropic gel). Ideally, one would like to diagnose ASR in the field, which would allow the causes of degradation to be determined more rapidly and would allow a better evaluation of the distribution of ASR within a structure at a hand-sample scale.

We recently developed a geochemical staining method for detecting ASR gel in a hand sample. Our method, ASR Detect™, makes use of the physical and chemical properties of the primary reaction product (an alkali-rich gel). The staining method is designed to tag regions containing exchangeable potassium.

Gel produced by ASR is typically enriched in both sodium and potassium, which are believed to originate largely from the cement. Most cements have potassium as their dominant alkali contaminant so ASR gels often have more potassium than sodium. In our observations of ASR gels (primarily in samples from New Mexico), potassium is always the dominant alkali cation. This exchangeable potassium can be used as a marker for ASR gel by staining with a saturated solution of sodium cobaltinitrite. When such a solution contacts ASR gel, exchangeable potassium from the gel reacts with the solution to form a yellow precipitate [$K_2NaCo(NO_2)_6 \cdot 6H_2O$]. This method has also been used in the

Figure 1. Industrial Source of CO_2.
Cement kilns are the largest nonenergy source for anthropogenic CO_2 emissions, producing about a ton of CO_2 for each ton of cement clinker.

Figure 2. An ASR Problem.
The underside of an ASR-plagued bridge on I-25 in New Mexico. The 35- to 40-year-old bridge was made using low-alkali cement, yet ASR appeared rapidly in the bridge deck, which has since undergone expensive resurfacing operations.

geological sciences for staining potassium feldspars that have been etched in hydrofluoric acid. For ASR gel, sodium cobaltinitrite solution is allowed to react directly with the concrete surface without any acid-etching step.

In addition to providing a means for rapid ASR identification in the field, using ASR Detect™ has enabled new insights into the geochemical development of ASR. As can be seen in the stained samples, ASR exhibits a characteristic progression from the initial formation of a potassium-rich gel located within some aggregates and voids to a latter migration and ion exchange to form gels with lower K/Ca ratios that have a more widespread distribution.

This chemical heterogeneity can be seen at a micrometer scale using scanning electron microscopy, and the staining allows the process to be followed at the hand-sample scale.

The heterogeneity of ASR is likely tied to the innate spatial variability of concrete. Heterogeneous microenvironments develop along fractures in a concrete due to the chemical differences between the hydrating Ca-Si paste (pH > 12.5) and the aggregates (often siliceous aggregates that can buffer the local pH at significantly lower values).

We are using this concept of microenvironments as the basis for our geochemical model for ASR.

The Biogeochemistry of ASR

The unique geochemistry of the concrete microenvironments we identified led us to consider whether microbial activity may play a role in ASR. Traditionally, ASR has been viewed as an inorganic process involving the enhanced dissolution of metastable silica (for example, opal, silica glass, and strained quartz) in a high-pH, alkali-rich solution. Hence, the aggregates around which gel was found were termed “reactive aggregates” and viewed as sources of the silica gel. In our model, these aggregates function as geochemical microenvironments in which the pH may be lowered by acidic mineral surfaces and by mineral dissolution, causing the silica to precipitate. One consequence of this view is that these microenvironments might provide suitable environments for microbial activity, which often is not optimized at the higher pH of the cement paste. We have investigated this hypothesis with a combination of stable isotopic analysis and biogeochemical staining.

Figure 3 shows values for $\delta^{13}C/^{12}C$ and $\delta^{18}O/^{16}O$ from a variety of locations within a degrading concrete system. Shown in triangles and circles are the values measured from two materials actively precipitating at the bottom of a concrete bridge deck (calcite stalactites and thermonatrite efflorescence, respectively). The isotopic ratios in these materials show a marked depletion along a trend with a slope of ~2. This trend results from a kinetic fractionation caused by the high pH of the precipitating fluids. In contrast to precipitation in caves (in which degassing causes stalactite growth), precipitation of the calcite and thermonatrite results from diffusion of atmospheric CO_2 into the high-pH fluids. These materials define the “inorganic” isotopic trend in this system. The squares in the graph show the ratios measured for samples of gel along fractures within the bridge deck. These isotopic ratios cannot be explained by the inorganic kinetic trend, because their carbon signature is even more depleted. This depletion is believed to reflect an additional (highly depleted) source of CO_2 caused by microbial degradation of organics.

We confirmed this hypothesis by combining geochemical staining (to show the distribution of ASR gel) with a biological staining method (to show the distribution of protein). An

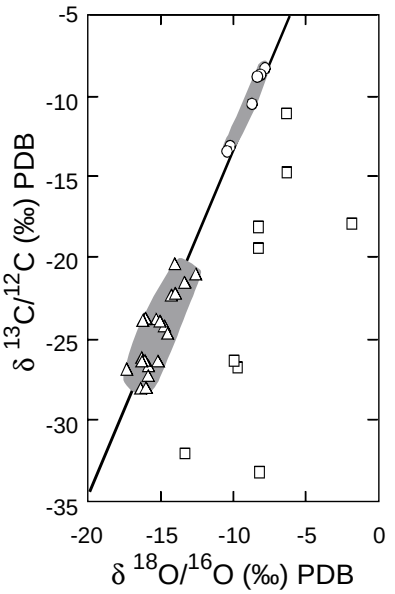

Figure 3. Isotopic Data.
The graph shows carbon and oxygen isotopic data from carbonates precipitated in the degrading concrete system.

example of this staining can be seen in Figures 4a and 4b. Ninhydrin is often used in microbiology to determine the presence of protein, which results in a purple stain. When stained with ninhydrin and ASR Detect™ (on opposites sides of a fracture), concrete from the structure studied isotopically shows protein accumulation in regions where K-rich ASR gel occurs. This protein accumulation is apparently due to a biofilm in these regions, as determined by scanning electron microscopy.

Given the association of microbial activity with ASR, one might wonder, “What role do microbes play in concrete degradation?” Microbial-induced degradation of concrete has been observed in concrete exposed to sewage. However, the type of degradation that we have observed appears to be quite distinct, with microbial activity restricted to specific microenvironments within the concrete. We plan to elucidate the role of microbes in ASR and to incorporate this role into a predictive model of concrete durability. ■

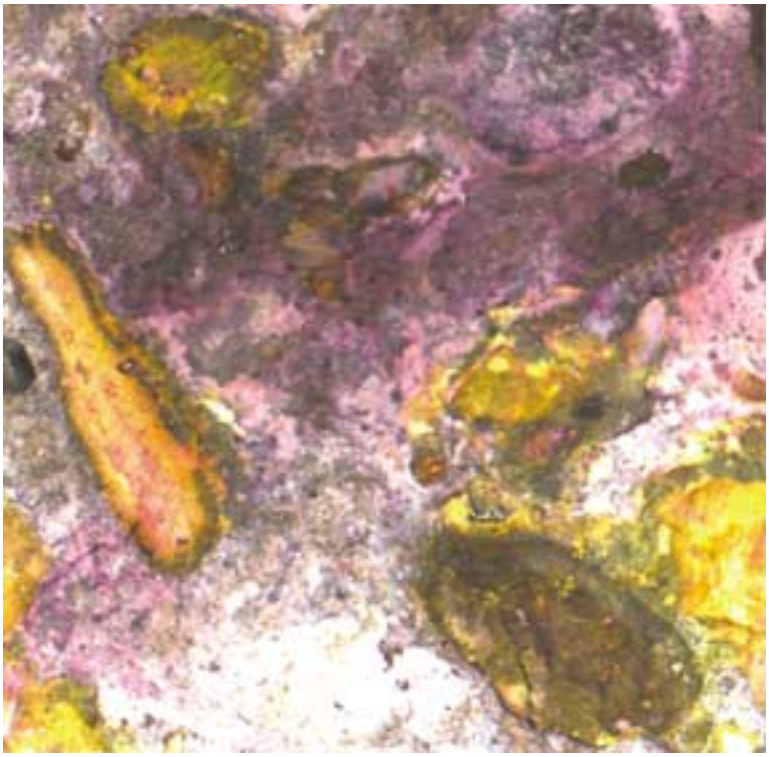

Figure 4a. ASR Detection.
Concrete fracture surface stained with ASR Detect to show characteristic yellow precipitate on ASR gel.

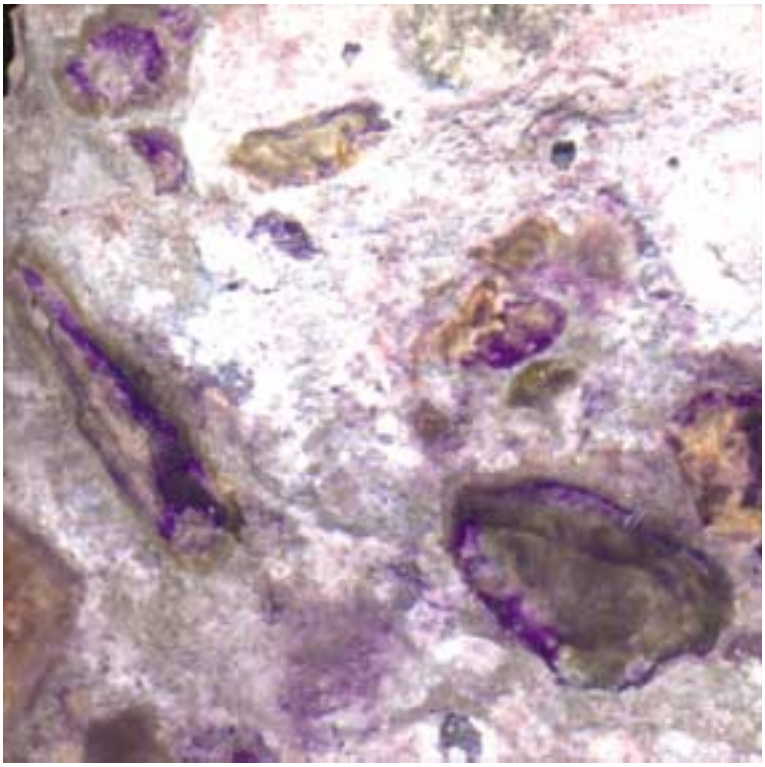

Figure 4b. Protein Detection.
The opposing concrete fracture surface stained with ninhydrin to show localization of protein. Note protein (dark purple) is localized in regions of ASR gel.

Further Reading

Davies, G., and R. E. Oberholster. 1988. Alkali-silica reaction products and their development. *Cement and Concrete Research* **18**: 621–635.

Guthrie, G. D., Jr., and J. W. Carey. 1997. A simple, environmentally friendly, and chemically specific method for the identification and evaluation of the alkali-silica reaction. *Cement and Concrete Research* **27**: 1407–1417.

Guthrie, G. D., Jr., and J. W. Carey. 1998. Detection of alkali-silica reaction swelling in concrete by staining. U.S. Patent No. 5,739,035.

Guthrie, G. D., Jr., and J. W. Carey. 1999a. A geochemical method for the identification of alkali-silica reaction. *TRB Record* **1668**: 68–71.

Guthrie, G. D., Jr., and J. W. Carey. 1999b. Detection of concrete deterioration by staining. U.S. Patent No. 5,955,372.

Lea, F. M. 1971. *The Chemistry of Cement and Concrete*, 3rd edition, p. 727. New York, NY: Chemical Publishing Company, Inc.

Natesaiyer, K. C., and K. C. Hover. 1989. Further study of an in situ identification method for alkali-silica reaction-products in concrete. *Cement and Concrete Research* **19**: 770–778.

Uncertainty and Upscaling in Porous Media Flow

D. Zhang (EES-6, dongzhang@lanl.gov) and W. E. Soll (EES-10)

Processes associated with fluid flow through porous rocks and sediments are at the core of problems in groundwater flow, contaminant migration, and petroleum production. A rigorous understanding of these processes is necessary to optimize our water resources, reduce environmental risk, and exploit fossil fuel most cost-effectively. Our objective is to develop partial differential equations for the moments of single- and two-phase fluid flow in heterogeneous porous media under realistic conditions as an alternative to the commonly used Monte Carlo simulation approach.

The workable moment equations have some important benefits over the traditional Monte Carlo approach. First, there are a small number of equations to be solved: one equation for the mean, and one each for a small number of variances and co-variances. Second, the coefficients of the equations, as averaged quantities, are smooth; thus, these equations can be solved on a relatively coarse grid. Third, the moment equations are available in analytic form, even though they are solved numerically in applications. This feature holds the potential for increased physical understanding of the mechanisms of uncertainty.

Extending from one scale to a larger one requires "upscaling," which allows the essence of physical processes at one level to be summarized at the coarser level. For upscaling from the local scale to the field scale, there are usually two kinds of approaches.

The first begins with the macroscopic equations and assumes that they are valid at all (larger) length scales but with different coefficients. At a larger scale, the coefficients such as permeability and porosity are obtained based on finer-scale information.

The second is the stochastic approach, which derives equations governing the statistical moments of the variables of interest from the macroscopic equations. This approach provides not only the prediction but also the associated uncertainty.

In the first section of this report, we describe a stochastic approach and some key results for flow and transport at field scale. Flow and transport at field scale is of practical interest, for example, for problems associated with water resources, groundwater remediation, and oil recovery. The process of upscaling from the macroscopic to the field scale, however, relies heavily on accurate description of flow at the macroscopic scale.

The second section of this article describes our ongoing research project to develop upscaling methods to predict constitutive relationships and other macroscopic coefficients based on some statistical parameters of pore-scale structures.

Although natural porous media are heterogeneous at all length scales, our observations and theoretical treatments are usually limited to a few distinct scales. For example, we commonly associate flow in porous media with three different scales: pore (microscopic), local (lab, macroscopic), and field. Fluid flow may have to be described by different equations at different scales.

At the pore scale, the minute pore structure and detailed occupation of space by different fluids are important; the equations of fluid motion are the Navier-Stokes equations, whereas diffusion and heat conduction are governed by the molecular Fick and Fourier laws. Because of the difficulty in describing the complicated geom-

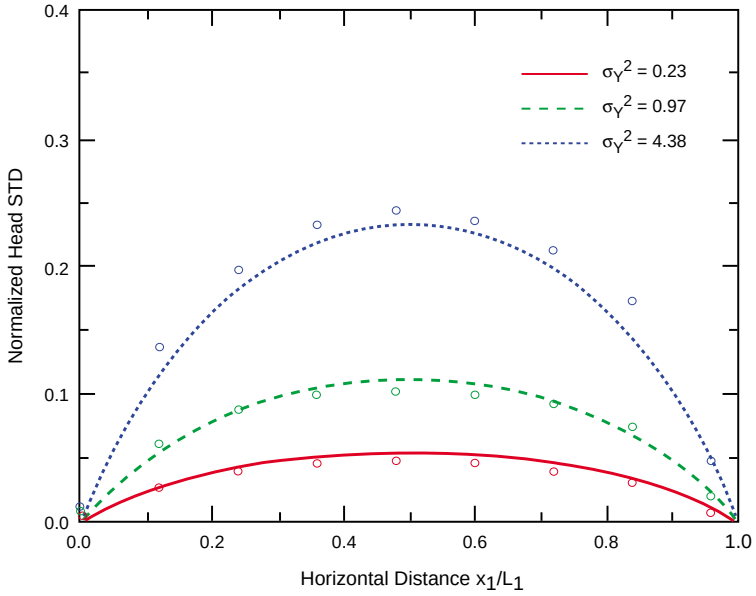

Figure 1. Model Validation.
The graph compares head standard deviations from the moment equation approach (curves) to the published Monte Carlo simulation results (circles).

etry of the individual pores and the fluid interphase boundaries coupled with the complex nature of the physical processes at this scale, the traditional focus has been on the larger lab scale.

At the lab scale, the macroscopic variables are defined by averaging the microscopic variables over a volume containing many pores. Because this volume is large compared to individual pores but extremely small compared to the lab scale, the macroscopic variables become point values, and the pore-scale details may be ignored. In turn, at this intermediate scale, the fluid motion satisfies macroscopic equations (for example, Darcy's law). The coefficients in the macroscopic equations are somehow related to the microscopic structures, and the fluid interphase boundaries may be determined through laboratory experiments. The lab scale is on the order of 10^{-1} to 10^{0} m, whereas the scale of interest can be as large as 10^{4} to 10^{5} m in hydrology and petroleum engineering; we usually refer to the large scale as "field scale."

Uncertainty Analyses of Flow at Field Scale

Despite the fact that geologic media exhibit a high degree of spatial variability, medium properties, including fundamental parameters such as permeability and porosity, are usually observed only at a few locations because of the high cost associated with subsurface measurements. This combination of significant spatial heterogeneity with a relatively small number of observations leads to uncertainty about the values of medium properties and, thus, to uncertainty in predicting flow and solute transport in such media.

The theory of stochastic processes provides a natural method for evaluating the prediction uncertainty. In stochastic formalism, uncertainty is represented by probability or by related quantities like statistical moments. Medium properties, boundary conditions, and initial conditions are treated as random fields whose values are determined by probability distributions. In turn, dependent variables such as pressure and flux are random fields, and the equations governing porous flow become stochastic differential equations whose solutions are probability distributions of pressure and flux. In general, we cannot solve a stochastic differential equation exactly but can only estimate the first few moments of the corresponding probability distribution, especially its mean, variance, and covariances. However, these moments usually suffice to approximate confidence intervals for the flow quantities.

We have developed moment equations for steady-state and transient single-phase flow in bounded domains of nonstationary media. The results from these models are the first two moments of flow quantities. The first moment (mean) can be used to estimate the field of the flow quantity of interest, and the second moment (standard deviation) measures the associated uncertainty (error). These two moments can be used to construct confidence intervals for the flow quantities. These models have been partially validated with Monte Carlo simulations (Figure 1). These flow models may be applied to both groundwater and gas reservoirs.

We have also developed and solved the moment equations for steady-state and transient unsaturated flow and solute transport in the vadose zone. In unsaturated media, water and air coexist in the pore systems. Unsaturated flow is treated as a special case of two-phase flow. We found that the boundary

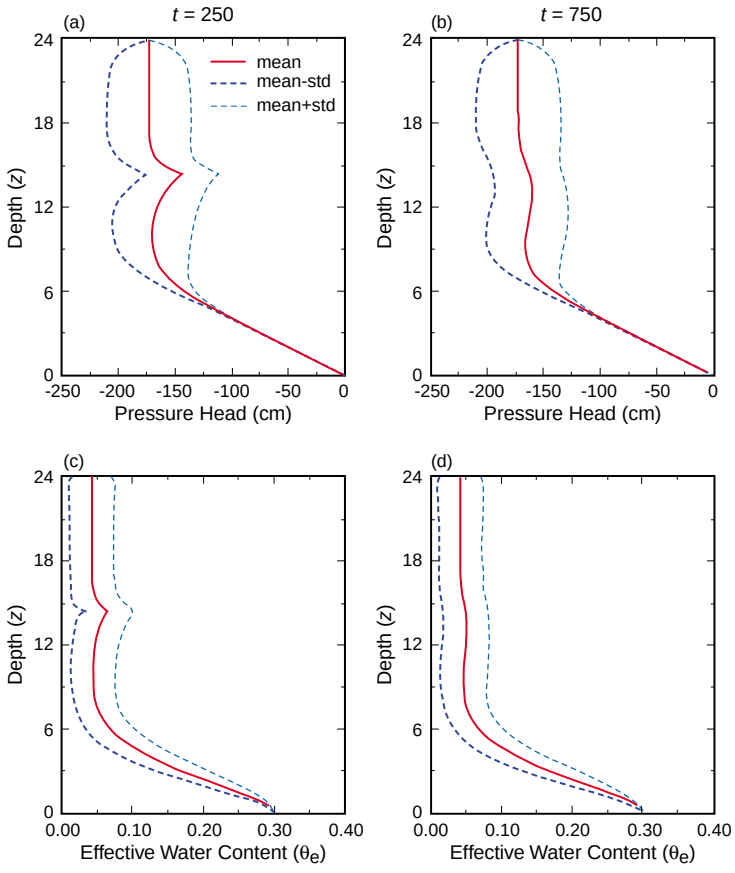

Figure 2. Unsaturated Flow.
The expected values and confidence intervals for pressure head and effective water content at two different times in the presence of an internal source for unsaturated flow in random porous media. The water table is at $z = 0$.

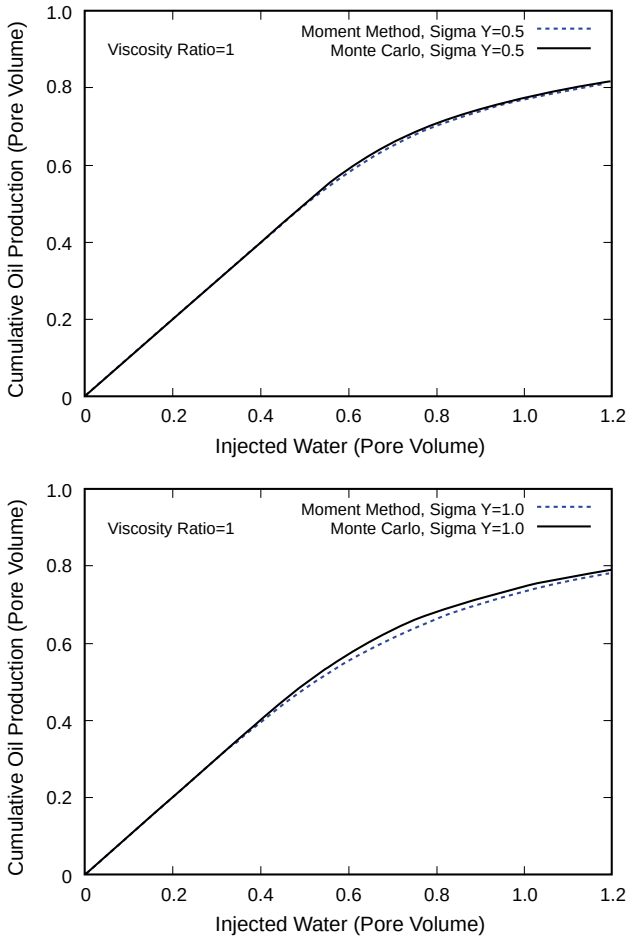

Figure 3. Two-Phase Flow.
The graphs show the cumulative oil production obtained from the moment equation approach and from Monte Carlo simulations for the two-phase case of water displacing oil.

conditions, especially the water table boundary, have a significant impact on the stochastic behaviors of unsaturated flow in random porous media (Figure 2).

For a true two-phase case of water displacing oil, we developed moment equations under both simplified and more realistic boundary conditions. We have compared the stochastic model of two-phase flow with Monte Carlo simulations and have found a very good agreement (Figure 3).

Upscaling from Pore to Macroscopic Scale

The objective of this project is to investigate fundamental issues of multiphase flow systematically at the microscopic and macroscopic scales and to develop upscaling methods for predicting macroscopic quantities and characteristic relationships based on some statistical parameters of microscopic quantities. We do so by applying recently developed computational tools and theoretical frameworks and by comparing these with experimental results. A successful upscaling approach would lead to a greatly increased efficiency and accuracy in simulating multiphase flows in porous media at the lab and field scales.

This past year we used an enhanced lattice Boltzman permeameter to study single-phase flow through pore-scale geometries obtained through high-resolution computed microtomography of rock cores. The permeameter allowed us to investigate some fundamental issues, such as the existence of representative elementary volume (REV), the scale dependence of porosity, specific surface area and permeability, and the relationship of these quantities. We found that although REV may not be well defined in a deterministic sense, it does exist statistically (Figure 4). The figure shows that at each scale, each quantity is computed by averaging over a window of this scale centered at a certain location. These values, obtained at different locations within the domain, are then analyzed to obtain the statistics. The expected values become constant, and the standard deviations approach zero with scale. The behaviors of these quantities indicate the existence of statistical REV. A similar observation is found for a computed microtomography of a sample of Berea sandstone.

The concept of statistical REV is weaker than the deterministic REV but is more useful in applications. We also found that the size of REV may be different for different quantities.

Conclusion

Based on our computational results, we found that rock permeability may not be predicted accurately with existing relationships such as the Kozeny-Carman relation, which is based only on porosity and specific surface area, the lower moments of rock geometry. A more accurate upscaling method would have to involve higher moments of pore geometry, and we will focus the remainder of the project on those. ■

Further Reading

Harter, T., and D. X. Zhang. 1999. Water flow and solute spreading in heterogeneous soils with spatially variable water content. *Water Resources Research* **35**: 415–426.

Sun, A. Y., and D. X. Zhang. 2000. Prediction of solute spreading during vertical infiltration in unsaturated,

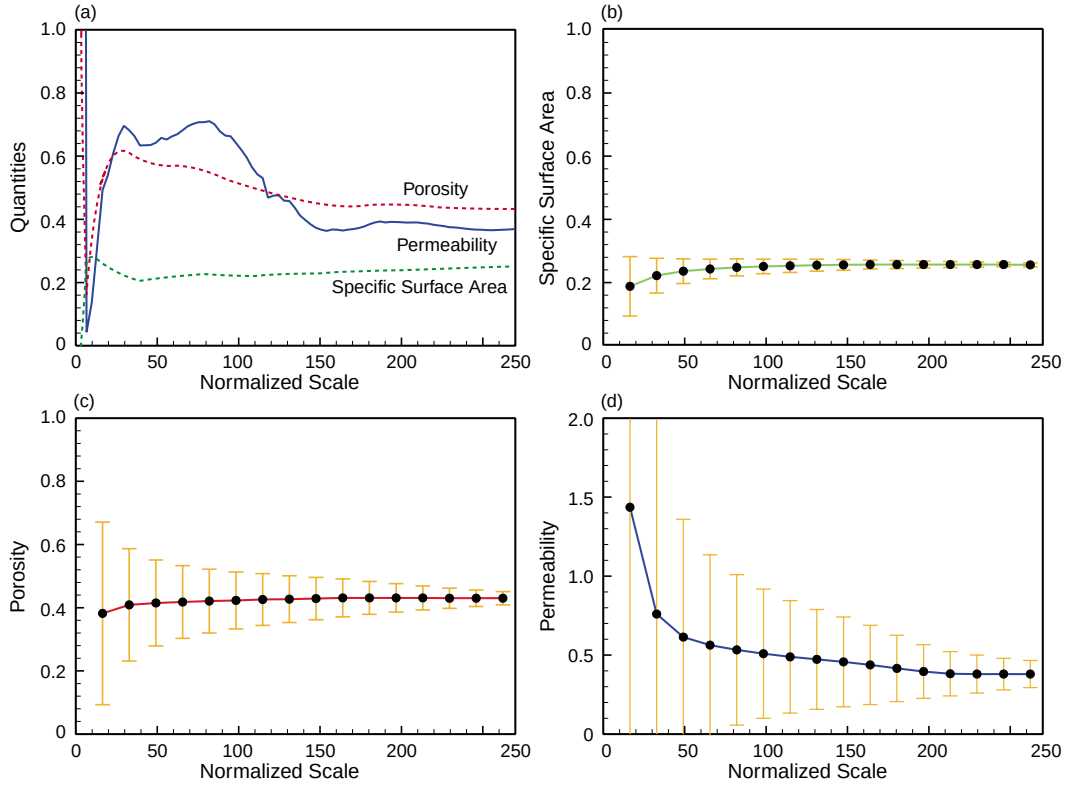

Figure 4. Study of Representative Elementary Volume.
Specific surface area, porosity, and permeability are shown in (a) for the point at the domain center, and their expected values as a function of lattice scale are given in (b), (c), and (d). The expected values are obtained with simulations performed on a computed-microtomography geometry of crushed glass beads divided into a 180 x 256 x 256 lattice structure with a resolution of 17.5 µm. The confidence intervals in these plots are plus or minus one standard deviation.

bounded heterogeneous porous media. *Water Resources Research* **36**: 715–723.

Xin, J., and D. X. Zhang. 1998. Stochastic analysis of biodegradation fronts in one-dimensional heterogeneous porous media. *Advances in Water Resources* **22**: 103–116.

Zhang, D. X. 1997. Conditional stochastic analysis of multiphase transport in randomly heterogeneous, variably saturated media. *Transport in Porous Media* **27**: 265–287.

Zhang, D. X. 1998. Numerical solutions to statistical moment equations of groundwater flow in nonstationary, bounded heterogeneous media. *Water Resources Research* **34**: 529–533.

Zhang, D. X. 1999a. Nonstationary stochastic analysis of transient unsaturated flow in randomly heterogeneous media. *Water Resources Research* **35**: 1127–1141.

Zhang, D. X. 1999b. Quantification of uncertainty for fluid flow in heterogeneous petroleum reservoirs. *Physica D* **133**: 488–497.

Zhang, D. X., and A.Y. Sun. 2000. Stochastic analysis of transient saturated flow through heterogeneous fractured porous media: A double-permeability approach. *Water Resources Research* **36**: 865–874.

Zhang, D. X., and H. A. Tchelepi. 1999. Stochastic analysis of immiscible two-phase flow in heterogeneous reservoirs. *Society of Petroleum Engineers Journal* **4**: 380.

Zhang, D. X., and C. L. Winter. 1998. Nonstationary stochastic analysis of steady-state flow through variably saturated, heterogeneous media. *Water Resources Research* **34**: 1091–1100.

Zhang, D. X., and C.L. Winter. 1999. Moment equation approach to single-phase fluid flow in heterogeneous reservoirs. *Society of Petroleum Engineers Journal* **4**: 118.

Zhang, D. X., L. Y. Li, and H. A. Tchelepi. 2000a. Stochastic formulation for uncertainty assessment of two-phase flow in heterogeneous reservoirs. *Society of Petroleum Engineers Journal* **5**: 60–70.

Zhang, D. X., T. C. Wallstrom, and C. L. Winter. 1998. Stochastic analysis of steady-state unsaturated flow in heterogeneous media: Comparison of the Brooks-Corey and Gardner-Russo models. *Water Resources Research* **34**: 1437–1449.

Zhang, D. X., R. Y. Zhang, S. Y. Chen, and V. E. Soll. 2000b. Pore-scale study of flow in porous media: Scale dependency, REV, and statistical REV. *Geophysical Research Letters* **27**: 1195–1198.

Zhang, D. X., R. Andricevic, A. Y. Sun, X. L. Hu, and G. W. He. 2000c. Solute flux approach to transport through spatially nonstationary flow in porous media. *Water Resources Research* **36**: 2107–2120.

A Nonlinear Elastic Class of Materials

P. A. Johnson (paj@lanl.gov), J. N. TenCate, T. Shankland, and D. E. Smith (EES-11),
T. Claytor and D. Summa (ESA-MT), T. Darling (MST-10), A. Migliori (MST-NHMFL)

It is becoming clear that numerous materials (sand, soil, some ceramics, concrete, etc.) share the elastic properties of rock. These materials have one or more of the following properties: strong nonlinearity, hysteresis in stress-strain relation, and discrete memory. Primarily, it is compliance, the microscopic linkages between the rigid components in the materials, that gives these materials their unusual elastic properties, termed "nonlinear mesoscopic elasticity." Our studies on these still-unexplained properties of certain materials have important implications for basic and applied research, including nondestructive testing of materials (including weapons components), studying earthquake strong-ground motion, and evaluating manufacturing processes such as assembly lines or concrete manufacturing.

Materials with nonlinear microscopic elasticity stand in contrast to liquids and crystalline solids, whose elasticity is due to contributions of atomic-level forces (i.e., materials with atomic elasticity). Atomic-elastic materials are well described by the traditional (Landau) theory of elasticity, and mesoscopic materials are well described by the P-M (Preisach-Mayergoyz) space model of nonlinear elasticity developed by Guyer and McCall. However, the nonlinear mechanisms in mesoscopic elastic materials still remain a mystery.

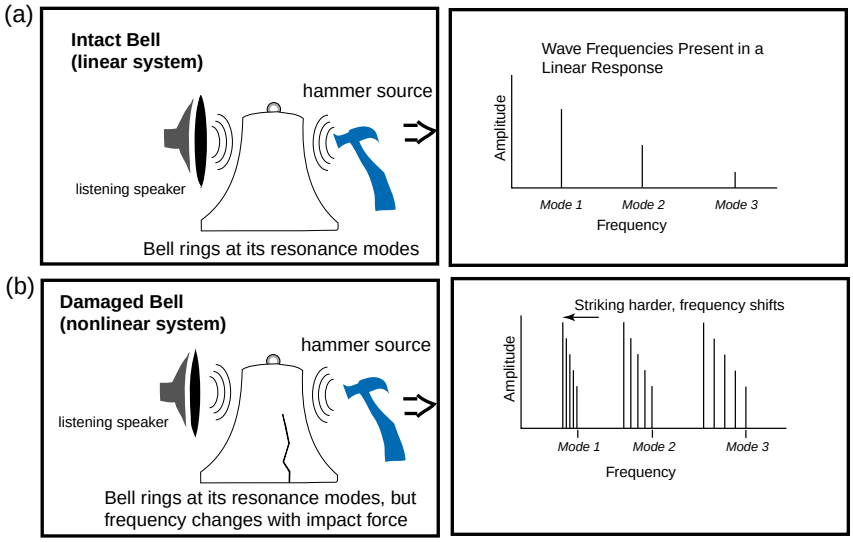

Figure 1. Wave Resonance Behavior in a Bell.
(a) Striking a bell of normal material excites the resonance modes whose frequencies are shown to the right. (b) Striking a bell that has a very small crack (or one composed of mesoscopic nonlinear material) excites modal frequencies whose values depend on how hard we strike (bottom right). This result is a nonlinear effect—a change in wave frequency with wave amplitude.

Introduction

Strike a normal bell, and the bell rings at its resonance modes. Strike it harder, and the bell rings at the same tones, only louder (Figure 1a). Now imagine a bell composed of granite, compressed powdered metal, or other mesoscopic nonlinear material. We strike the bell gently, and it rings normally. Striking it harder, we find, to our surprise, that the tone drops in frequency ever so slightly. Striking it even harder, the tone drops further. The frequency shift is a manifestation of nonlinearity resulting from certain properties of these and other materials. Interestingly, a crack in the bell, even a small crack, will make the bell respond nonlinearly as well—that is, like a rock, etc. (Figure 1b). That remarkable property can be applied to detect damage in materials using a nondestructive technique we call nonlinear resonant ultrasound spectroscopy (NRUS). The NRUS method is being patented.

There are additional manifestations of nonlinearity. If a normal bell is excited with an audio speaker using arbitrarily chosen input frequencies of 440 and 8000 cycles per second (Hz), the bell rings at the two input frequencies (Figure 2a). If we do the same thing with a cracked bell (or one made of granite, powdered aluminum, etc.), interesting things happen again (Figure 2b). Not only does the bell ring at 440 and 8000 Hz, but other frequencies abound. We can detect two, three, and four times each input frequency (880, 1,320, and 1,740 Hz, and 16,000, 24,000, and 32,000 Hz, respectively) and also the sum and difference frequencies (8,000 ± 440 Hz), which are called sidebands. We call this

technique nonlinear wave modulation spectroscopy (NWMS), which is also being patented.

Both the amount of the resonance-peak change with amplitude (Figure 1b) and the appearance of large numbers of new frequencies inside the material (Figure 2b) are not expected results! They are the result of nonlinear interaction of the sound in the damaged bell.

What causes these behaviors? The common theme is the presence of soft regions contained within harder regions. For instance, in a rock, the soft regions are the grain contacts and microcracks; in a crystal, they are dislocations; in powdered compressed metals, they are hard sintered components glued together with softer material much like a rock. A crack in a piece of metal acts as a localized soft region in an otherwise stiff material. Figure 3 illustrates some of these features in materials.

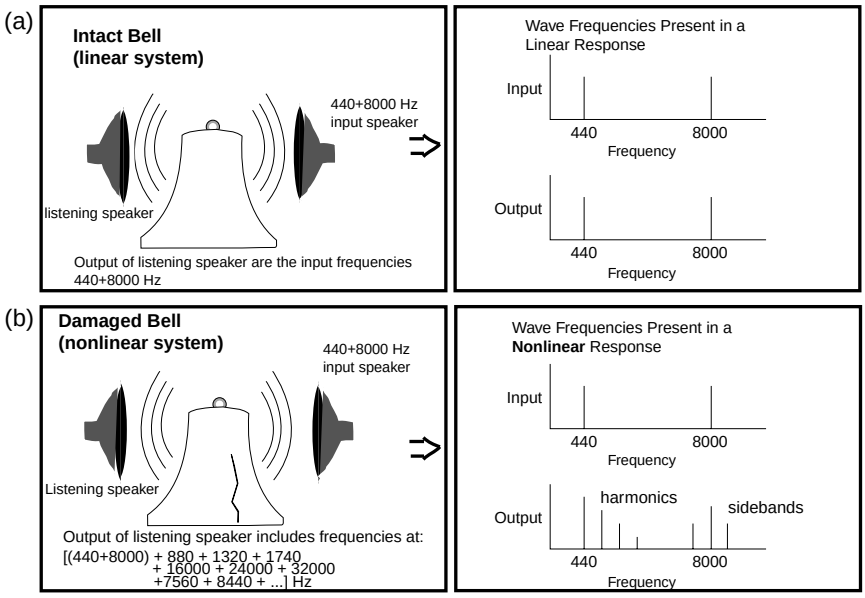

Figure 2. Wave Harmonics and Modulation in a Bell.
(a) A normal bell responds to two frequencies from a speaker with those same two frequencies. (b) For a cracked bell, nonlinear mixing (multiplication) occurs. The two frequencies multiply with themselves to create harmonics and with each other to create sum and difference frequencies (sidebands). We call this nonlinear wave modulation spectroscopy (NWMS). It is being patented.

The Fundamental Measure of Nonlinearity: Stress-Strain

Suffice it to say that the presence of the soft features inside otherwise hard materials gives rise to all forms of elastic nonlinear behavior. Elasticity? That is simply Hooke's law, which relates the applied stress to the resulting deformation, or strain, via a quantity called the modulus. Compressional modulus and shear modulus are among the "spring constants" of linear elasticity theory. Stress is a tensor quantity with units of force per area that, in some instances, coincides with pressure. Stress is usually measured in pascals (0.1 MPa = 1 atm).

A cylinder of Pyrex glass and a block of copper are well described by linear elasticity. They are what we call atomic elastic materials. Not so the materials above. Their elasticity is strikingly nonlinear, is hysteretic, and has discrete memory. For instance, if we study the static behavior of any of the above materials, we will see nonlinearity in the relationship of applied static stress versus the responding deformation. Figure 4 compares the stress-strain relationships of a linear material, Pyrex glass, and a nonlinear material, Berea sandstone.

All or some of these properties (nonlinear/hysteretic/discrete memory) are seen in the elasticity of ceramics, cement, and concrete materials that we think of as consolidated materials (i.e., materials whose primary properties are due to the process of their construction or consolidation). Put another way, the elastic properties of a sandstone and similar materials are not at all those of the grains but rather are conferred by the bonds between the grains (typical scale 1 μm), with the grains acting as essentially rigid elements. It is the bond system, the set of effective elastic elements between the grains and the cracks within the grains themselves, that control the behavior of the elastic properties. These bonds are mesoscopic in size, which is why we call such materials nonlinear mesoscopic elastic materials.

Nonlinearity and Acoustic Waves in Damaged Materials

Returning to the subject of cracked material, we have shown that the nonlinearity resulting from the presence of cracks is an extremely sensitive indicator of damage. The undamaged portion of the sample produces nearly zero nonlinear effects. The damaged portion acts as a nonlinear mixer (multiplier). It is a localized effect. We can easily tell the difference between an undamaged and a damaged object using a frequency spectrum analysis. In fact, we are not aware of a more sensitive, more rapid, and easier-to-apply method for detecting and examining material damage.

Our studies have shown that the nonlinear response of a sample provides a quick, qualitative test of pass/fail (go/no-go) in numerous metal components such as alternator housings, engine bearing caps, gears, Plexiglas, synthetic slates, weapons components, etc., where damage is localized. The elastic nonlinear response is also useful in examining

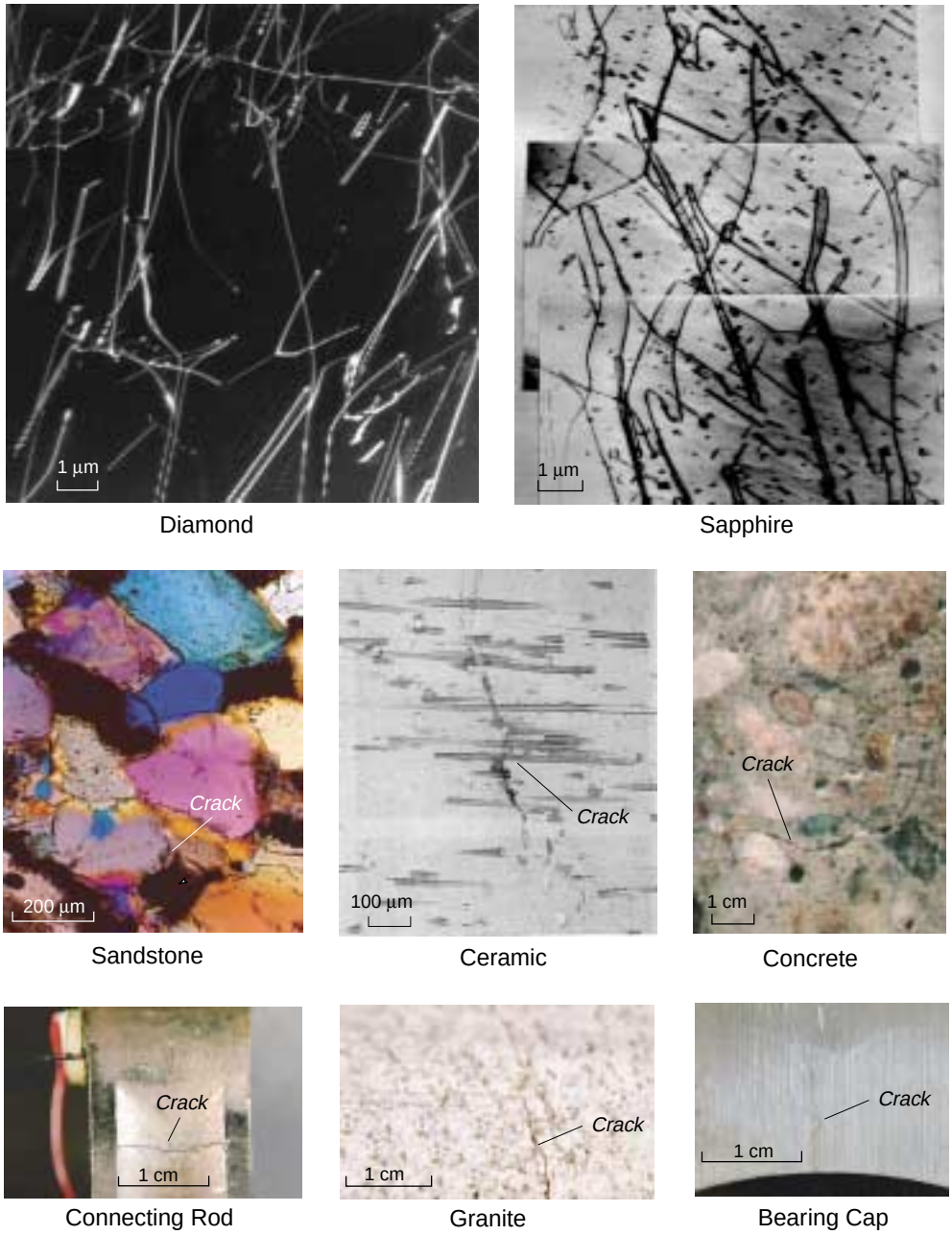

Figure 3. Features that Provide a Nonlinear Response.
Dislocations in type-2 diamond and sapphire, the soft bond system in sandstone, a single crack in ceramic (barium magnesium silicate doped with borosilicate glass), and cracks in concrete, a connecting rod, granite, or a damaged bearing cap are all physical features that can result in a nonlinear response.

the physical state of volumetrically damaged materials such as concrete, rock core, and other porous materials (including the effects of fluid saturation) and is being applied to characterize dislocations in metals and to study progressive damage in these materials (Figure 5).

Summarizing, we can say that as a material fatigues or is damaged, dislocations, cracks, and flaws may be introduced, resulting in a significant change in the material's nonlinear elastic wave behavior. This behavior is manifest in two primary manners when sound is applied to the object. First, under resonance conditions (such as the bell), the resonance tone changes as the applied volume is increased. Second, under resonance, continuous-wave, or pulse-wave excitation, frequency-mixing spectral components, such as wave harmonics, appear. These effects are enormous in damaged material but nearly unmeasureable in undamaged materials. They are the signatures of damage. Linear methods in acoustical nondestructive testing rely on either reflected wave energy from a crack, wave speed changes, or amplitude changes. None of these linear wave characteristics are as sensitive as the nonlinear response of the material.

In volumetrically damaged materials, microfeatures such as dislocations are responsible for the nonlinear behavior. It is very interesting that volumetric and local damage over several orders of magnitude in scale (~10^{-9} to 10^{-1}) provide very similar nonlinear characteristics (e.g., Guyer and Johnson, 1999)! That is, there are close similarities between the nonlinear response from the presence of dislocations in a sample and a single macrocrack in a sample. The similarities are currently under intense scrutiny to determine why this is so. Dislocations, soft grain contacts in rock and concrete, microcracks, and macrocracks can all lead to a large and complex nonlinear wave response (Figure 3).

Example of a Nondestructive Testing Application

As a practical example, we show NWMS experiments in automobile engine bearing caps that determine whether or not damage is present. In these tests, one high-frequency wave and several low-frequency waves were used simultaneously as input. Thus, when damage is present, we would expect mixing of all waves with each other, leading to the creation of many harmonics and sidebands. Figures 6a and 6b show the frequency wave spectrum around the sideband frequencies of the undamaged and damaged samples, respectively. The damaged sample (seen in Figure 5) contains a crack approximately several millimeters deep and 1 cm long and clearly failed the go/no-go test. Note that we observed no change in linear wave speed or wave dissipation between the two samples despite the fact that the nonlinear response is very different.

NWMS is ideal for monitoring progressive damage in materials as well, as the experiment with the plastic rod shown in Figure 7. The rod, fixed at one end, was shaken at its fixed end in shear until failure

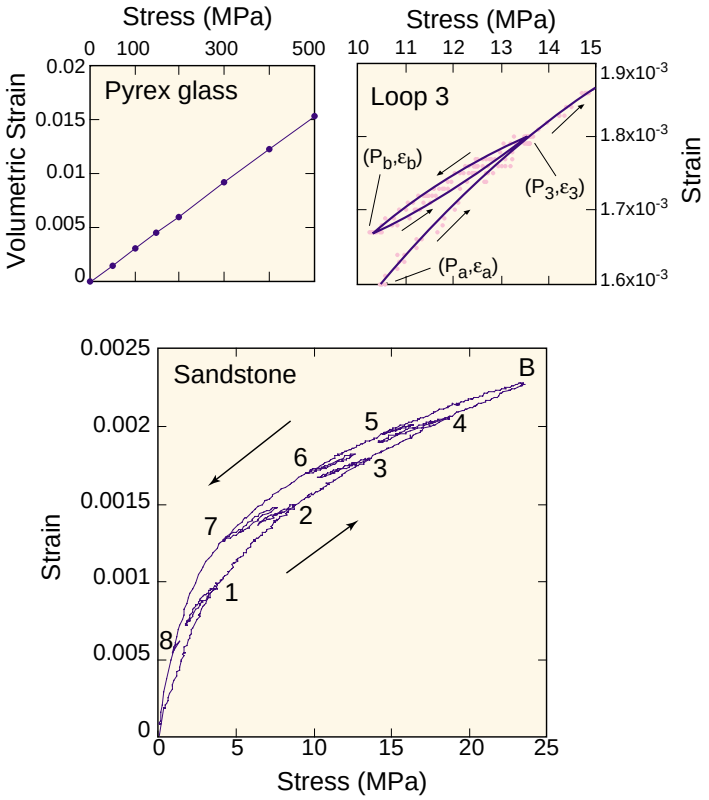

Figure 4. Stress-Strain Relationships.
Here, material is stressed by being squeezed with a piston, and the resulting deformation, or strain, is measured. Pyrex glass (top left), a normal or atomic elastic material, has a stress-strain relationship that is linear from 0 to 500 MPa. On the other hand, Berea sandstone (bottom), a mesoscopic elastic material, is highly nonlinear as evident in the curved response from 0 to 25 MPa. The sandstone also shows hysteresis—when stress is reversed at B, strain only partially reverses, and a loop forms. The small numbered loops are the result of other small excursions in the stress; details of the third reversal are shown at top right.

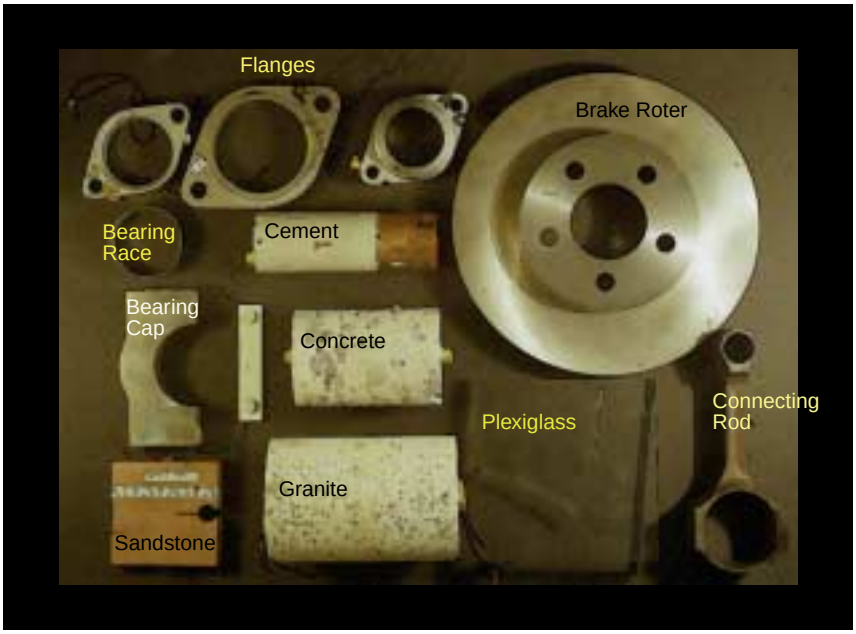

Figure 5. Objects Tested for Damage.
All of the samples shown here are damaged in some manner, either with a small localized crack or with volumetric damage.

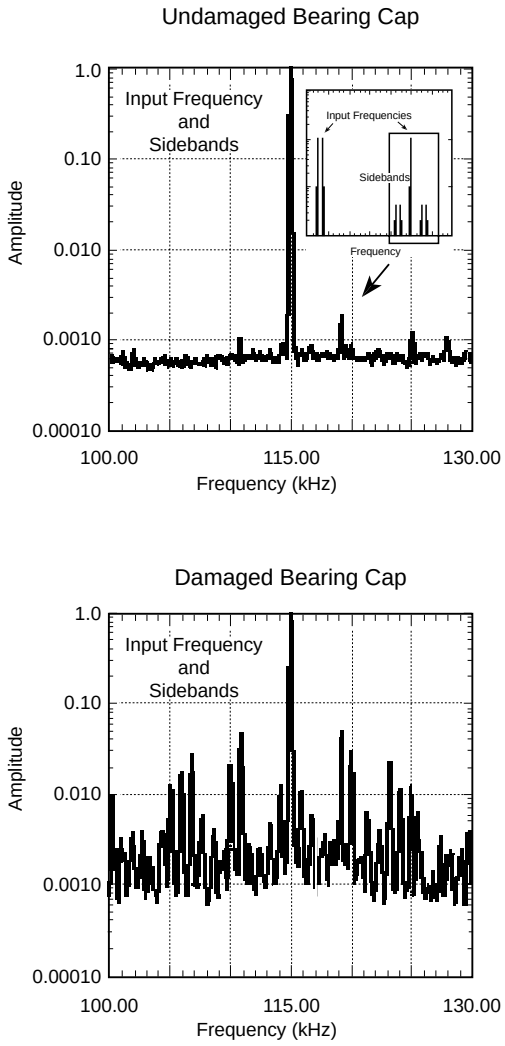

Figure 6. A Nonlinear Wave Modulation Spectroscopy Experiment.
The graphs are NWMS frequency spectra from wave modulation tests of (a) undamaged and (b) damaged engine bearing caps. The inset (top) shows a full spectrum including the sideband portion. There are many sidebands because multiple frequencies were input simultaneously in continuous-wave mode.

occurred. Linear and nonlinear behavior was monitored at each step. The linear responses were relatively insensitive to induced damage until just before failure, whereas the nonlinear response was affected early in the damage process and became enormous quickly. Nonlinear means are far superior to linear means in progressive damage detection.

Strong Ground Motion During Earthquakes

If the 1906 San Francisco earthquake took place today, the costs to replace the infrastructure would surely exceed a trillion dollars. One key to mitigating such a disaster is understanding and modeling the physical system on which structures are built (in the worst case, a structure built on soft sedimentary layers that can significantly amplify seismic waves). This process is well understood by both the seismic and civil engineering communities; unfortunately, a key aspect that is not well understood is the enormous effect of the nonlinear response of the system on structural damage and failure. In 1997, in an article in *Nature* (Field et al., 1997), we first demonstrated unequivocally that nonlinearity is a significant influence in strong ground motion.

During a large earthquake, buildings collapse and are damaged because soft sediments just beneath the Earth's surface can amplify seismic shear waves as a result of (1) seismic wave velocity gradations and (2) trapping of wave energy, creating resonances and dramatically increasing seismic wave amplitudes. This amplification is called strong ground motion. Amplified wave frequencies that correspond to the resonant modes of a structure can couple into the structure, leading to damage and ultimately, failure. The greatest unknown in this physical system is the influence of the nonlinear response, which can dramatically alter sediment resonance frequencies and wave amplitudes in ways that are only now becoming clear.

In an earthquake wave in a surface layer, every frequency component in the wavefield multiplies nonlinearly with itself and with every other frequency component, just as in the examples shown above. For instance, any two angular frequencies ω_1 and ω_2 will multiply with each other, creating additional frequency components at $\omega_1 \pm \omega_2$, $2\omega_1$, $2\omega_1 \pm \omega_2$, $3\omega_1$, $3\omega_2$, and so forth. The interaction is amplitude-dependent; for example, in the case of a resonating layer, resonance peak frequencies and mixing of these frequencies dominate the amplitude of the spectral response. As the amplitude increases, energy is progressively redistributed from the resonance frequency to other portions of the spectrum. As a result of wave mixing, we expect new frequency components to appear, especially at multiples of resonance frequencies as the driving force (the source magnitude) becomes larger and larger.

The effects of nonlinear wave mixing are important because the models most often used in prediction of strong ground motion do not incorporate frequency mixing, and strain softening is not well understood. We have unique experience and a unique

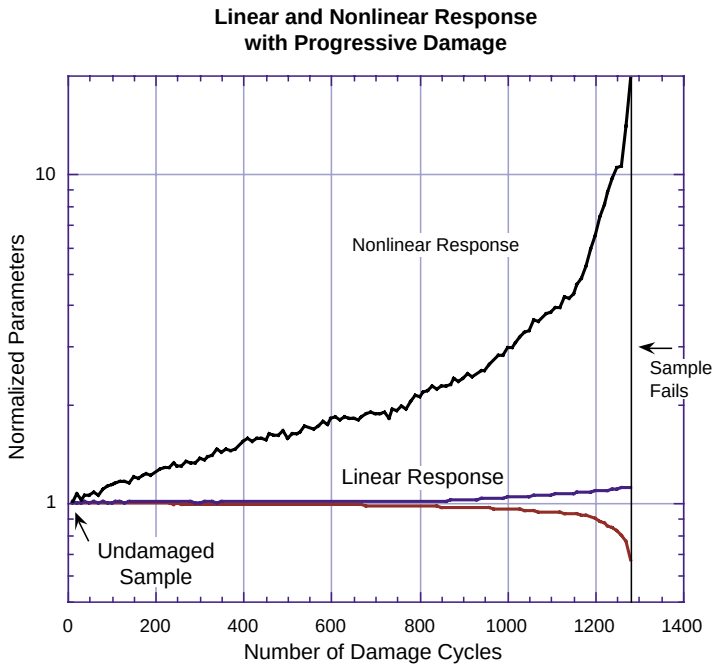

Figure 7. Progressive Damage in Plastic.
This plot (courtesy of Peter Nagy) of linear and nonlinear response as a function of damage cycles for a plastic rod shows that the linear responses (wave dissipation in blue and wave speed in red) are relatively insensitive to induced damage until just before the sample fails at nearly 1,300 cycles. However, the nonlinear response is affected early in the damage process and grows quickly.

group of analytical tools that we developed for strong-motion data analysis. For instance, we developed the method of constant strain analysis and resonance-template-matched filtering that take advantage of both phase and amplitude of the Fourier transformed seismic signal. These novel methods (currently being patented) provide us unparalleled sensitivity for studying resonance frequency changes (or jumps) as a function of earthquake magnitude and guide our modeling efforts of the nonlinear response. Furthermore, our experience in understanding nonlinear behavior in earth and damaged materials is unparalleled and provides us a unique point of view for addressing this problem.

Conclusion

Dynamic nonlinear response of mesoscopic materials is a new and extremely exciting domain of study, both from the standpoint of basic research into materials and from that of applications. We have identified a new universal class of materials that we believe includes geomaterials and many types of manufactured materials, including damaged materials. There are potentially many applications of enormous economic and safety impact that will evolve from nonlinear applications. Applications and spin-off research will affect a number of problems, from designing earthquake-resistant structures to eliminating flawed components fabricated on an assembly line and monitoring long-term aging in infrastructure. Further, application to structures after an earthquake may well provide valuable information regarding the extent of the damage. We anticipate that within 10 years, nonlinear methods may be used routinely in applications as diverse as quality control in manufacturing processes, quality control of concrete curing, monitoring reactor containment walls for damage, inspecting aircraft and spacecraft for damage, and observing fatigue damage in buildings, bridges, tunnels, and gas or oil pipe lines. ■

Acknowledgements

Funding: Technology Partnership Program, Los Alamos Institute of Geophysics and Planetary Physics, Laboratory Directed Reseach Development Program, and U.S. Department of Energy Office of Basic Energy Sciences.

Further Reading

Field, E. H., P. A. Johnson, I. A. Beresnev, and Y. H. Zeng. 1997. Nonlinear ground-motion amplification by sediments during the 1994 Northridge earthquake. *Nature* **390**: 599–602.

Guyer, R. A., and P. A. Johnson. 1999. The astonishing case of mesoscopic elastic nonlinearity. *Physics Today* **52**: 30–35.

Guyer, R. A., J. N. TenCate, and P. A. Johnson. 1999. Hysteresis and the dynamic elasticity of consolidated granular materials. *Physical Review Letters* **82**: 3280–3283.

Johnson, P. 1999. The new wave in acoustic testing. *Materials World: The Journal of Inst. Materials* **7**: 544–546.

TenCate, J. A., E. Smith, and R. A.Guyer. 2000. Universal slow dynamics in granular solids. *Physical Review Letters* **85**: 1020–1023.

Van den Abeele, K. E. A., J. Carmeliet, J. A. TenCate, and P. A. Johnson. 2000. Nonlinear elastic wave spectroscopy (NEWS) techniques to discern material damage: Part II. Single mode nonlinear resonant acoustic spectroscopy. *Research on Nondestructive Evaluation* **12**: 31–42.

Van den Abeele, K. E. A., P. A. Johnson, and A. Sutin. 2000. Nonlinear elastic wave spectroscopy (NEWS) techniques to discern material damage: Part I. Nonlinear wave modulation spectroscopy (NWMS). *Research on Nondestructive Evaluation* **12**: 17–30.

Also see Los Alamos Center for Nonlinear Elastic Materials at http://www.ees4.lanl.gov/nonlinear/.

Measuring Total Soil Carbon with Laser-Induced Breakdown Spectroscopy

M. H. Ebinger (mhe@lanl.gov) and D. D. Breshears, EES-10, D. A. Cremers (C-ADI), and P. J. Unkefer (B-S1)

Terrestrial carbon fluxes account for more than half of the carbon transferred between the atmosphere and the Earth's surface (about 120 gigatons/yr), and current stores of carbon in terrestrial ecosystems are estimated at 2,060 gigatons. Given humanity's ability to modify terrestrial systems and, hence, to control these fluxes, management and sequestration of carbon in the terrestrial biosphere has emerged as the most promising near-term means of mitigating overall U.S. carbon emissions, as highlighted in the 1999 Department of Energy Carbon Sequestration Report. We are in the process of testing a new spectroscopic method for measuring total soil carbon, based on laser-induced breakdown spectroscopy (LIBS).

Much of the carbon in terrestrial ecosystems is in the form of soil carbon, which is the fundamental building block of soil organic matter. Consequently, soil carbon is a primary determinant of many soil chemical and physical properties, including nutrient availability, soil structure, and water-holding capacity, all of which directly influence ecosystem productivity and land quality.

Soil carbon measurement is the focus of current and future international negotiations and treaties related to global climate change. To manage terrestrial carbon inventories and fluxes effectively, it is important to find more efficient ways to measure soil carbon. It is possible that we may need orders of magnitude more measurements than have been obtained to date.

The LIBS method is based on atomic-emission spectroscopy. In this method, a laser is focused on a solid sample and forms a microplasma that emits light characteristic of the elemental composition of the sample. The emitted light is collected, spectrally resolved, and detected to monitor concentrations of elements via their unique spectral signatures. When calibrated, the LIBS method provides quantitative measurements. This method is readily amenable for field-portable instrumentation and high-throughput analysis.

In the discussion below of our preliminary work, we evaluate the LIBS method to measure total soil carbon and test the hypothesis that the LIBS carbon signal is correlated with total soil carbon. Our results suggest that the LIBS method provides a useful new approach for measuring total soil carbon.

Methods

To assess ways to detect carbon using existing LIBS technology, we evaluated different carbon emission lines that are produced by LIBS and selected a strong emission peak occurring at 247.8 nm to use for measuring carbon. A laser (type Nd:YAG) set at a wavelength of 1,064 nm (50-mJ pulses of 10 ns) was focused with a lens of 50-mm focal length on each soil sample (Figure 1). The light was collected by a fused silica fiber-optic cable pointed at the plasma from a distance of about 50 mm. A spectrograph of 0.5-m focal length resolved the light that was then detected using a gated-intensified photodiode array detector.

For each LIBS analysis, a sample was placed in a 25-μm-diameter × 75-μm-long quartz tube, which was then positioned such that the focal volume of the laser pulse was centered in the tube. Twenty laser pulses were directed into the tube to complete one measurement. Typical measurement areas for the LIBS method are 1 to 5 mm^2/pulse. The background signals from carbon and silicon emissions were subtracted from the resulting spectrum, and this procedure was repeated for each sample. Because of shot-to-shot variations in the laser plasma parameters and sampling geometry, measurement precision is increased by taking the ratio of the analyte signal to the signal from another species, in this case silicon, with the same concentration assumed in all samples.

We measured total soil carbon with the conventional dry combustion method using a Dohrmann DC-180 analyzer and then with LIBS to calibrate, verify, and assess performance of our LIBS method. We calibrated and tested the LIBS measurements using soils from a series of farms in east-central Colorado and soils from a piñon-juniper woodland near Los Alamos, New Mexico.

The total soil carbon concentrations from a subset of the Colorado samples were measured using dry combustion, and these soil concentrations were used to verify the calibrated LIBS method against (1) different samples from a subset of the same soils and (2) soils of distinctly different parent material and genesis (alfisols weathered from

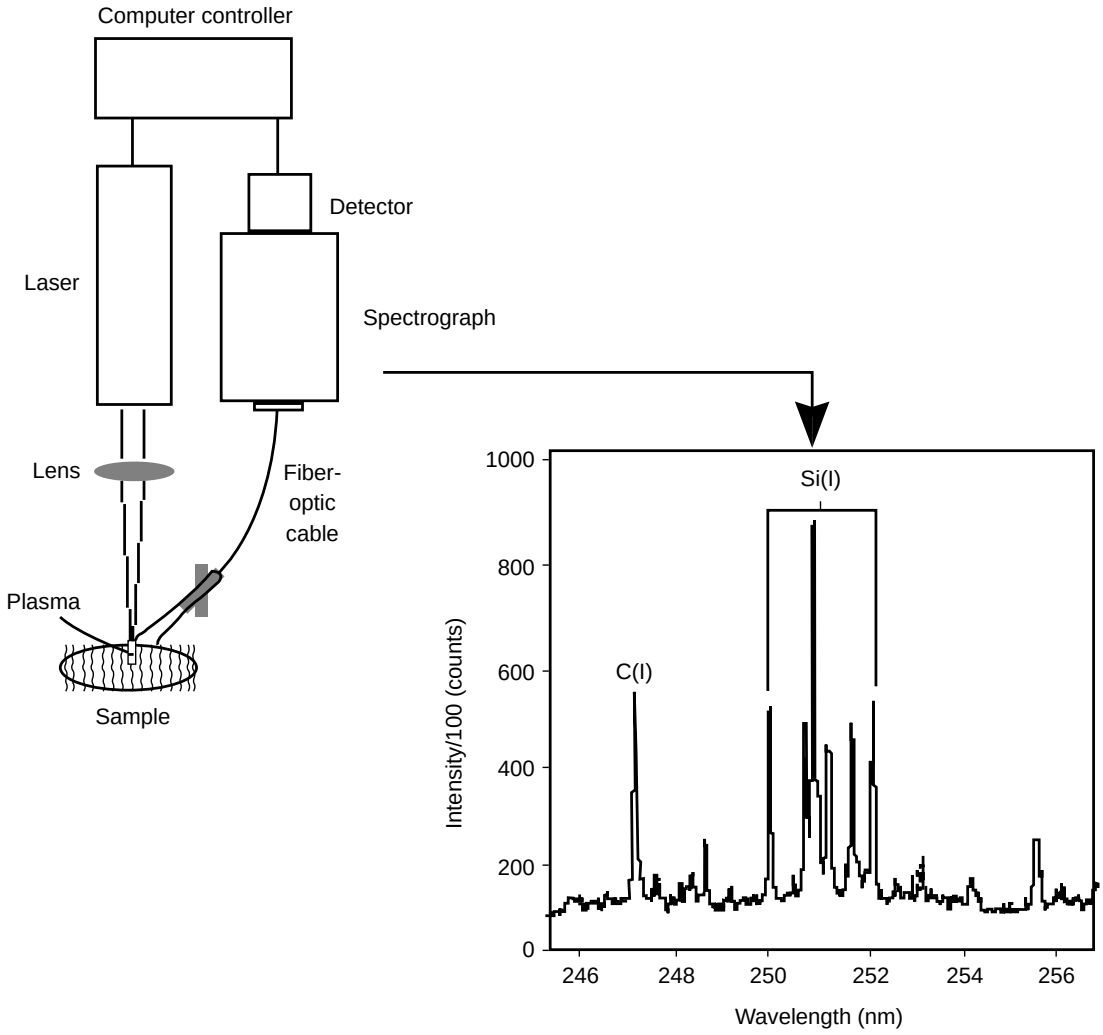

Figure 1. The LIBS Apparatus.
This diagram of the apparatus shows a LIBS spectrum of a soil tuned to monitor the carbon emission at 247.8 nm. To the right of the carbon line is a series of silicon lines used for quantification.

volcanic tuff in the piñon-juniper woodland near Los Alamos).

The Colorado soil samples were collected from cultivated plots in mollisols weathered from sandstone that were conventionally tilled. Samples were collected from random locations in the fields after harvest from 0 to 10 cm and 10 to 20 cm below the soil surface. The piñon-juniper woodland samples were collected under piñon trees (*Pinus edulis*) or juniper trees (*Juniperus monosperma*) or in intercanopy spaces that were either grass-covered or bare. These piñon-juniper samples were collected in 5-cm intervals to 30 cm or until parent material was observed. Each sample was sieved to <2 mm, air dried, then analyzed by dry combustion and LIBS.

We evaluated LIBS measurement performance from the collected data. A detection limit (DL) for carbon was estimated using the formula DL = 3 σ/m, where σ is the standard deviation of 6 to12 replicate measurements and m is the slope of the calibration curve. We estimated the measurement precision by performing 6 to 12 replicate measurements on several samples and computing the percent relative standard deviation. Accuracy was estimated by comparing LIBS measurements to dry combustion measurements obtained from two different laboratories.

Results

We determined that carbon could be identified and quantified using LIBS. A plot of the LIBS signal versus carbon concentration for soils from the cultivated plots (Colorado samples) shows excellent correlation and provides a calibration curve (Figure 2a). The calibration curve was effective in predicting the carbon content of additional samples from the cultivated plots (Figure 2b). The same calibration curve was also effective in predicting carbon concentrations in semiarid alfisols (Los Alamos samples), even though the genesis of the soils was

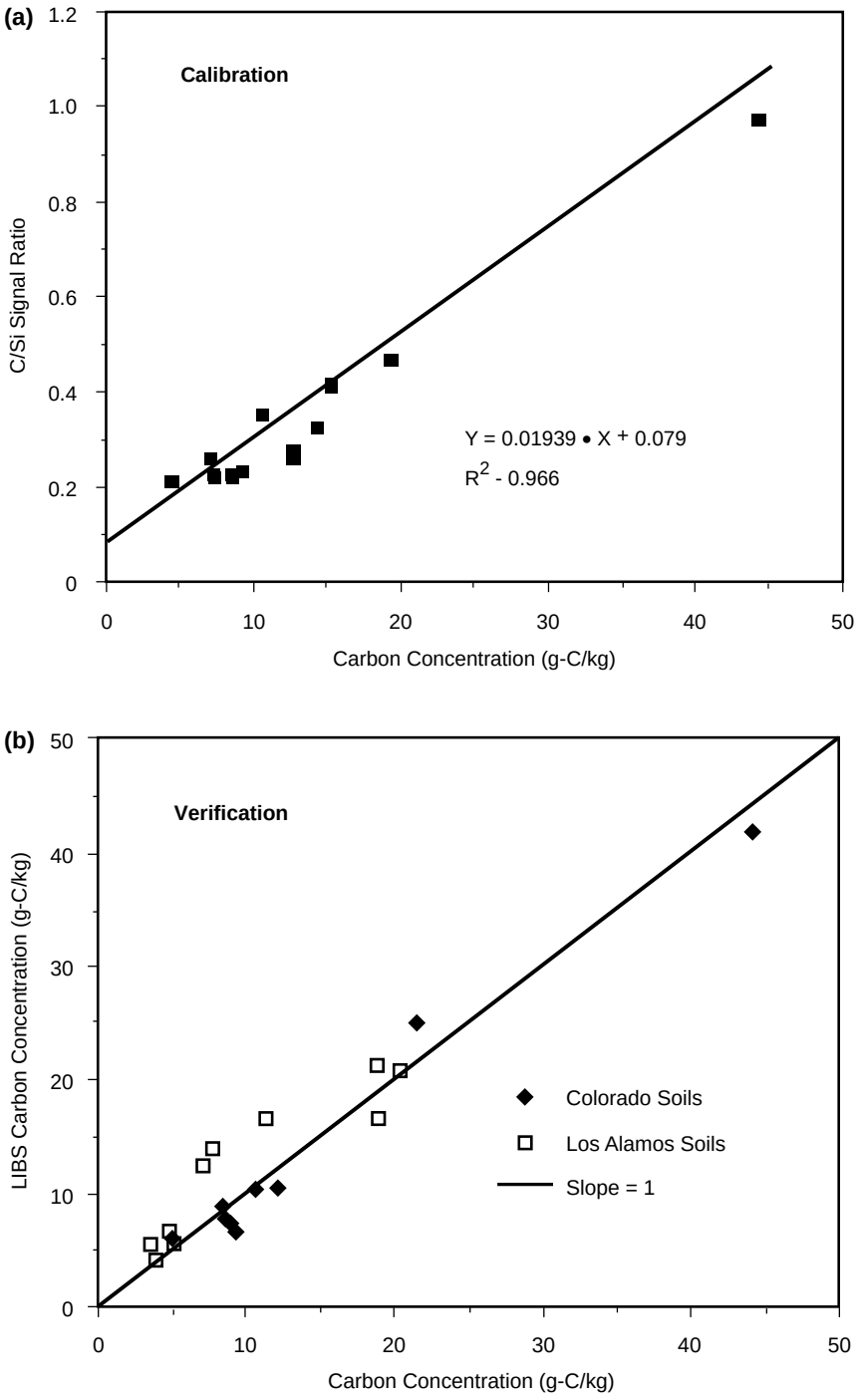

Figure 2. LIBS Soil Data.
(a) Calibration curve for the detection of total soil carbon from Colorado mollisols. The data show a strong relationship between the LIBS signal and total soil carbon.
(b) Correlation between the predicted carbon concentration by LIBS and the percent carbon determined by dry combustion for Colorado mollisols and Los Alamos alfisols. The line indicates exact correlation between LIBS measurements and dry-combustion determinations.

significantly different (Figure 2b). The effectiveness of the calibration curve supports our hypothesis that the magnitude of the carbon signal detected by LIBS is a good indicator of the total soil carbon concentration. We estimated LIBS detection limit to be 300 mg-C/kg^{-1} with precision of 4 to 5% and accuracy of 3 to 14%.

Conclusion

Our initial work on application of the LIBS method to total soil carbon measurement suggests that LIBS can provide rapid and efficient measurements of total soil carbon with appropriate limits of detection, accuracy, and precision. Good carbon measurements with LIBS were obtained with two distinct soil types. Additional work is needed to evaluate if measurements must be adjusted for effects such as soil type and texture, a wide range in carbon concentration, carbonate, bulk density, and soil water content. In addition, we are evaluating the feasibility of incorporating a constant silicon standard in the method to avoid variation in soil silicon due to changes in mineralogy among soil samples. Because LIBS can be made field portable and has short sample analysis time, it could be very useful for obtaining large numbers of carbon measurements in the field. Our preliminary findings suggest that the LIBS method may help to address carbon measurement and management issues in range land, agricultural, and forest ecosystems. ■

Collaborator

Joel R. Brown, U.S. Department of Agriculture National Resource Conservation Service

Further Reading

Cremers, D. A., M. J. Ferrism and M. Davies. 1996. Transportable laser-induced breakdown spectroscopy (LIBS) instrument for field-based soil analysis. *Proceedings of the Society of Photo-Optical Instrumentation Engineers* **2835**: 190–200.

Davenport, D. W., B. P. Wilcox, and D. D. Breshears. 1996. Soil morphology of canopy and intercanopy sites in a piñon-juniper woodland. *Soil Science Society of America Journal* **60**: 1881–1887.

DOE (U.S. Department of Energy). 1999. Carbon sequestration research and development. Report DOE/SC/FE-1 [www document]. URL http://www.ornl.gov/carbon_sequestration.

Radziemski, L. J., and D. A. Cremers. 1989. Spectrochemical analysis using laser plasma excitation. In *Applications of Laser-Induced Plasmas*, L. J. Radziemski and D. A. Cremers, editors, pp. 295–325. New York, NY: Marcel Dekker.

Rusak, D. A., B. C. Castle, B. W. Smith, and J. D. Winefordner. 1997. Fundamentals and applications of laser-induced breakdown spectroscopy. *Critical Reviews in Analytical Chemistry* **27**: 257–290.

Sollins, P., C. Glassman, E. A. Paul, C. Swanston, K. Lajtha, J. W. Heil, and E. T. Elliott. 1999. Soil carbon and nitrogen: Pools and fractions. In *Methods in Ecosystem Science*, O. E. Sala, R. B. Jackson, H. A. Mooney, and R. W. Howarth, editors, pp. 89–105. New York, NY: Springer.

Zero-Emission Coal Technology

H. Ziock (EES-6, ziock@lanl.gov) and K. Lackner (T-DO)

Fossil energy is the backbone of the world energy supply and the motor of modern economies. Yet, in spite of its obvious importance, the entire fossil energy sector is threatened by concerns about carbon dioxide (CO_2) accumulating in the atmosphere. The world seems to face a stark choice: curtail economic growth or face potential environmental catastrophe. We are investigating a new technology that will allow us to continue to use our vast fossil energy sources without releasing CO_2 and other emissions to the atmosphere.

Fossil energy sources are vast. Coal reserves alone are sufficient to last for hundreds of years, even with greatly increased world energy consumption rates. Consequently, we have selected zero-emission coal technology as the focus of our program development and research efforts. Zero-emission coal technology could provide low-cost, clean, copious energy from coal for centuries to come without increasing CO_2 levels in the atmosphere.

Our initiative on zero-emission coal technology has led to establishment of the Zero Emission Coal Alliance (ZECA), an alliance of industry, government, and research institutions. ZECA is pursuing a technology for generating hydrogen and/or electricity from coal in an emission-free manner. The process generates a pure stream of CO_2 that can be disposed of in any number of sequestration approaches.

The Los Alamos Approach

Our long-term goal (which is shared by ZECA) is to have a zero-emissions fossil-fuel-based energy source that converts CO_2 into a solid (mineral) by reacting it with an appropriate starting material, possibly in an industrial process. The concept is illustrated in Figure 1. The advantage of our approach is that it addresses the full fuel cycle with the

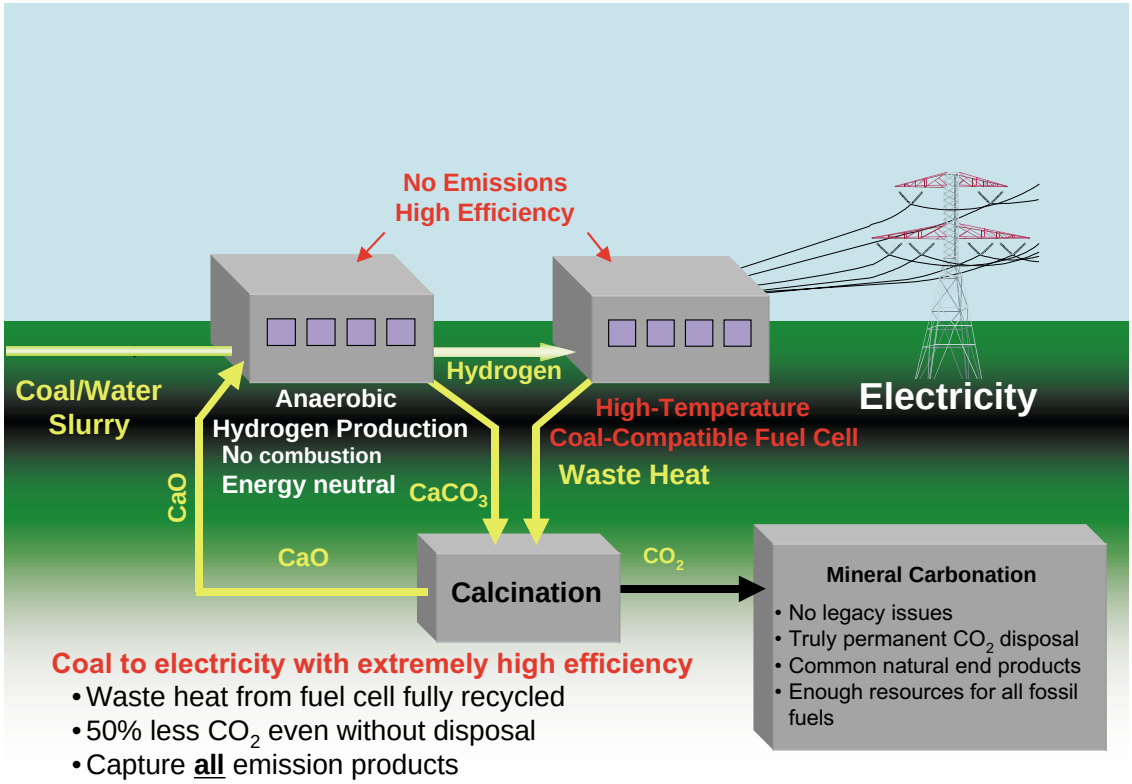

Figure 1. Zero-Emission Coal Process.
The diagram shows conversion of coal to electricity with extremely high efficiency. The waste heat from the fuel cell is fully recycled; there is 50% less CO_2 even without disposal; and *all* emission products are captured.

CO_2 being rendered immobile and benign, which avoids costly monitoring and the potential for environmental disaster. Sufficient raw materials in the form of magnesium silicates exist to handle all of the world's coal easily. The end products (magnesium carbonate and silica) are stable solids, thereby guaranteeing the permanent sequestration of the CO_2.

The full coal gasification and power production process that produces a pure stream of CO_2 involves a number of integrated yet distinct modules, as can be seen in Figure 2. In the first module, coal is reacted with hydrogen to produce methane (CH_4). In the second module, the methane is reacted with lime (CaO) and water to produce calcium carbonate ($CaCO_3$) and hydrogen (half of which is recycled back to the first module). These first two modules comprise the anaerobic production of hydrogen. In the third module, the ($CaCO_3$) is calcined to produce a pure stream of CO_2 and lime (which is recycled to the second module). In the fourth module, the hydrogen is used by a solid oxide fuel cell to produce electricity, water, and heat (used in the third module). The net effect of this process is that coal is used to generate electricity in a highly efficient zero-emission coal plant, which inherently generates a separate waste stream of concentrated CO_2 containing all the carbon brought into the process as coal. This stream of CO_2 is subsequently transferred to a separate mineral carbonation plant to be reacted with magnesium silicates derived from serpentinites or peridotites. The end products are returned to the serpentine mine. Alternative fates for the CO_2 (for example, use in enhanced oil recovery) are also compatible with our zero-emissions gasification concept, but the objective is the safe and permanent storage of CO_2. The process described above is likely to be the only one that will fully meet this objective.

In Figure 2, the material flow is represented in an idealized schematic, emphasizing the dominant compounds produced in each step. Coal enters the gasification vessel as a slurry or dry material and is then gasified with hydrogen. In contrast to the coal-based, combined water-gas production and shift reactions, hydrogenation of carbon to methane is exothermic. By injecting water into the gasifier, one can quench the heat release and maintain a constant temperature in the gasifier vessel. By transforming the carbonaceous compounds of the fuel into gaseous forms, the gasifier separates the ash from the fuel. The carbon, which is now in the form of volatile carbon compounds, enters the carbonation vessel where it reacts with water to form CO_2 and H_2. The CO_2 is continuously removed from the reaction zone by reacting it with CaO to form $CaCO_3$. The mixture of liquid water, steam, volatile hydrocarbons, and CaO that reacts in this vessel neither consumes nor generates heat. The energy neutrality follows from the observation that the net reaction

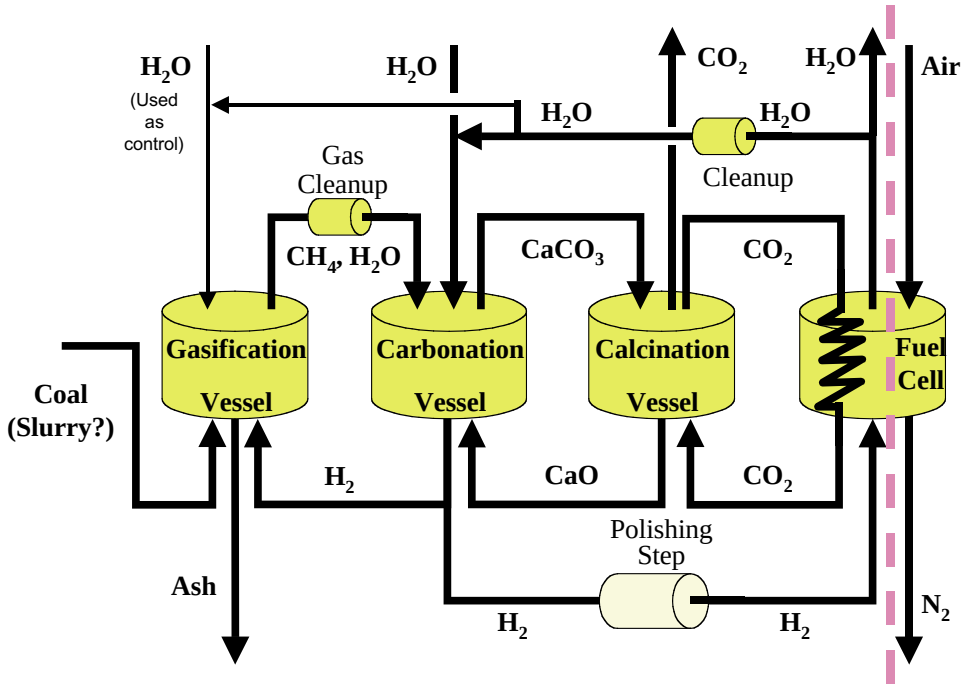

Figure 2. Anaerobic Hydrogen Production and Fuel Cell System.
Material flows in the diagram are idealized to the predominant components. The major reactions are:

Gasification Vessel: $C + 2H_2 \rightarrow CH_4$, H_2O (liquid) $\rightarrow H_2O$ (gas)
Carbonation Vessel: $CH_4 + 2H_2O \rightarrow CO_2 + 4H_2$, $CaO + CO_2 \rightarrow CaCO_3$
Calcination Vessel: $CaCO_3 \rightarrow CaO + CO_2$
Fuel Cell: $2H_2 + O_2 \rightarrow 2H_2O$

in the gasification and carbonation units is essentially energetically neutral:

$$CaO + C + 2H_2O \text{ (liquid)} \rightarrow CaCO_3 + 2H_2 + 0.6 \text{ kJ/mol C}.$$

Thus, the total heat release in the gasification and carbonation vessels is zero. Because the first vessel has been adjusted to have zero heat release, the second one will have zero heat release as well. The reaction in the calcination vessel requires heat, which is provided by the solid-oxide fuel cell (the fourth module). For thermodynamic reasons, at their operating temperature, these fuel cells cannot avoid turning approximately one-third of the chemical energy of hydrogen oxidation into waste heat. However, solid-oxide fuel cells operate at a temperature at which this waste heat can be used to calcine $CaCO_3$. The overall system is highly efficient because it uses the waste heat of the fuel cell to regenerate lime. In the theoretical limit of pure carbon, zero heat losses, and optimal performance of the fuel cell, the efficiency of converting the carbon fuel into electricity would be 93%. Additional losses occur because heat will escape from the vessels and because a realistic conversion efficiency for a fuel cell is less than the thermodynamically allowed limit. Nevertheless, a very high conversion efficiency, on the order of 70 to 80% (compared with 30 to 35% for today's power plants), for the conversion of coal energy to electrical energy should be achievable. It is important to note that for the ZECA process, the 70 to 80% efficiency values already include the efficiency reductions associated with separating out the CO_2 in a pure stream and compressing it to high pressure. The above efficiency values for the conventional plants do not yet include these reductions. Estimates of the efficiency penalty of incorporating the required retrofits into existing power plants would reduce their net efficiencies to approximately 25%.

The process is also attractive because it eliminates all emissions to the air. This process has no smokestack, as there is no combustion of the coal. Thus, the ash (particulates) in the coal is fully contained, making compliance with proposed particulate emission restrictions straightforward. A small amount of additional calcium oxide or $CaCO_3$ is used to capture the sulfur in the coal. The sulfur is pulled out of the reaction vessels in a solid form, thereby eliminating hydrogen sulfide or SO_X emissions. The reducing conditions inside the hydrogen production vessel and the absence of any combustion limit the formation of NO_X from any nitrogen in the coal. Finally, the CO_2 generated in the hydrogen production is initially extracted as a solid, before being converted to a pure gas stream. Because this extraction is an integral part of the hydrogen production process, no additional expenses are incurred in producing a concentrated CO_2 exhaust stream.

To dispose of the CO_2 permanently, we are investigating a process to convert it to a stable solid, thereby leaving no CO_2 legacy issue for future generations. In our carbonation process, we will react CO_2 with abundant, naturally occurring rocks (serpentinites and/or peridotites) to form magnesium carbonate (the magnesium analog of limestone), silica (e.g., quartz), and water. The end products are all naturally occurring, and the reaction is actually part of the natural geological carbon cycle. The reaction that produces the magnesium carbonate ($MgCO_3$) also generates energy (heat) that could potentially be harvested. The $MgCO_3$ product is a stable compound, and hence, the disposal is truly permanent. The starting magnesium silicates exist in vast, rich deposits worldwide (Figure 3). For example, a single deposit in Oman contains over 30,000 km^3 of the magnesium

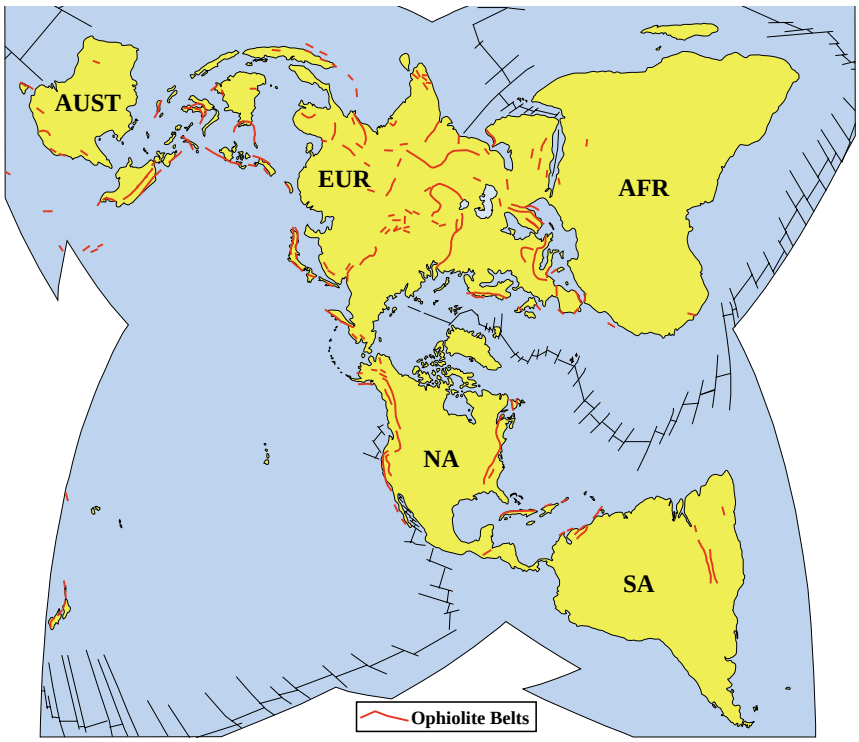

Figure 3. Magnesium Silicate Deposits.
The map shows the location of ophiolite belts that are rich deposits of magnesium silicates. Adapted from work by W. P. Irwin and R. G. Coleman, U.S. Geological Survey 1974.

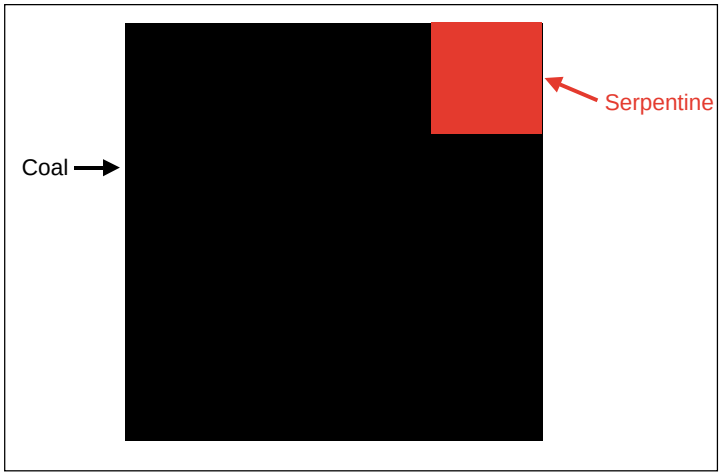

Representative Values
for a 1 GW electric power plant at 80% efficiency

	Coal	Serpentine
Thickness	4 m	200 m
Density	1.4 ton/m^3	2.55 ton/m^3
Use/day	3750 ton/day	25,000 ton/day
Area/day	670 m^2/day	49 m^2/day

Figure 4. Disturbed Surface Areas.
The squares represent the surface areas disturbed in supplying the coal and the serpentine for our high-efficiency zero-emission coal process power plant based on the representative values given above for coal and serpentine deposits.

silicates, which alone could handle most of the world's coal. Taken together, the world's rich magnesium silicate deposits are sufficient to handle easily the entire world's coal supply many times over.

The operation scale required is not unreasonable. The serpentinite mining operation suitable for a large electric power plant is smaller than that for a large, open-pit copper mine. Even though the mineral carbonation requires six times the mass of serpentinite compared to the coal used to produce the CO_2, the surface area disturbed in mining the serpentinite is considerably less than that associated with mining the coal. In contrast to coal seams, serpentinites are typically thick and dense, resulting in a smaller footprint for a serpentinite mine than for a coal strip mine. Figure 4 shows an area comparison for coal mining and serpentine mining, assuming typical deposit values.

The end products of the carbonation process would be used to refill the pit. Based on copper ore mining and milling costs and the likely required plant size for the chemical processing, a disposal cost of approximately $20 per ton of CO_2 would not be unreasonable. With a power plant operating at 80% efficiency, our sequestration approach for CO_2 would cost less than 1 cent per kWh of electricity in the United States.

We believe that coal will likely have an important, and even dominant, position in the energy future for the world. The technological solution we are pursuing with ZECA will allow the realization of "green" coal power, which can be used to ensure a clean world and a long-term, prosperous, healthy, and secure global economy. ■

Further Reading

For additional information on this topic, please contact Hans Ziock (ziock@lanl.gov).

Microhole Drilling and Instrumentation Technology

J. N. Albright (j_albright@lanl.gov) and D. S. Dreesen (EES-11)

For the past five years, the EES Drilling Team, in collaboration with major oil companies and oil-field service providers, has been involved in developing a subsurface exploration capability, termed microhole drilling and instrumentation technology, which promises a very substantial reduction in exploration and development costs. Simple in concept, microhole technology reduces drilled-hole size to the smallest size that is still compatible with good drilling practice and permits the continued access by instruments for subsurface measurements. Figure 1 illustrates microhole diameters relative to conventional oil and gas exploration and production well sizes.

Microholes have from 1/25th to 1/50th of the cross-sectional area of conventional wells. By reducing the terminal-depth hole diameter to sizes in the range of 1 to 2 inches, we expect to substantially reduce the cost of all deep subsurface exploration and characterization. As an example, Figure 2 shows the relative costs of conventional and microhole technologies for a coal-bed methane exploration-and-development project that has been proposed for remote Alaskan villages. The project would supply coal-bed methane for heat and electricity in villages now dependent on diesel-fueled generators for power. Savings in drilling costs result from the smaller drill sites, much smaller draw-works for pipe and tube handling, greatly reduced material for drilling and well completion, and fewer support personnel.

Los Alamos is particularly well qualified to undertake the development of microhole technologies. Over the past 25 years, EES Division and its predecessors have participated in programs contributing to U.S. efforts in geothermal-, oil-, and gas-resource development. As a consequence of these programs, we have acquired extensive exposure to well drilling and completion, well logging technology, and borehole seismic-instrumentation development. Our team's familiarity with well technology has been essential for undertaking a project with the scope and complexity of microhole technology development. Engineering efforts associated with this project encompass evaluating the feasibility of drilling deep microholes; integrating microhole drilling subsystems; field testing bottomhole, coiled-tubing drilling assemblies; miniaturizing geophysical logging tools; and incorporating emerging miniature sensor technologies in borehole seismic-instrumentation packages.

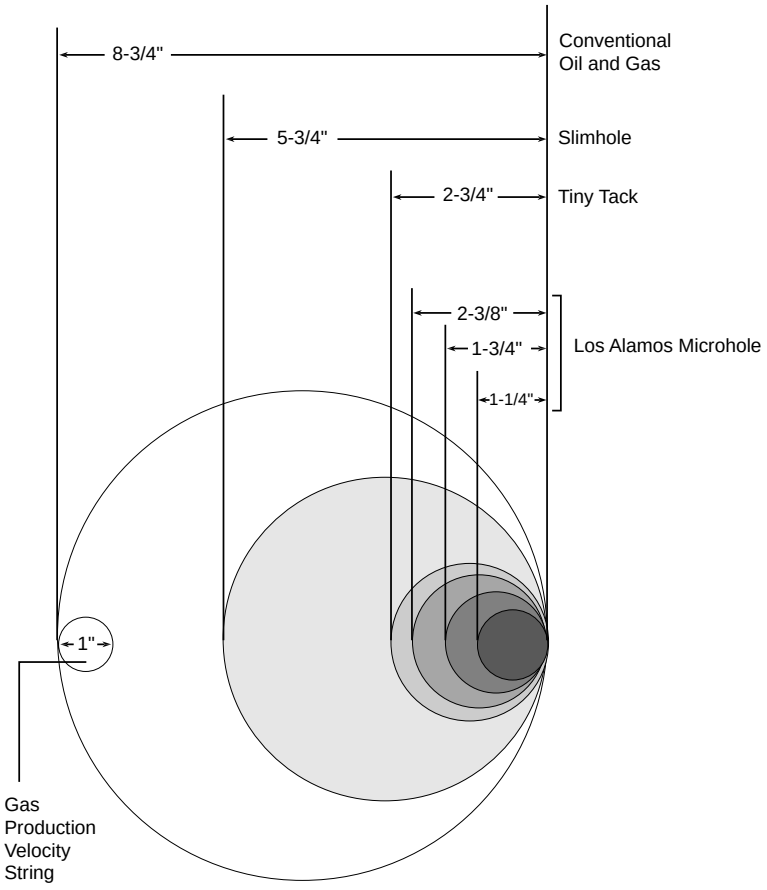

Figure 1. Relative Dimensions of Conventional Wells and Microholes. Our team currently drills microholes 1-3/4″ and 2-3/8″ in diameter with the ultimate goal of drilling deep microholes 1-1/4″ in diameter.

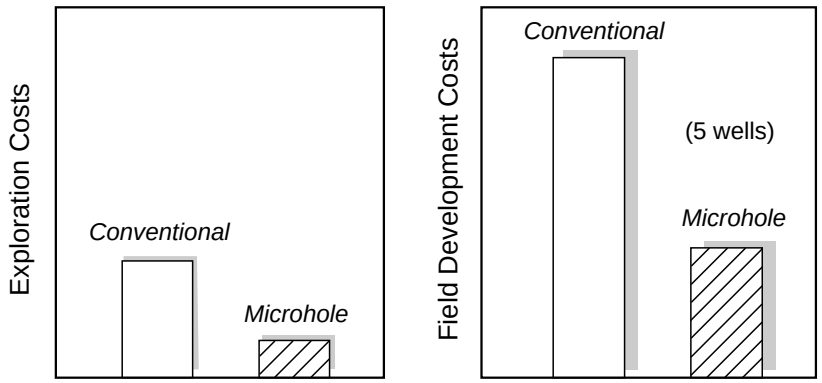

Figure 2. Relative Costs.
The figure illustrates the relative costs of conventional wells and microholes for coal-bed methane exploration and field development in remote Alaska based on cost data for conventional wells obtained by the Division of Geological and Geophysical Surveys of the Alaskan Department of Natural Resources.

Los Alamos Microhole Drilling System

The Los Alamos microhole drilling system, which corresponds in many respects to much larger sized commercial rigs, consists of a mechanical rotary drag bit, a hydraulically powered positive displacement motor, and a coiled-tubing drill stem. This hardware, termed a bottomhole assembly, is deployed for drilling using the coiled-tubing unit that is shown in Figure 3, along with its mud-conditioning and cementing equipment. For the initial tests, we either procured or fabricated components suitable for drilling 1-3/4 in. microholes and then tested them as a bottomhole assembly in an industrial laboratory. Laboratory tests for motor and bit performance demonstrated that these assemblies were suitable for coiled-tubing-supported drilling. Penetration rates in Berea sandstone and Carthage marble exceeded 100 ft/h.

Currently, we are drilling and casing 2-3/8 in.-diameter microholes to depths of 600 ft with the equipment shown. The drilling has been in basin-and-range valley fill and volcanic tuff. In the five wells drilled to date, we have encountered no problems that we would not expect to see in conventional drilling, and the problems were successfully addressed with conventional methods. As microholes are drilled deeper, we expect that conventional methods will have to be modified, if not replaced with advanced technology.

Logging Tools and Borehole Instrumentation

We have begun designing and fabricating a basic suite of 7/8 in.-diameter logging tools that will include both spectral-gamma and electrical-resistivity tools. It will also include a capability for surveying the trajectory of completed microholes. Furthest along in development is the gamma tool, which will be used to measure the natural radioactivity of rock penetrated by microholes.

Microhole Gamma Tool. The radiation incident on a sensor deployed in a microhole will always be greater than that for a conventional tool in a cased 8-1/4 in. hole. Figure 4 demonstrates this with an approximate calculation for the relative gamma radiation incident at three different energies on gamma-ray detectors packaged in cylindrical 7/8 in.-diameter and 3-1/4 in.-diameter stainless steel logging-tool housings.

In the foregoing calculation, we take into account only the absorption of gamma rays propagating perpendicular to the borehole. Off-normal flux components will also be greater for the microhole tool because of the closer proximity of the rock above and below the sensor in a microhole. The increased gamma flux incident

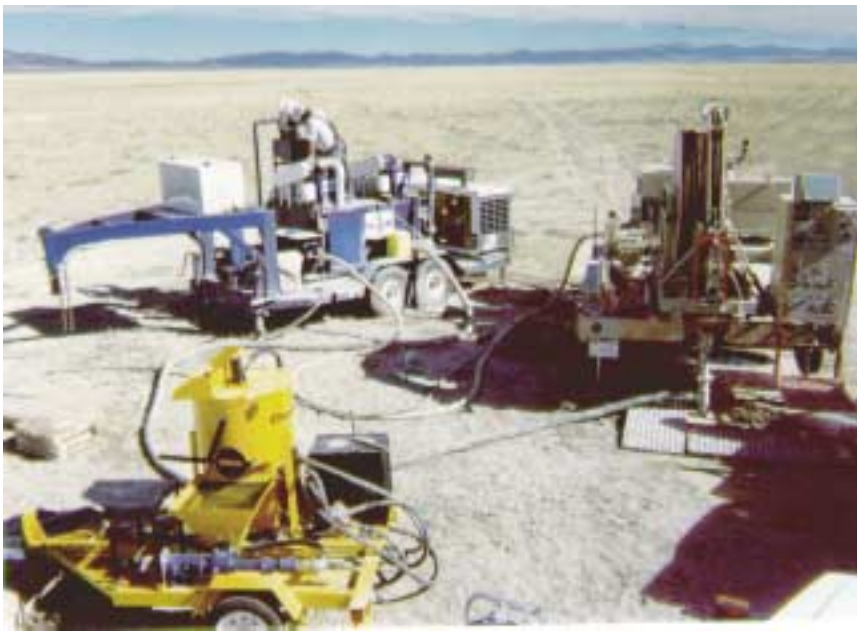

Figure 3. Drilling Systems.
The microhole drill rig (upper right), mud system (upper left), and batch cement mixer (lower left) at a field site in central Nevada are being used to drill microholes for emplacement of seismic-instrumentation packages.

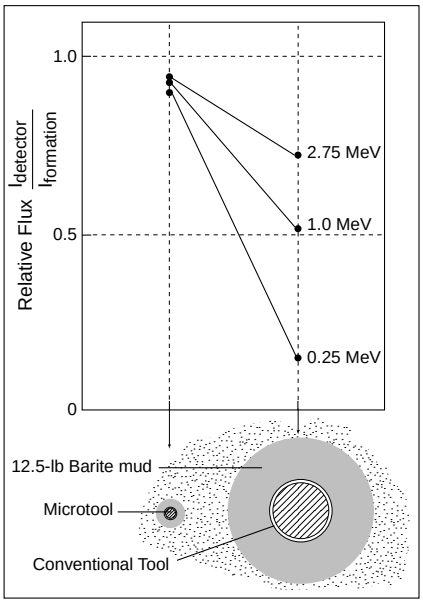

Figure 4. Relative Flux.
The figure shows the calculated relative gamma flux incident (left) on a 7/8 in. diameter sensor package in a 1-3/8 in. microhole and (right) on a commercial 3-3/8 in. logging tool in an 8-1/4 in. production well. Both tools are in open boreholes filled with barite mud.

on the microhole tool, however, is offset by the reduced photopeak-detector efficiency inherent in its smaller sensor.

Theory dealing with the gamma-capture efficiency of NaI crystals—the material most commonly used for gamma-ray detection in borehole logging tools—has yet to deal effectively with cylinders of the high aspect ratios found in logging tools. Consequently, a calculation of their relative photopeak efficiency was not practical. To address this question, we designed and fabricated a microhole gamma tool to compare its efficiency directly with that of a conventional tool. Making this comparison early in the microtool design effort is important if we are to determine the relative counting time for the two tools in a constant gamma flux. If the microtool's counting time is excessively long compared with that of the commercial tool, we will have to increase the mass of the NaI crystal in the final microtool design.

Figure 5 compares counts registered on a microtool detector assembly with those of a commercial logging tool over the energy range of 100 to 2,000 keV. In this case, there is no absorbing medium between a bismuth-207 point source and the respective tool housings; the measurement is done in air. The results show that the photopeak efficiency of the microtool NaI crystal is greater than 0.4 times that of the commercial tool, reaching up to roughly 1,200 keV and then decreasing rapidly.

We designed a test setup to compare the overall performance of the microtool with that of a commercial tool, while taking into account the competing effects of increased flux and reduced photopeak efficiency, over a range of borehole diameters, casings, and fluids. The test setup consists of a potash-filled barrel in which various combinations of casing and gamma tools can be easily inserted for spectral gamma measurements. Once the comparative measurements are completed, we will be able to determine the crystal mass required for the microhole tool's performance to match that of the commercial tool.

Microhole Resistivity Tool. The Cedar Bluff Group, a company specializing in formation resistivity measurements for the oil industry, recently completed a comprehensive review of all types of resistivity/conductivity tools and the relative merits of their use in microholes for EES Division. They reviewed data on focused and unfocused electrodes and low- and high-frequency induction logging tools.

Cedar Bluff identified the special constraints imposed on tool design by the 7/8 in.-diameter limitation and analyzed the constraints, along with estimating the performance limitations of the various types of tools. They found that, although electrode tools are less affected by diameter, they still present some significant mechanical design challenges. Cedar Bluff also reviewed the environmental factors affecting performance, comparing the relative effects on conventional and microhole resistivity logging of the following: drilling muds, casing, post-completion borehole fluids, invasion, and rocks possessing conductivity extremes.

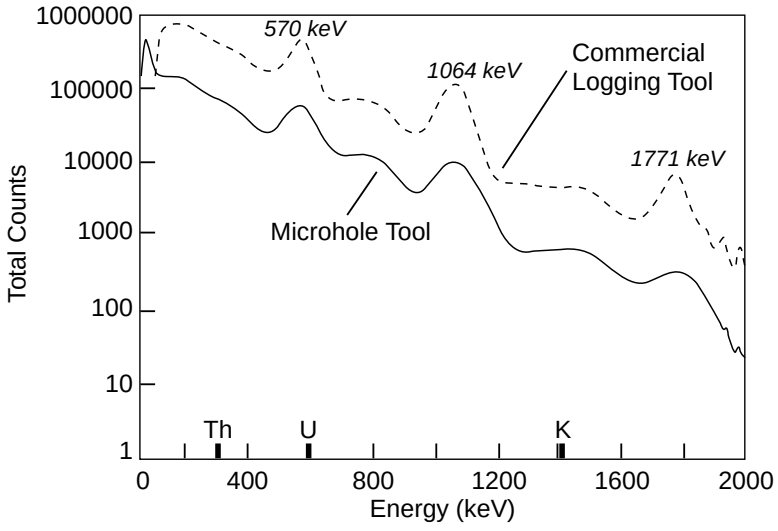

Figure 5. Count Comparison.
The figure compares total counts for 1-11/16 in. commercial and 7/8 in.-diameter microhole gamma tools using a point bismuth-207 source. The source is located 4 in. from the center of a NaI crystal in each tool. The length and radius of the crystals are 6 x 1 in. and 4 x 1/2 in., respectively.

The small available cross-sectional area in a microtool compels us to use the higher-frequency induction tools to compensate for the reduced sensitivity of the small transmitting and receiving coils. High-frequency tools provide a higher resolution than current commercial logging tools in conventional-size wells. The Cedar Bluff Group has recommended the development of a high-frequency induction tool consistent with current state-of-the-art design in microhole logging tools.

Microhole Seismic Array Design, Fabrication, and Testing

Our team, capitalizing on Input/Output, Inc. (IOC) in-house microelectromechanical systems (MEMS) accelerometer technology, designed, fabricated, and tested two four-level, three-component seismic arrays, which were based on a successful prototype. To the best of our knowledge, this is the first reported use of the MEMS technology for a borehole seismic array.

We substantially redesigned the prototype 7/8 in.-diameter borehole package, which provides initial information on the performance of the MEMS sensor, to serve as an interchangeable sensor pod in a multipod-array system. In collaboration with Phillips Petroleum, we then deployed the arrays to (1) demonstrate that successful deployment in and retrieval from microholes was possible, and (2) evaluate the potential contribution that data from microhole arrays could make to seismic-reflection surveying.

With respect to our first objective, four 2-1/4 in.-diameter microholes were drilled to depths of between 300 and 500 ft using the Los Alamos coiled-tubing drilling unit. These wells were cased by grouting in 1-1/4 in.-inside-diameter flush-joint PVC tubing. A subcontractor to Phillips Petroleum collected two-dimensional reflection data simultaneously from conventional surface geophone arrays and from the two MEMS microhole arrays using IOC's System-2 data-acquisition equipment. The arrays were successfully deployed and retrieved without incident.

So far, borehole field data results indicate comparable sensitivity; however, these data also indicate a lower signal-to-noise ratio than that of nine-geophone gathers used in a reflection line. Array noise levels gradually declined with the depth of each array pod, and the horizontal array elements recording the elastic waves showed lower amplitude motion than did the verticals.

Conclusions

At this stage in our study of microhole technology, we have not found any fundamental technical barriers either to the drilling of deep microholes or to their instrumentation for a variety of applications. Rather, microhole technology appears to offer the prospect of improved subsurface measurements at greatly reduced cost. ■

Further Reading

Albright, J. N. 2000. Microhole technology—progress on borehole instrumentation development. In *Seventh International Symposium on Borehole Geophysics for Minerals, Geotechnical, and Environmental Applications, Golden, CO, Oct. 24–26*.

Albright, J. N., and D. S. Dreesen. 2000. Microhole technology lowers reservoir exploration characterization costs. *Oil and Gas Journal* **98:** 39–41.

Albright, J. N., J. C. Gannon, T. D. Fairbanks, and J. T. Rutledge. 1999. Borehole testing of a micromachined silicon accelerometer. *Society of Exploration Geophysicists International Exposition and 69th Annual Meeting, Houston, TX, Oct. 31–Nov. 5*.

Dreesen, D. S., and J. N. Albright. 2000. Models support potential for drilling deep microholes. *Oil and Gas Journal* **98**: 56–58.

Dreesen, D. S., and J. H. Cohen. 1997. Investigation of the feasibility of deep microborehole drilling. In *Proceedings of 8th Annual Energy Week Conference and Exhibition*, Vol. I, Book III, p. 137. Houston, TX: American Society of Mechanical Engineers.

Sinclair, P. 2000. Resistivity tools for microhole logging. Los Alamos National Laboratory document LA-UR–00-5971.

Thomson, J. C., J. Hufford, and D. S. Dreesen. 1999. Coiled-tubing microdrilling demonstration in basin and dry lake sediments. Los Alamos National Laboratory document LA-UR-99-5310.

The ARM Program in the Tropical Western Pacific

W. E. Clements (clements@lanl.gov) and L. A. Jones (EES-8), F. J. Barnes (EES-10), and M. D. Ivey (SNL)

The Department of Energy's Atmospheric Radiation Measurement (ARM) program was created in 1989 as part of the U.S. Global Change Research Program. The overall goal of the ARM program is to develop and test parameterizations of important atmospheric processes, particularly cloud and radiative processes, that will be used to improve atmospheric models. This goal is being achieved using a combination of field and modeling studies.

A key ARM precept is that observers and modelers should work together, using field data to develop and validate parameters. ARM's objective is to produce measurements suitable for testing parameters in a sufficiently wide variety of situations so as to span the range of climatologically relevant possibilities. To accomplish this, we need very detailed measurements of radiation and optical properties at the Earth's surface, inside the atmospheric column, and at the top of the atmosphere.

ARM's primary observational methods are remote sensing of clouds, water vapor, and aerosols. It is impossible to meet ARM's objectives, however, without obtaining a large volume of detailed in situ measurements, some of which will have to be acquired from manned or unmanned aircraft. In addition, high-quality satellite observations are needed to measure the top-of-the-atmosphere radiation.

To obtain the required in situ and surface-based remote-sensing data, ARM has been making measurements at three locales using atmospheric radiation and cloud stations (ARCS), as well as acquiring satellite data from other programs. The three locales, shown in Figure 1, are the southern Great Plains of the United States (SGP), the tropical western Pacific (TWP), and the north slope of Alaska and adjacent Arctic Ocean (NSA/AAO). The TWP location, on which we will focus, is managed by the ARM TWP Program Office in EES Division and began phased operations in 1996.

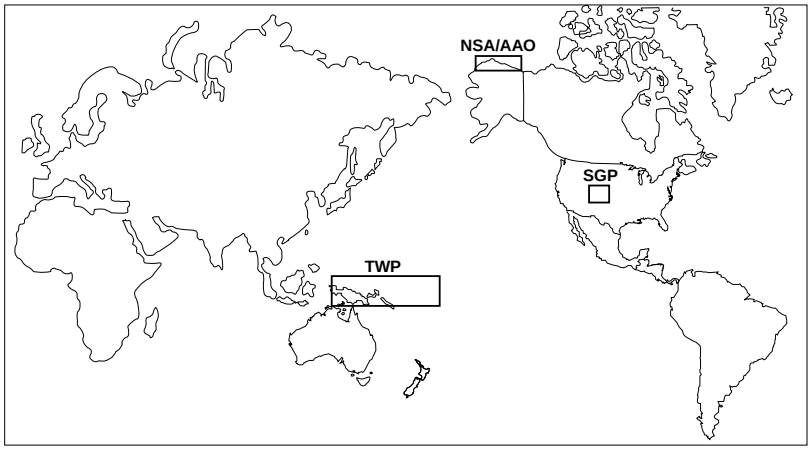

Figure 1. Locations of the three primary ARM locales.

The SGP, which began operating in 1992, covers approximately 55,000 square miles in north central Oklahoma and south central Kansas. The NSA/AAO began in 1997. ARM plans to collect data in each location for at least 10 years.

The TWP Locale

The TWP locale is a large expanse of tropical ocean and maritime continent, lying roughly between 10°S and 10°N latitude and from 135°E to 150°W longitude (Figure 2). The maritime continent area is largely in the southwest, and the open ocean area is in the northeast of the locale. Climatologically, warm sea-surface temperatures, deep and frequent atmospheric convection, high rain rates, strong coupling between the atmosphere and ocean, and substantial variability associated with the El Niño-Southern Oscillation phenomenon characterize the locale. The relationship between climatic variability in this region and variability in other areas of the Earth is well known.

We are addressing three questions in the TWP: radiation budget and cloud forcing, water and energy budgets, and ocean-atmosphere interactions. The large geographic expanse of the TWP, as well as logistical and financial constraints, have influenced our observational strategy, which follows:

(1) Gather a long-time series of basic observations at several locations that will aid in understanding intraannual and interannual variability of surface radiation fluxes and cloud properties.

(2) Conduct intensive field campaigns, which augment radiation and cloud observations, to study the role of deep convection in the tropics on radiative processes.

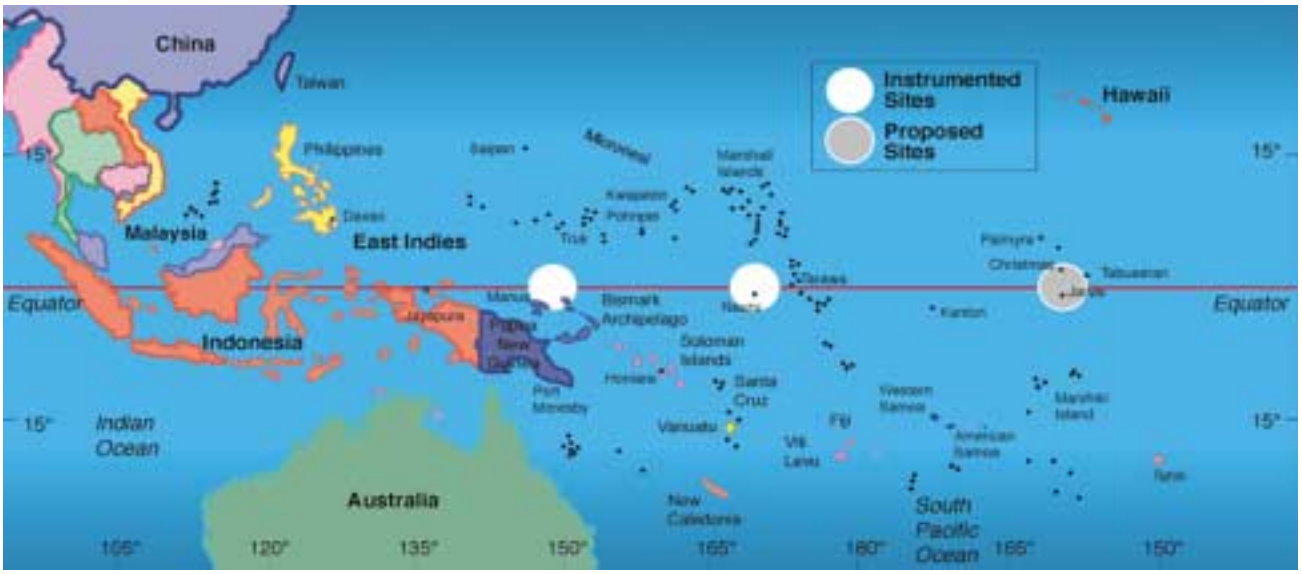

Figure 2. The Tropical Western Pacific Sites.
This map of the equatorial western Pacific region shows the TWP locale and existing and proposed ARCS sites.

(3) Devise and implement a strategy for long-term measurements of ocean-atmosphere properties and fluxes.

The first element of our strategy is most important for two reasons: it relates directly to the primary scientific questions articulated by the ARM Program, and it addresses the lack of data on long-term radiation in the TWP locale.

Atmospheric Radiation and Cloud Stations (ARCS)

To study long-term radiation and cloud properties, ARM uses ARCS, which were designed to collect this type of data. An ARCS system, which is housed in custom modified 20-ft-long sea containers, consists of an integrated instrument set that measures the surface radiation balance, surface meteorology, cloud properties, and some limited atmospheric quantities. In addition to the suite of scientific instruments, a station contains data acquisition systems, monitoring and control systems, satellite communications, a backup electrical generator, a hydrogen generator, and other support equipment. The ARCS system is self-contained and designed to operate semi-autonomously with a minimum of on-site support.

The need to measure the effect of tropical clouds and water vapor on the surface radiation budget is the main scientific driver for the set of observations made by a station. Table 1 summarizes the general measurement categories and the instruments used to obtain them.

Hourly health and status data from the ARCS are transmitted via satellite and are available on the Web. The health and status data provide information on how well the instruments are performing and the condition of support equipment. All of the ARCS data are written to magnetic tapes and periodically shipped back to the United States.

Siting Strategy

An important property of the climate in the tropical Pacific is a strong east-to-west gradient in various climate parameters, including sea-surface temperature, water-vapor column, and frequency of convection. High sea-surface temperatures and frequent deep convection characterize the TWP. Toward the eastern Pacific, there is a steady decline in sea-surface temperature and a corresponding decrease in the frequency of convection. An El Niño is a deviation from these typical east-to-west gradients. Because of this longitudinal structure and its variability, it would be difficult to characterize the climate of the TWP using a single site. ARM plans to deploy ARCS at three sites to sample the structure in this region. Figure 2 shows the existing and proposed locations of the three TWP sites. The third site in the eastern Pacific is currently on hold pending scientific and budgetary considerations.

The Manus Site

The first TWP ARCS site was established in Manus Province, Papua, New Guinea, in 1996 (Figure 2). This was the first site selected because it is within the heart of the Pacific warm pool and is supported by the Papua National Weather Service. The site is located at their weather station at the Momote airport on Los Negros Island at 2.060°S, 147.425°E (Figure 3).

The site is 6 m above mean sea level, and all equipment is located within the weather station compound (Figure 4). Collection of data began in October 1996.

The Manus site has been operating and providing data to the ARM Experiment Center for three years. A global positioning rawinsonde system

Table 1. ARCS Measurements and Instruments.

Measurement	Instrument
Surface Radiation Balance	Up- and down-looking pyranometers and pyrgeometers Sun-shaded pyranometer and pyrgeometer using solar tracker Normal incidence pyrheliometer Up- and down-looking 9–11-mm narrow-field-of-view radiometers UV-B hemispheric radiometer Broadband (solar and infrared) net radiometer
Surface Meteorology	Temperature and relative humidity sensor Barometer Optical rain gauge Propeller vane anemometer Sea-surface temperature measurement[1]
Cloud Properties	Cloud lidar (523 nm) Ceilometer (7.5-km maximum range) 35-GHz cloud radar Whole Sky Imager (WSI)
Aerosol Optical Depth	Multifilter rotating shadow band radiometer (total, direct, and diffuse irradiance in six 10-nm channels)
Column Water	Dual channel (23.8 and 31.4 GHz) microwave radiometer
Vertical Structure of Atmosphere	Rawinsonde 915-MHz wind profiler with RASS[2]
Atmospheric Emitted Radiation	Atmospheric Emitted Radiance Interferometer (AERI)[1]

[1]Nauru site only
[2]Operated in cooperation with NOAA's Aeronomy Laboratory

was added in August 1997, and a whole-sky imager was installed in August 1998. The instrument suite was completed in early 1999 with the addition of a 35-GHz cloud radar.

The Nauru Site

The second TWP site was established on Nauru Island at 0.521°S, 166.916°E in November 1998. We chose this site because of its location on the eastern edge of the warm pool under La Niña conditions.

The site is located in the Denigomodu (Denig) District on the northwest shore of the island (Figure 5) and is operated in collaboration with the Nauru Department of Island Development and Industry.

Nauru99 Campaign

During June and July of 1999, the Nauru ARM site was host to the Nauru99 Scientific Research Campaign. Nauru99 was an international study of climate in the vicinity of Nauru Island in the TWP. Study participants included the DOE, the National Oceanic and Atmospheric Administration (NOAA), the Japanese Marine Science and Technology Center, Airborne Research Australia, and the Nauruan

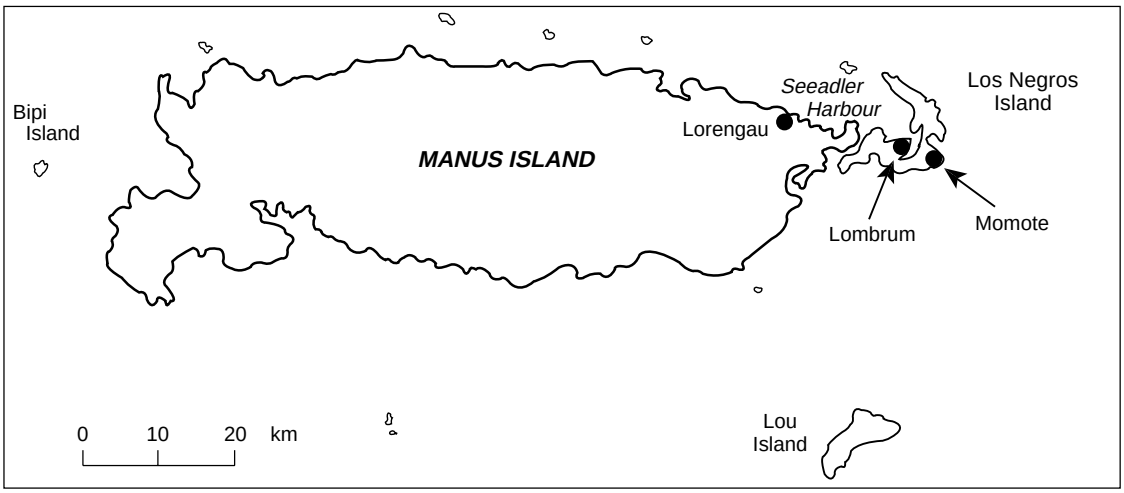

Figure 3. The Manus Site.
The ARCS site is located at the National Weather Service station at the Momote airport on Los Negros Island in Papua, New Guinea.

Figure 4. Manus Weather Station.
The ARCS installation at the National Weather Service station at Momote airport, Manus Province, Papua, New Guinea.

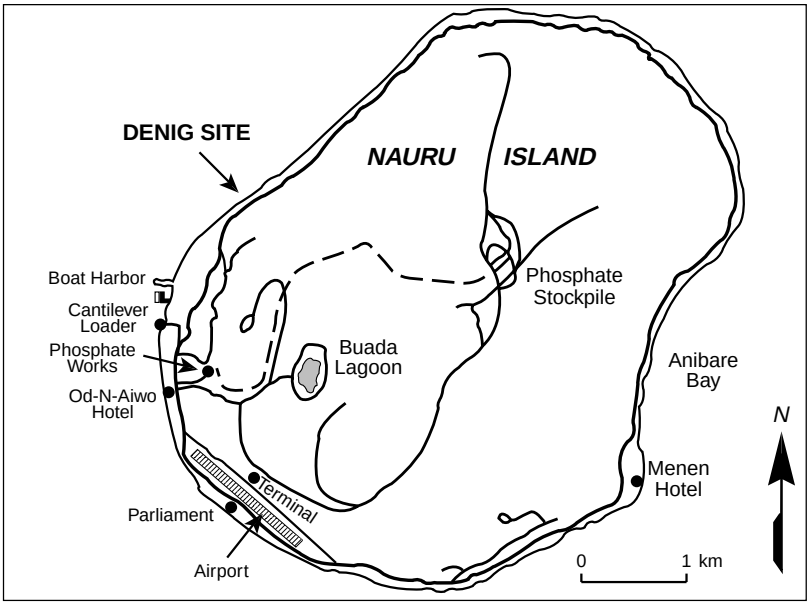

Figure 5. The Nauru Site.
The map shows the Denig Site on the northwest shore of Nauru Island.

Government. The main goal of Nauru99 was to improve our understanding of radiant heat transfer and the effects of clouds on ocean weather processes in the tropics using land-, air-, and ocean-based measurements. Nauru99 also collected data to look at possible island effects on the island-based measurements.

Educational Outreach

ARM also conducts an Education Outreach Program in each locale to complement local and regional education in the areas of basic science, meteorology, and climatology. This program is discussed in the Project Descriptions section of this report. ■

Acknowledgements

The DOE Office of Biological and Environmental Research sponsors the ARM Program. The program draws on the resources of most of the U.S. national laboratories, several universities, and other national and international agencies and contractors. The Manus site operation is a collaborative effort with the Papua, New Guinea, National Weather Service and that of the Nauru site with the Department of Island Development and Industry on Nauru. Operation of the wind profilers at Manus and Nauru is a cooperative effort with NOAA's Aeronomy Lab. The Tropical Western Pacific Program Office works closely with the South Pacific Regional Environment Programme in all aspects of the implementation and operation of the TWP program.

Further Reading

DOE. 1990. *Atmospheric Radiation Measurement Program Plan*. Reports DOE/ER-0442 (Executive Summary, 19 pp.) and 0441 (116 pp.). Springfield, VA: U.S. Department of Commerce, National Technical Information Service (707-487-4650).

DOE. 1990–1999. *Proceedings of the Atmospheric Radiation Measurement (ARM) Science Team Meetings*. Annual DOE reports. Springfield, VA: U.S. Department of Commerce, National Technical Information Service (707-487-4650).

Mather, J. H., T. P. Ackerman, W. E. Clements, F. J. Barnes, M. D. Ivey, L. D. Hatfield, and R. M. Reynolds. 1998. An atmospheric radiation and cloud station in the tropical western Pacific. *Bulletin of the American Meteorological Society* **79**: 627–642.

National Tidal Facility. 1998. *Curriculum Modules for the Pacific Schools—Climate Change and Sea Level; Part One: Physical Science.* ISBN: 0-7258-0637-0. Bedford Park, South Australia: National Tidal Facility (618-8201-7611).

Stokes, G. M., and S. E. Schwartz. 1994. The Atmospheric Radiation Measurement (ARM) Program: Programmatic background and design of the cloud and radiation test bed. *Bulletin of the American Meteorological Society* **75**: 1201–1221.

ARM Web Site: www.arm.gov.

Advances in Microscale Atmospheric Modeling

J. E. Bossert (ALDTR), R. R. Linn (rrl@lanl.gov), J. M. Reisner, S. Smith, and J. Winterkamp (EES-8)

The Atmospheric and Climate Sciences Group's recent advances in numerical modeling of small-scale phenomena in the atmosphere are based on two models, the HIgh GRADient applications model, HIGRAD, and a physics-based wildfire-behavior model, FIRETEC. These codes have allowed us to simulate atmospheric phenomena at very high spatial resolution on LANL's supercomputers. Results from the application of HIGRAD/FIRETEC have greatly increased our physical understanding of atmospheric flows in the presence of strong heat sources and topographic obstacles. Specific examples, which are discussed below, highlight these accomplishments.

Modeling System

The high-resolution, strong-gradient applications model, HIGRAD, solves the compressible forms of the conservation equations for mass, momentum, energy, oxygen, and other chemical species of interest in the atmosphere. HIGRAD uses numerical techniques that are fully second-order in time and space, include monotonicity constraints to handle the over- and under-shoots associated with representing strong gradients numerically, and minimize numerical diffusion that tends to diminish steep gradients with time.

Small-scale physical processes relevant to wildfires are represented in the FIRETEC combustion/turbulence-closure model. FIRETEC was developed to simulate wildfire behavior by representing the underlying physical processes that control wildfires (coupling atmospheric flows with large heat sources, mixing-limited chemical reactions, transport of reacting chemical species, etc.). FIRETEC also incorporates a turbulence transport scheme that represents the turbulence generated by the vegetation. It accounts for the microscopic details of a fire with macroscopic resolution by dividing quantities into mean and fluctuating parts similar to the approach used in traditional turbulence modeling. These divided quantities include fuel, wind, and gas concentrations.

Combining these two models into HIGRAD/FIRETEC allows simulation of dispersion of atmospheric pollutants associated with wildfires or other sources. The numerical techniques used make HIGRAD/FIRETEC especially useful for modeling circumstances such as abrupt changes in either boundary conditions (e.g., the complex terrain of the LANL site or of an urban area—surface boundary conditions) or internal-state variable structures (e.g., strong temperature inversions in the atmosphere). Three examples of HIGRAD/FIRETEC applications are discussed below.

Using Spatial Fuels Data to Investigate Wildfires

In one of the more interesting tests of HIGRAD/FIRETEC applied to real wildfires, we simulated a small portion of the 16,000-acre Calabasas fire that occurred on 21 to 22 October 1996 in the Santa Monica Mountains of Los Angeles County, California. Our simulation was limited to an intense fire—a blowup—that occurred in an isolated canyon around noon on 22 October. Overall, the Calabasas incident was a typical Santa Ana wind-driven conflagration that burned from Highway 101 southwestward to the Pacific Ocean on 21 October. That night, however, the offshore winds eased, allowing residual fire lines to be affected by the normal onshore sea breeze during the morning of 22 October.

Our study area, Corral Canyon, is a north-south oriented 4-km-long watershed running between the crest of the Santa Monica Mountains (~700 m above sea level) and the Pacific Ocean. At the bottom of the canyon is a narrow riparian corridor resistant to burning. At the time of the Calabasas fire, the steep slopes of the canyon were densely covered in typical coastal chaparral vegetation.

We used AVIRIS, an aircraft-borne remote sensing spectrometer that images some 220 wavebands in the visible and near-infrared portions of the spectrum, to create the appropriate model data sets related to the spatial variability of these fuels (Figure 1). Differential analysis of reflected sunlight in these wavebands allows discrimination of surface properties, including types of ground cover and, thus, fuels.

This study constituted one of the first attempts to use the HIGRAD/FIRETEC model with both "coarse" resolution and real topography. The model resolution was 10 m in the horizontal and 5 m in the vertical—considerably coarser than our idealized fire simulations that use resolutions of 2 m or less. For computational efficiency, we stretched the vertical coordinate over

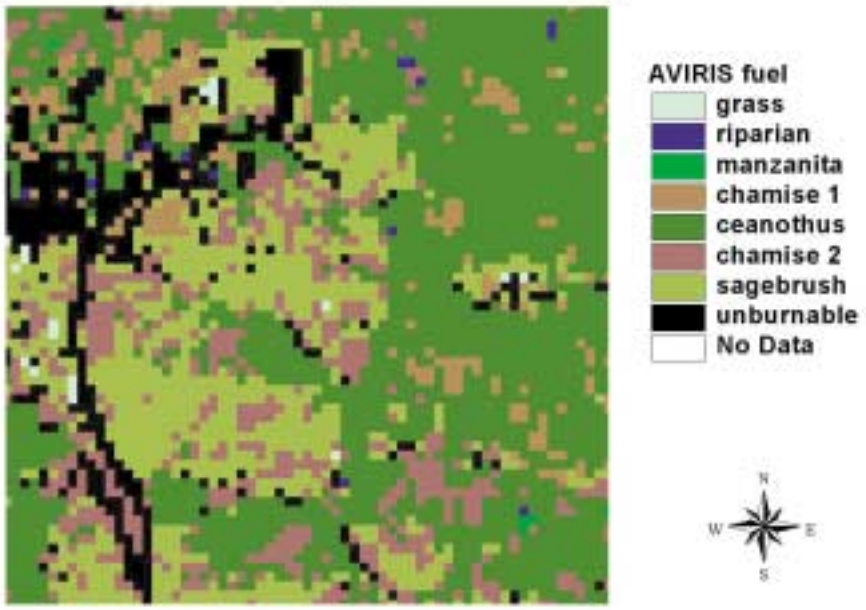

Figure 1. Fuels in the Corral Canyon Study Area Derived from AVIRIS Data. The black (unburnable) area represents an asphalt road on a ridge to the west of the Malibu Bowl and housing developments on the north rim of the Bowl. The various fuel species are collectively termed "chaparral" in local terminology. The riparian corridor where the fire ignited is not shown here. This area is represented in three-dimensional perspective in Figure 2.

26 layers following a geometric progression, which established the model top at 1.3 km. The simulation domain was a 1.27-km (128-grid-cell) square, and it incorporated a topographic slice through the bottom of Corral Canyon at 10-m resolution for the lower boundary.

The Calabasas fire burned near the bottom of the canyon during the late morning of 22 October, driven by weak sea breezes. Just after noon, a fire blowup occurred on the steep slopes of the Malibu Bowl, halfway up the canyon. Several firefighters, protecting a subdivision at the top of the Bowl, were overtaken by flame lengths in excess of 100 ft during the fire blowup, and one firefighter was severely burned.

Our HIGRAD/FIRETEC simulation was able to capture many features of the actual fire behavior as related by firefighting professionals on the scene. Figure 2 shows that our simulated fire raced up the steep slopes of the Malibu Bowl after smoldering in the riparian fuel at the bottom of the canyon for 17 min following ignition. Over the course of 15 min, our simulated fire progressed rapidly up the ridgeline at the right edge of the bowl, exactly where the firefighter, defending a home, was severely burned by the real fire. Next, our simulated fire burned out the entire Malibu Bowl in the following 5 min, exhibiting extreme behavior in terms of flame lengths, vertical velocities, and fire temperatures. Our results are consistent with observations and with the aftermath of the fire, in which the lush vegetation within the Bowl was reduced to mineral ash, indicating the intensity of the burn.

HCl Dispersion from a Shuttle Abort Scenario

A second application of HIGRAD/FIRETEC, one that we hope will never represent real circumstances, concerns both fire and the dispersion of its combustion products. In this study, we used the combined model to examine the emissions associated with a potential catastrophic abort of a launch of the NASA Space Shuttle.

Abort procedures within the first 20 s after launch would result in an explosive fragmentation of the Shuttle's solid rocket boosters. In such a scenario, the hazards associated with emissions from the burning booster, which would produce

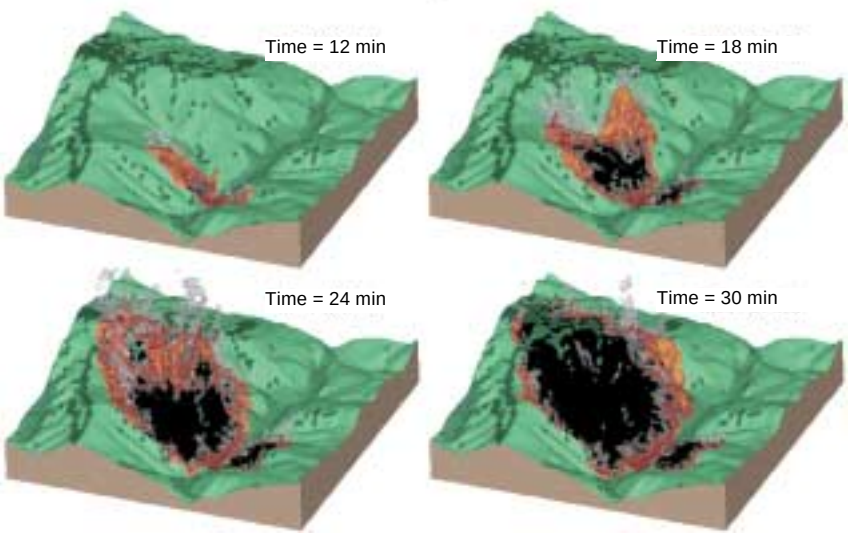

Figure 2. FIRETEC Wildfire Simulation. In these snapshots, green represents unburned vegetation, black represents completely burned areas, and the other colors are keyed to model temperatures of the simulated Corral Canyon portion of the Calabasas fire. The progression of the fire in this simulation corresponds to (qualitative) observations by firefighting professionals at the scene.

hydrochloric acid (HCl) gas, pose a potential exposure risk to launch visitors and nearby communities, a true cause for concern. To evaluate this potential risk, we simulated the abort scenario and analyzed the dispersion of HCl released after the rocket booster fragments reached the ground. This analysis was conducted under the guidance of the NASA Biomedical Office at the Kennedy Space Center.

To address the concerns about the potential HCl hazard, we developed a worst-case scenario that included identifying weather conditions to evaluate the predicted size and shape of the solid rocket booster debris field, the burning characteristics of the booster, and the HCl emissions and their transport. HIGRAD/FIRETEC was then used to simulate the atmosphere's response to the intense heat emitted by the burning booster fragments. We also simulated emission of HCl in the gaseous and aqueous phases in the vicinity of the shuttle launch pad and subsequent transport downstream toward the NASA causeway and Port Canaveral. To make these simulations as accurate as possible, we developed representations in HIGRAD/FIRETEC for (1) the production of heat and HCl emitted from the rocket booster fragment distribution patterns, (2) the depletion of the fragments with time, and (3) the deposition of HCl on vegetation and water surfaces.

The simulation itself was divided into two parts, each representing a different phase of the transport of HCl from the burning fragments to points of interest downwind. The first part consisted of modeling the emission of gas (HCl and other gases) and heat from the rocket fragments and the atmospheric response to these emissions. This *near-field* simulation required high resolution (~20 m) to capture the strong buoyancy-driven flows resulting from the heat released by the fragments. The physical domain for this part of the analysis was taken to be 4.8 km along-wind by 4 km across-wind by 10 km high.

Figure 3 shows a snapshot of the HCl plume from the near-field simulation when the discrete fragment emission pattern is combined with real meteorological conditions from 23 November 1995, a day chosen to enhance our simulation of a worst case. The two features of interest are the significant amount of the plume that is trapped near the ground and between about 900 and 1,000 meters above the ground. This trapping, associated with two strong atmospheric temperature inversions at these levels, is similar to that seen in nighttime pollution episodes in urban areas.

The second part of the simulation consisted of modeling the *far-field* transport of gaseous HCl downwind after the booster fragments finished burning and the atmospheric response relaxed from the strong vertical motions associated with the burning process. To simulate this downwind transport required a larger physical domain, approximately 28 km along-wind by 12 km cross-wind by 10 km high. Consequently, we used coarser horizontal grid resolution than in the near-field case. In the far-field simulation, it was also important to consider additional processes associated with transport of the HCl downwind, particularly the deposition of HCl onto the vegetation. Based on the initial near-field dispersion and the deposition and dilution processes in the far-field domain, we were able to conclude that HCl concentrations, even in a worst case such as we used, would be below Environmental Protection Agency (EPA) hazard levels.

Building Flow Simulations

This third application of the HIGRAD/FIRETEC microscale atmospheric modeling system illustrates both the model's flexibility and its robust character. Although this application does not involve fire, the turbulence closures in FIRETEC play an important role in the results of this study, in which we investigate the dispersal of atmospheric contaminants within the urban environment. We focus here on the equivalent of the near-field results discussed in the last section; additional work, the

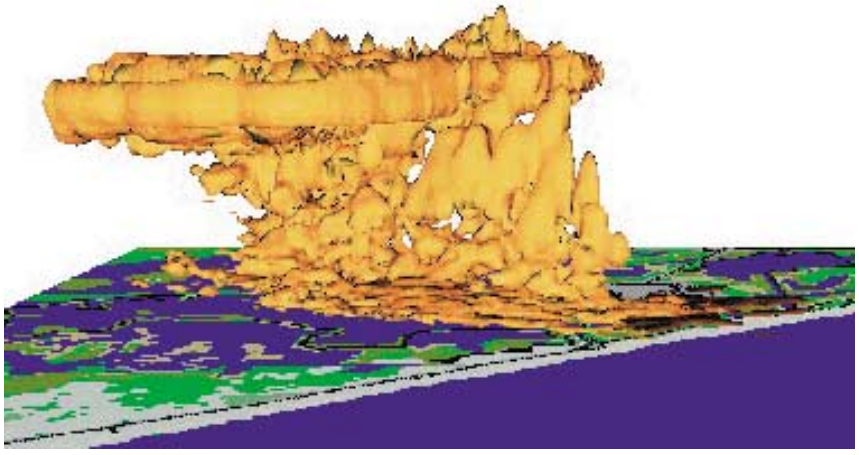

Figure 3. Near-Field Simulation of Shuttle Abort.
The HCl cloud is depicted using its 20-points-per-million isosurface in the near-field domain shortly after the Shuttle abort process. In this simulation, the large-scale wind field blows from right to left, spreading the cloud downwind from its ignition point (the blackened area near the "coast"). The areas of widespread HCl near the surface and at the top of the cloud are associated with temperature inversions in the meteorological conditions used.

analog of the far-field study discussed above, is in progress.

In preparation for the 2002 Winter Olympic Games to be held in Salt Lake City, Utah, we have simulated the effects of a release of an unspecified agent at the Delta Center, the Olympic skating venue. In the event of a release of a chemical or biological agent at such a large indoor event, the pollutant would diffuse throughout the interior of the building and would likely be exhausted to the atmosphere through the heating, ventilation, and air-conditioning ducts, thus exposing the population in the vicinity of the building. Our work does not concern dispersion in the interior of the Delta Center; rather, we have specified a continuous release of a passive tracer for a finite duration at the location of the air-conditioning vents as a way to investigate subsequent transport in the atmosphere outside the building.

These near-field simulations (Figure 4) use a single building on flat terrain in neutral atmospheric stratification. The dispersion shown is non-Gaussian with a substantial amount of the tracer trapped in the building recirculation zone. The concentration contours that seem unconnected with the building wake region are caused by the vents located on the upstream side and transport over the building. These results show that significant variability in concentration of hazardous agents could be located in the lee of the building for extended periods.

Validations. To validate these simulations and provide a basis for confidence in more complex simulations that include several buildings (the far-field case), we have compared HIGRAD/FIRETEC results with wind-tunnel experiments. These model validation runs used data obtained from a recent EPA wind-tunnel study of the flow field around a two-dimensional array of "buildings." These buildings consisted of seven evenly spaced rectangular blocks of equal height (H) and downwind length of 0.15 m. The spacing between each building row was H, and the building rows spanned the horizontal (cross-wind) extent of the wind tunnel. A neutral atmospheric boundary layer was simulated in the wind tunnel by stirring the flow with spires and floor roughness elements upstream of the

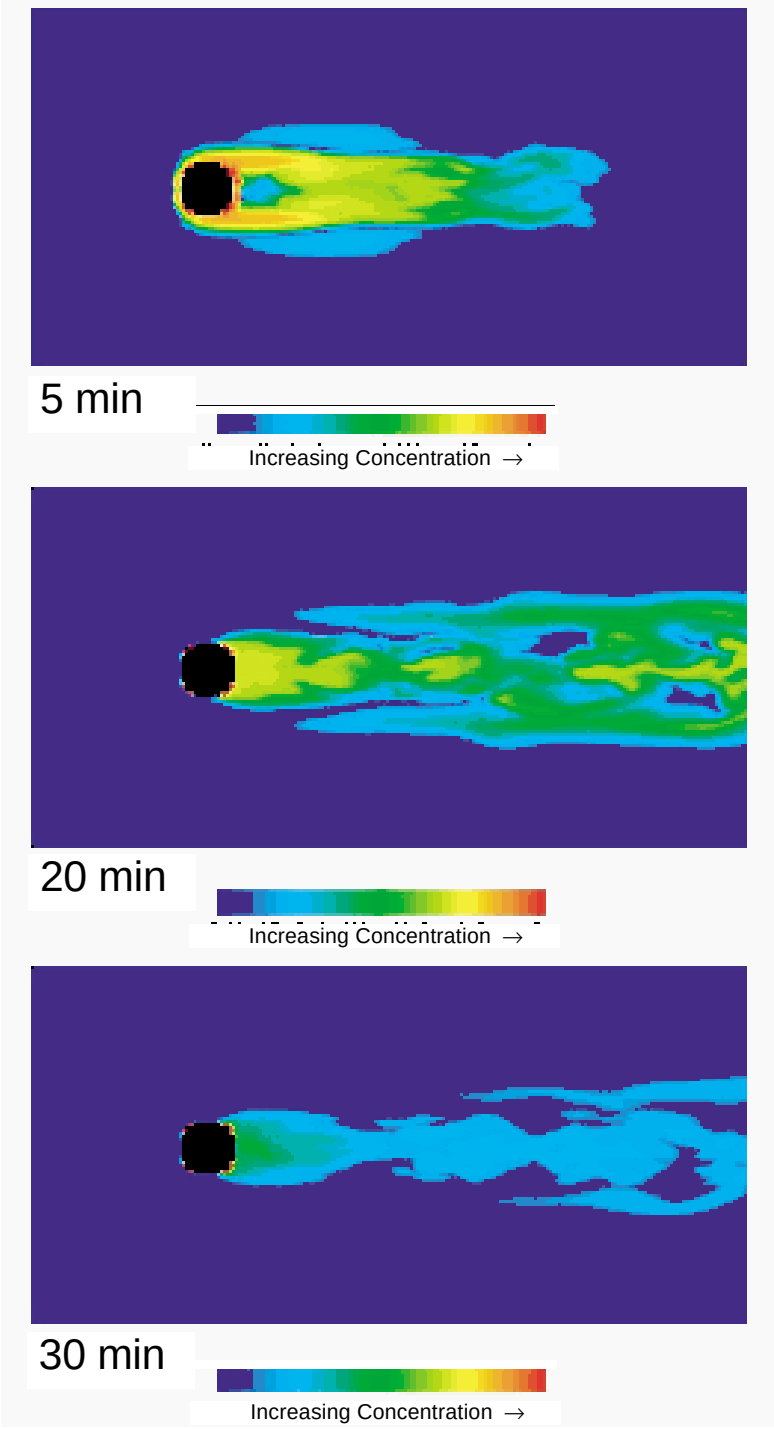

Figure 4. Near-Field Simulation of Building Flow.
The figure shows the transport and dispersion of pollutants downstream of a single building. Sources are located on all sides of the building, and some of the patterns here that appear unconnected to the wake are associated with transport over the building and back to the ground level.

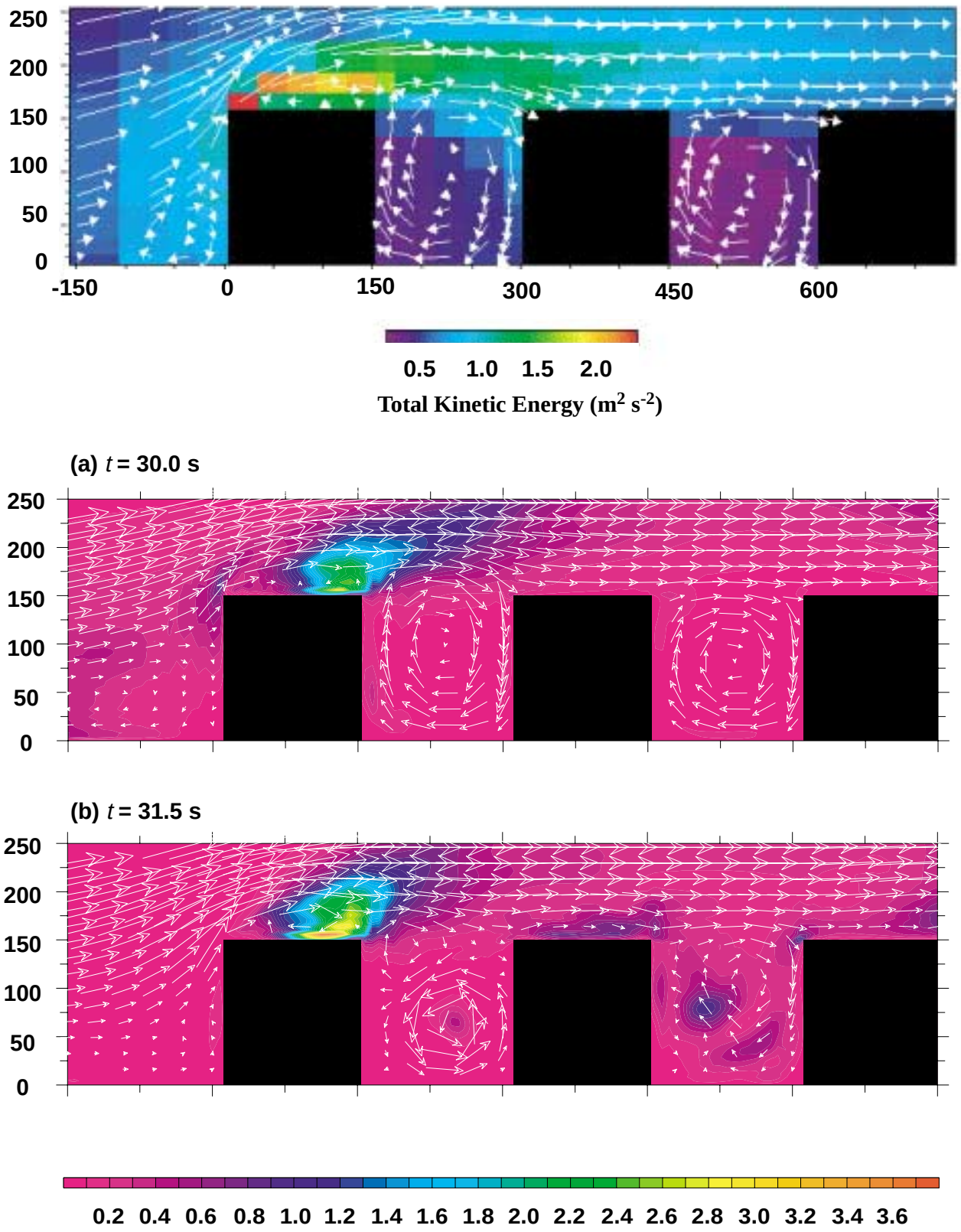

Figure 5. Wind Tunnel and HIGRAD Simulations of Flow Over Buildings.
The HIGRAD simulation shown here (bottom) reproduces the actual wind-tunnel geometry (top) using a downstream grid size of 1.5 cm. In addition to reproducing the overall flow pattern, HIGRAD captures such features as the structure of the turbulent kinetic energy and the flow recirculation upstream of the left-most building. (Wind-tunnel data courtesy of U.S. EPA.)

building array. High-resolution measurements of the three components of mean and turbulent velocity statistics were made with a pulsed wire anemometer at various heights within each "canyon" between the buildings, above each building, and upstream and downstream of the building array.

To simulate the wind-tunnel experiments, we used a domain size of 5.4 m in the along-flow direction and 1.4 m in the vertical direction with a $360 \times 1 \times 51$ grid. The downwind resolution was constant, and vertical grid varied from 0.05 H near the bottom of the domain to 0.1 H near the top. The inflow profile of the mean velocity for the simulations was determined from the wind-tunnel data, and HIGRAD simulations were integrated for a time span of 1 min with a time increment of 0.001 s.

Figure 5 shows a crosssection down the longitudinal centerline of the observed turbulent kinetic energy and mean wind vectors, which reveals the overall flow pattern. The figure shows a flow separation and corresponding recirculation over the first building rooftop. There is no similar recirculation over the other buildings. There are well-developed clockwise rotating vortices in each of the canyons. The turbulent kinetic energy peaks at the upwind edge of the first building and is largest above the canyons. Interestingly, the modeled turbulent kinetic energy is similar to that observed turbulent kinetic energy in pattern and magnitude despite the two-dimensional nature of the simulation.

The modeled flow field matches the wind-tunnel observations reasonably well. For example, a small recirculation zone upstream of the first building is simulated, as observed in the wind tunnel study. The model simulation also reproduces the flow separation and recirculation at the top of the first building. These features are not evident for the other buildings. Well-defined clockwise rotation in the canyons is also evident for the model simulation and wind-tunnel observations. These results have given us confidence to proceed in using the HIGRAD model as a tool to simulate urban dispersion effects for assessment and prediction purposes in real urban environments.

Conclusions

Simulating atmospheric phenomena involves addressing processes on a wide variety of spatial scales. The discussion here is concerned with micrometeorology simulations for which computational domains of 100 km^2 and less are appropriate. To simulate realistically processes associated with dispersion of contaminants and with combustion in wildfires, it is necessary to use computational techniques that can adapt to high gradients of both state variables and boundary conditions.

The LANL-developed model we call HIGRAD was designed specifically to include such gradients; in addition, it can be configured to compute the effects of the compressibility of air and the heating associated with absorption of sunlight and terrestrial radiation. This feature makes it suitable for simulating wildfires and dispersion of contaminants associated with heat sources (such as the NASA simulation discussed above) and with the complex lower boundary condition of the urban environment.

The model's versatility is highlighted in this discussion with results from simulations on domains from 1 to 10^8 m^2. Its application to the real-world problems of wildfire and of urban dispersion is continuing and provides a full-physics benchmark for simpler parametric models. ■

Further Reading

Hanson, H. P., M. M. Bradley, J. E. Bossert, R. R. Linn, and L. W. Younker. 2000. The potential and promise of physics-based wildfire simulation. *Environmental Science & Policy* **3:** 161–172.

Kao, C.-Y. J., Y.-H. Hang, D. I. Cooper, W. E. Eichinger, W. S. Smith, and J. M. Reisner. 2000. High-resolution modeling of LIDAR data mechanisms governing surface water vapor variability during SALSA. *Agricultural and Forest Meteorology* **105:** 185–194.

Reisner, J., S. Wynne, L. Margolin, and R. Linn. 2000. Coupled atmospheric-fire modeling employing the method of averages. *Monthly Weather Review* **128:** 3683–3691.

Reisner, J., V. Mousseau, and D. Knoll. 2001. Application of the Newton-Krylov method to geophysical flows. *Monthly Weather Review,* in press.

Smith, W. S., J. M. Reisner, and C.-Y. J. Kao. 2001. Simulations of flow around a cubical building: Comparison with towing-tank data and assessment of radiatively-induced thermal effects. *Atmospheric Environment,* in press.

Studying Water Vapor in the Atmospheric Surface Layer

D. I. Cooper (dcooper@lanl.gov), C.-Y. J. Kao, J. R. Reisner, and J. A. Archuleta (EES-8)

Interactions between the Earth's surface and its atmosphere play a fundamental role in a variety of processes of interest to EES Division. The exchange of water between plant communities and the atmosphere, in particular, is an important component of the climate system, and to a large degree, this exchange controls the local recycling of precipitation. In addition to the more traditional measuring techniques and modeling studies that are used in EES, we are using an advanced remote sensing system, a scanning Raman lidar, to understand the role of evapotranspiration, the process by which plants exchange water with the atmosphere.

Lidar, the optical equivalent of radar, is used in a variety of atmospheric science applications; the Los Alamos Raman system is designed to measure water-vapor concentrations at short-to-medium distances. This discussion of the Raman lidar's application to evapotranspiration over the San Pedro River riparian area in southern Arizona is an introduction to the instrument's capabilities.

Figure 1. The Los Alamos Raman Lidar.

Instrument Description

The Los Alamos Raman water-vapor lidar is based on the Raman technique pioneered in the 1960s and extended for daytime, solar-blind operation in the 1980s. In Figure 1 we see a photograph of the Los Alamos Raman lidar being set up for operation in Arizona. The device operates by emitting a pulsed, ultraviolet laser beam. The laser light is absorbed by nitrogen and water vapor molecules and re-emitted in their Raman bands. The lidar system then collects this "Raman-scattered" light and converts it to an electrical signal. The system operates in the solar-blind region of the spectrum using krypton fluoride as the lazing medium to obtain light at 248 nm. The Raman-shifted nitrogen signal returns at 263 nm, and the Raman-shifted water vapor signal returns at 273 nm. Simultaneous measurement of the water-vapor and nitrogen signal returns provides a simple method for obtaining absolute measurements.

Because nitrogen is by far the most abundant atmospheric gas and because its concentration is relatively invariant, dividing the Raman-shifted return signal from water vapor by that of nitrogen normalizes each pulse and corrects for first-order atmospheric transmission effects, pulse-to-pulse laser variations, and telescope field-of-view overlap with the laser beam. The normalized returns are then proportional to the absolute water-vapor content of the air. A correction is required to account for the differential atmospheric attenuation between the nitrogen and water-vapor wavelengths.

The typical maximum horizontal range for the lidar is approximately 700 m when scanning, with a corresponding spatial resolution of 1.5 m over that distance. The upper scanning mirror allows three-dimensional scanning in 360° in azimuth and ±22° in elevation. The uncertainty in the water-vapor mixing ratio is typically measured to be less than 4%.

Spatial Variations of Water Vapor

Here we present selected lidar-data analyses as vertical lidar scans of water-vapor concentration (in the form of mixing ratio) and as vertical profiles of water vapor derived from

the scans. The vertical scans represent vertical/horizontal cross-sections of the structure of atmospheric water vapor. Our analysis focuses on measurements over a cottonwood canopy versus measurements over the adjacent grass-shrub cover.

Water Vapor over a Canopy. In 1997, the Los Alamos Raman lidar system was fielded as a part of the Semi-Arid Land-Surface Atmosphere Experiment (SALSA) for the San Pedro Project in Arizona. The site chosen for this field study included both grassland/scrub areas and the cottonwood-bosque riparian area adjacent to the San Pedro River.

A cursory inspection of some of the lidar data obtained reveals interesting properties of the cottonwood-canopy/surface-layer interface, when compared with the atmosphere above the relatively flat grass-mesquite-sacaton region adjacent to the San Pedro riparian corridor. An example of a time series of vertical scans acquired between 0913 local standard time (LST) and 1436 LST on August 11, 1997, illustrates the spatial patterns and distribution of water vapor mixing ratio in 1.5-m, range-resolved pixels. The variations in color in the images of Figure 2 show high mixing-ratio values in red and low values in blue. The vertical scans are composed of 42 individual scan lines in which each scan required 0.75 s. Thus, it took about 32 s to complete and save each image. The lidar return signal from the cottonwood trees was substantially larger than the atmospheric signal and saturated the detectors; therefore, the returned signal from the leaves, stems, and trunks can be separated from the atmospheric signal by using a simple threshold. By setting all mixing-ratio values above 16.8 g/kg^{-1} as canopy signal and all values below 16.8 g/kg^{-1} as "atmospheric" signal, the canopy appears as solid red in the Figure 2 images.

The black regions on the images are areas for which the water vapor mixing ratio is below 10.5 g/kg^{-1}, the reading associated with the bottom-most color on the legend. When the return signal is less than 14.0 g/kg^{-1}, patterns emerge from the data, as can be seen in the unstable regions above the surface and the canopy.

Microscale convective structures above the canopy are seen as "bubbles" of high-mixing-ratio air presumably interacting with the relatively drier air from above, such as the structure at 430 m range and starting at 30 m height in the 0913 LST scan. At the time of this measurement, the wind was nearly perpendicular to the lidar line of sight. Over a green ash orchard, the lidar observed similar convective structures that were closely related to intermittent features, including "ramps." The high-mixing-ratio features over the mesquite-sacaton area are 2 to 3 g/kg^{-1} drier than those over the cottonwood canopy. Interestingly, these features appear primarily in the morning and decrease in frequency until they disappear at midday; after about 1330 hours LST, they begin reappearing. We still do not know if these structures are due to dynamics above the canopy or to canopy-atmosphere interactions such as sweep-ejection phenomena.

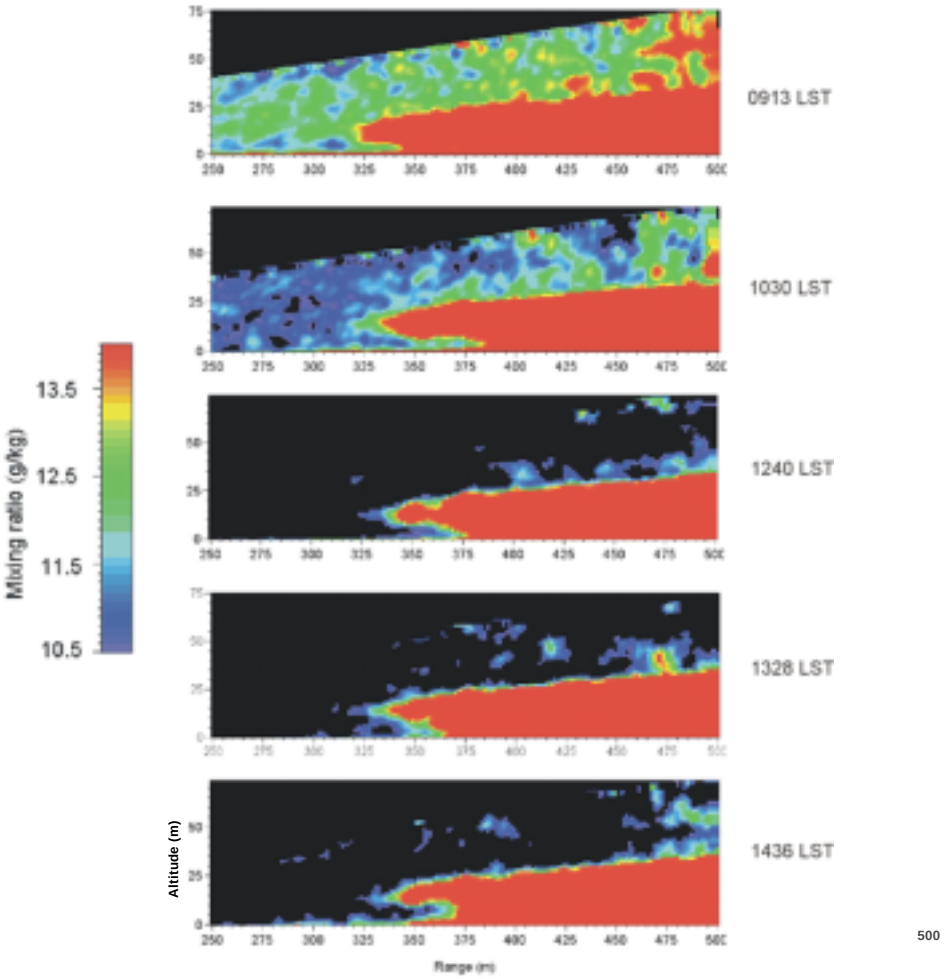

Figure 2. Lidar Scans over Cottonwoods and Grassland.
These scans show vertical cross sections of water vapor above the San Pedro River cottonwood bosque for a series of times indicated as local standard time (LST).

A more traditional method for displaying and analyzing the lidar data would be in the form of vertical profiles of water vapor extracted from the scans. We made one-dimensional profiles with 32-s averaging times by sorting the range pixels by their associated height bins from an individual scan shown in the Figure 2 cross sections. Thus, all range pixels from a given region that fell into a specified height range (e.g., from 0 to 0.5 m in elevation) can be displayed as mixing ratio versus height. We extracted two 25-m-wide sections from the 0913 LST scan in Figure 2 at positions over both the grass-mesquite-sacaton association (at ranges between 300 and 325 m) and the cottonwoods (between 425 and 450 m). The grass was in the near field of the scan, limiting the height of the profile to 35 m. The sixteen 1.5-m lidar values per height bin in these 25-m scan widths provide the data points of the profiles in Figure 3. Although the average mixing ratio is similar for the two regimes, there is a substantially larger variability at a given height over the cottonwoods. Both regimes exhibited an undulating structure with height, reflecting some of the coherent structures visible in the image in Figure 2. Figure 3 suggests that over both regimes the size of these structures is similar, approximately 20 m. The plumes observed in Figure 2 create the moistening observed 10 to 15 m above the canopy in the profiles of Figure 3; as these plumes decay in height, the profiles show these higher regions as "dry."

The most pronounced difference between the two profiles in Figure 3 is the variability of function of height above the canopy. While the mean mixing ratios for the grass and cottonwoods are only about 0.5 g/kg^{-1} apart, the range of values at a given height is approximately 2.5 times greater for the cottonwoods than for the grass. This difference shows that water vapor from the cottonwood provides greater atmospheric input than does water vapor from the grassland.

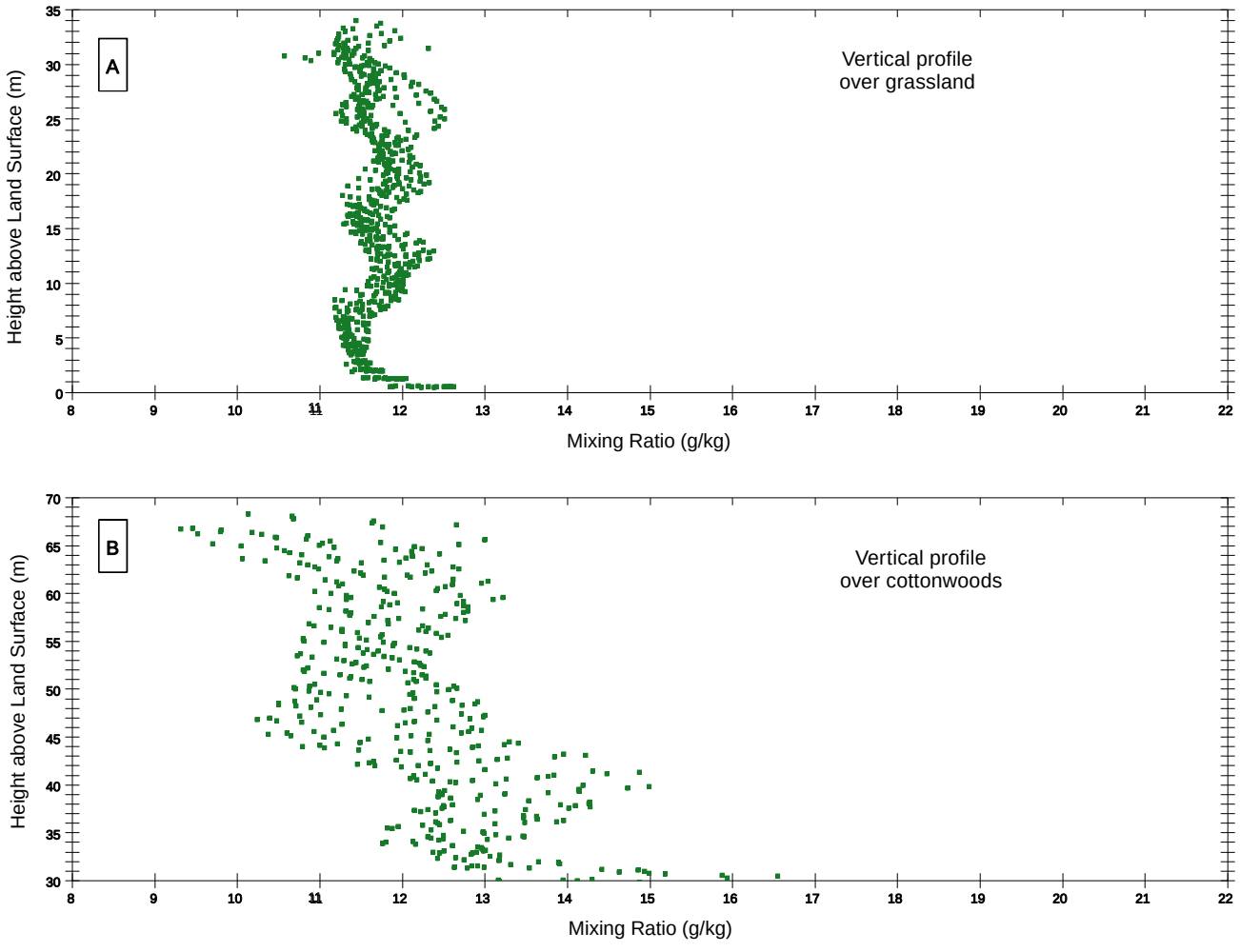

Figure 3. One-Dimensional Water-Vapor Profiles.
These vertical profiles from Figure 2 are of (A) water-vapor mixing ratio over grassland between the surface and to a height of about 35 m from the leftmost part of the Figure 2 images and (B) the ratio over cottonwoods between the tree tops and about 70 m.

Closing Comments

Understanding mixing processes in the atmospheric boundary layer and how they are influenced by—and influence—surface/atmosphere exchange processes is critical to understanding the Earth's hydrological and carbon cycles and the climate itself. Although numerical models provide great insight into these mixing processes, direct observations add a new dimension to our studies. The Los Alamos Raman lidar system can directly measure small-scale variations in atmospheric water vapor. Those variations are closely tied to the mechanisms of atmospheric mixing.

As shown by the example presented here, water vapor in the lower atmosphere is influenced strongly by the character of the Earth's surface itself, in this case by the differences between cottonwood canopies and grasslands. The greater evapotranspiration rates from the canopy in the SALSA experiment are reflected by higher water-vapor mixing ratios above the canopy. In addition, the scales of the mixing processes are shown by the sizes of the bubbles of high-mixing-ratio air and by the bubbles' progression in time.

We are conducting additional field studies using the Raman system. For example, we are participating in the DOE-funded vertical transport and mixing experiment, in which nocturnal mixing processes in the atmosphere above Salt Lake City are being studied. We are also conducting a variety of observational campaigns to promote understanding of evapotranspiration processes from various types of ground cover. These sets of measurements will address questions about the efficiency of water retention of various biomes, the differences between daytime and nighttime mixing processes (and the behavior of the transition between the two regimes), and the effects of these mixing processes on the transport and fate of atmospheric pollution. ■

Further Reading

Cooper, D. I., W. E. Eichinger, D. E. Hof, D. Seville-Jones, R. C. Quick, and J. Tiee. 1994. Observations of coherent structures from a scanning LIDAR over an irrigated orchard. *Agricultural and Forest Meteorology* **67**: 239–252.

Cooper, D. I., W. E. Eichinger, J. Kao, L. Hipps, J. Reisner, S. Smith, S. M. Schaeffer, and D. G. Williams. 2000. Spatial and temporal properties of water vapor and latent energy flux over a riparian canopy. *Agricultural and Forest Meteorology* **105**: 161–183.

Cooney, J., K. Petrik, and A. Salik. 1985. Measurement of high-resolution atmospheric water vapor profiles by use of a solar-blind, raman LIDAR. *Applied Optics* **24**: 104–108.

Eichinger, W., et al. 1992. Derivation of water vapor fluxes from LIDAR measurements. *Boundary-Layer Meteorology* **63**: 39.

Kao, C.-Y. J., Y. H. Hang, D. I. Cooper, W. E. Eichinger, W. S. Smith, and J. M. Reisner. 2000. High-resolution modeling of LIDAR data: Mechanisms governing surface water vapor variability during SALSA. *Agricultural and Forest Meteorology* **105**: 185–194.

Melfi, S. H., et al. 1969. Observation of raman scattering by water vapor in the atmosphere. *Applied Physics Letters* **15**: 295.

Hydrogeochemistry of Contaminated Springs at TA-16

B. Newman (EES-10, bnewman@lanl.gov), D. Hickmott (EES-6), E. Ludwig (EES-10), and S. McMillan (EES-6)

Deep drilling at Technical Area (TA) 16 at LANL recently revealed high explosives (HE) contamination at depths from 750 to 1500 ft, including in the regional aquifer. The levels of HE are over 40 times the Environmental Protection Agency lifetime health advisory for the HE RDX (cyclotrimethylenetrinitramine). This discovery has heightened concerns among members of the public, neighboring Indian pueblos, and other stakeholders about groundwater contamination from Laboratory operations. In addition to HE, barium and nitrate contamination are also of concern at TA-16. We are determining the extent of contamination and investigating the processes that control contaminant concentrations in the TA-16 mesa and canyon environments.

Based on extensive interviews with site personnel and widespread environmental sampling, we determined that the most significant source of HE contamination appears to be outfall from the HE-machining building, TA-16-260 (Figure 1). Total HE levels in soil at this site range to over 20 weight percent (wt%). To reduce the concentrations of HE available for transport, the contaminated soils have been excavated and staged for off-site disposal.

Because water is the most likely medium by which the HE constituents may affect human or ecological receptors, the crucial scientific question associated with the environmental investigations at TA-16

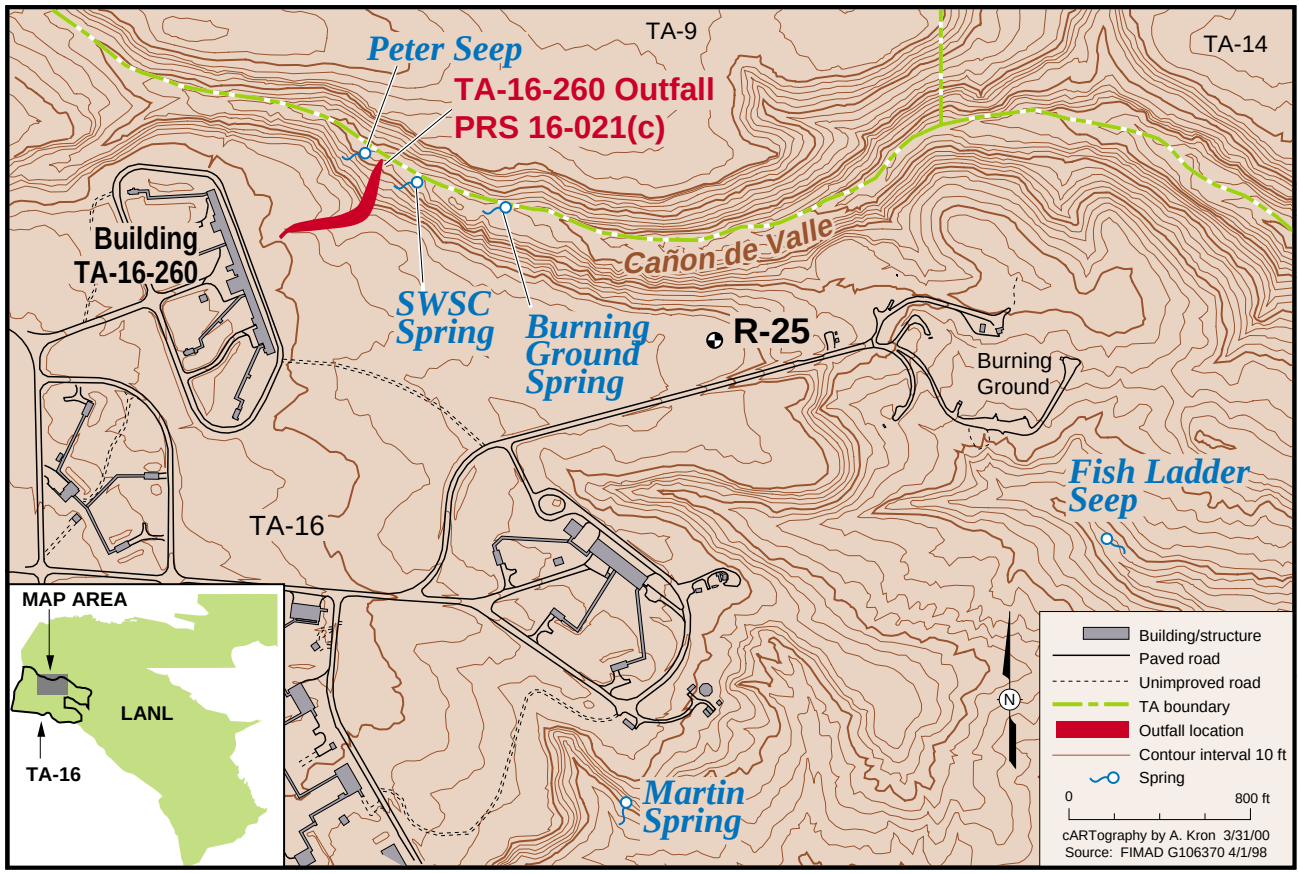

Figure 1. Technical Area 16.
Map showing the location of the TA-16-260 outfall and nearby features. Inset shows the location of TA-16 at LANL.

concerns how water and its associated contaminants move through the hydrogeologic system in this area. We have addressed this question in our study.

A conceptual model of likely fluid flow paths at TA-16 is shown in Figure 2. Water in three springs (sanitary wastewater system consolidation [SWSC], Burning Ground, and Martin), the Cañon de Valle alluvial system, and deeper groundwater in well R-25 is contaminated with HE.

At this time, we are focusing on understanding the shallow (less than 200-ft depth) hydrologic system as it manifests itself in the springs and seeps located in Cañon de Valle and Martin Canyon. We are using measurements of spring water chemistry, spring flow rates, and stable isotope compositions to determine (1) the principal recharge locations for the TA-16 springs (and by inference the recharge locations for the deeper hydrologic systems), (2) the nature of temporal variability in both natural and anthropogenic constituents in springs, and (3) whether contaminant concentrations are decreasing or increasing with the passage of time.

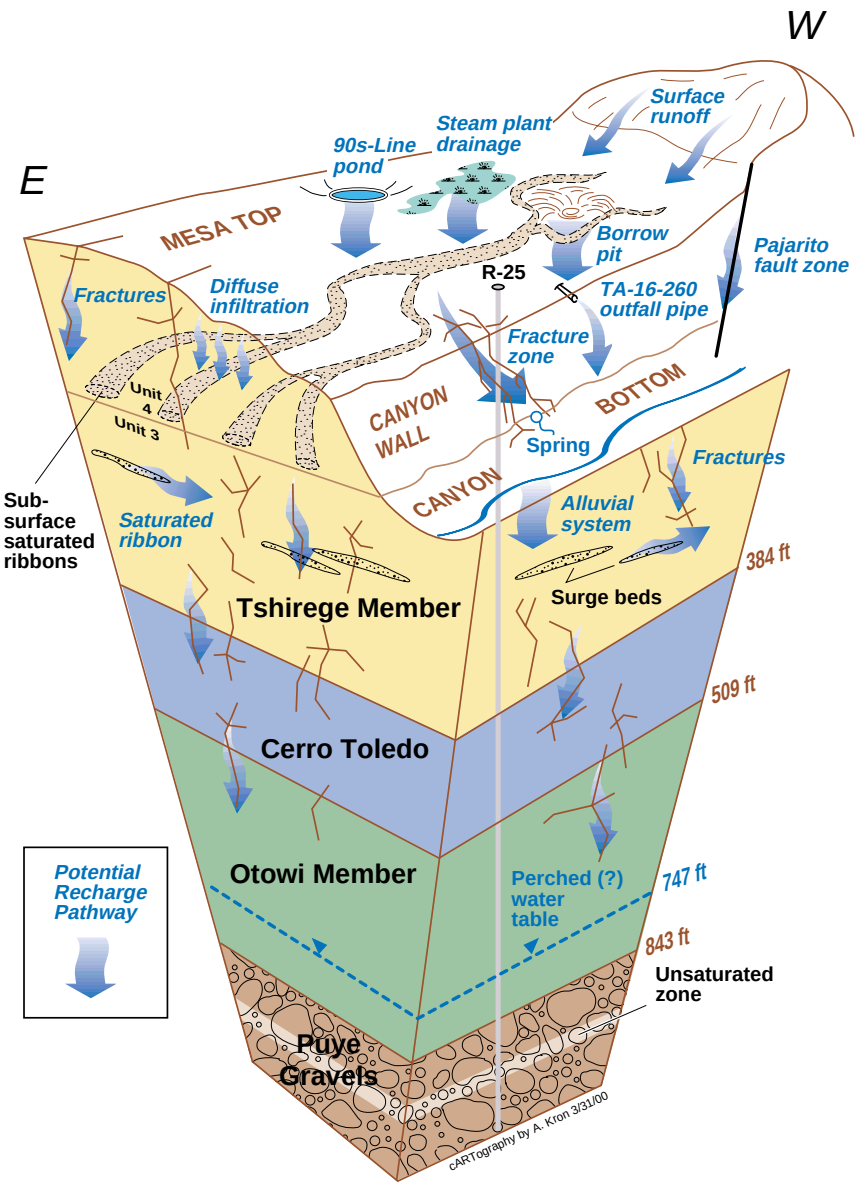

Figure 2. Water Transport.
Diagram showing a conceptual model for water transport at TA-16 (and by inference, associated HE and barium contamination).

Water Chemistry and Flow Rates

Data on spring flow rates and water chemistry provide information on the hydrologic systems and pathways that feed the springs. The water chemistry of a spring reflects local precipitation and interactions with soils and rocks along the flow paths that feed the spring. A spring system that shows little change in flow or chemistry over time is typically interpreted to represent a well-mixed system with little seasonal variation in recharge sources. A more dynamic spring system reflects differing proportions of water sources such as diffuse recharge, spring snowmelt, monsoonal water, and anthropogenic discharge.

Our observations suggest that the water chemistry of the TA-16 springs is typical of springs in the arid and semiarid Southwest, particularly those associated with evolved volcanic rocks such as those found in the Jemez Mountains. All the springs at TA-16 are low-ionic-strength calcium-bicarbonate, mainly because of the high pH in local soil, widespread occurrence of carbonate, and preponderance of Ca-K rich volcanic rocks and soils.

Temporal Variations. Both flow rates (Figure 3) and concentrations (Figure 4) of naturally occurring and anthropogenic compounds in the TA-16 springs vary with the seasons and with high-precipitation events. Not surprisingly, flows are highest following spring snowmelt and the summer monsoonal rains. Burning Ground Spring has the highest annual

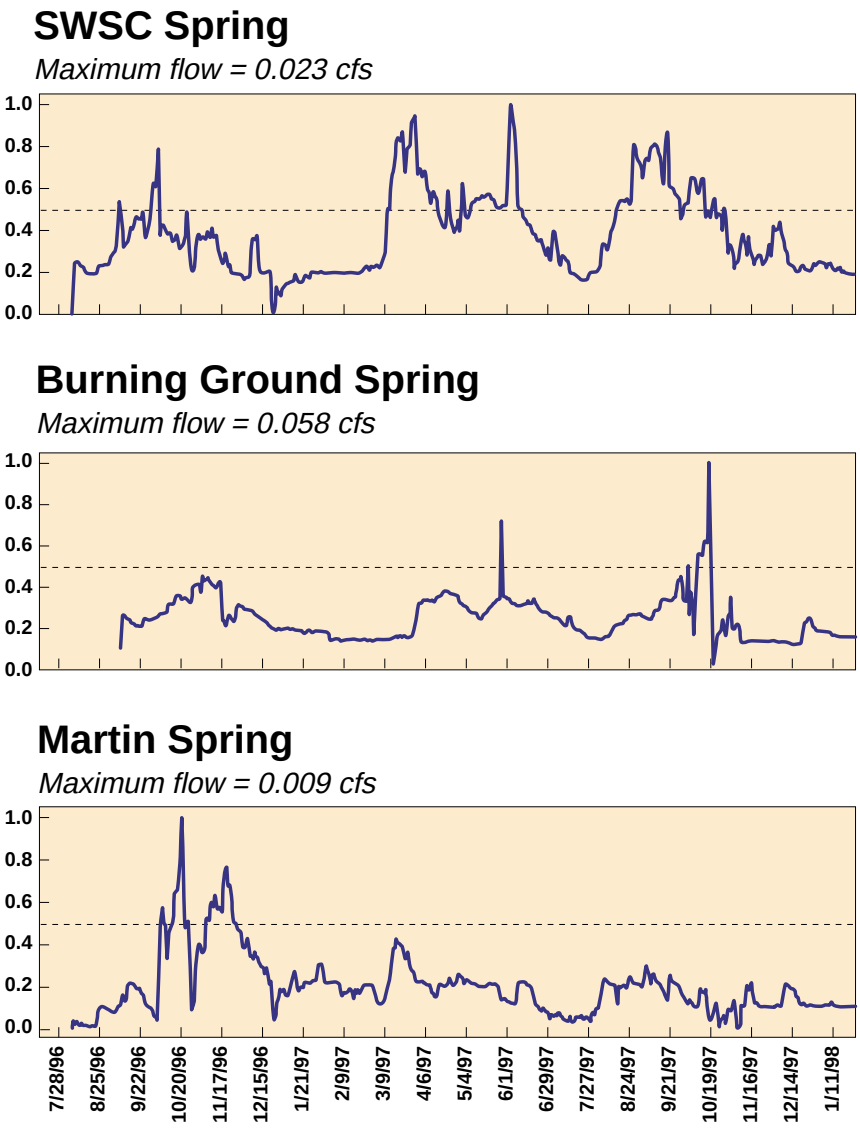

Figure 3. Water Flow.
Flow rates in cubic feet per second (cfs) at SWSC, Burning Ground, and Martin Springs between 1997 and 1999.

flow of the three; however, our analysis of the frequency distribution of average daily flow at Burning Ground indicates that it has a narrow range of flow rates, and the normalized standard deviation of flow rates is the lowest of the three. In contrast, the SWSC Spring and the highest normalized standard deviation of flow rates. Our data indicate that SWSC Spring has a more variable flow behavior than Burning Ground Spring. Martin Spring has the lowest flow rates of the three. Our data for Martin Spring show a continuous range of flow rates and an intermediate normalized standard deviation.

The flow variations (or more specifically, changes in recharge that cause flow of water to vary) affect the chemistry of the spring waters as well. The water chemistry varies with the extent of dilution during high-flow periods and the pathways taken by recharge. This variation takes place because different parts of the vadose zone are sampled as saturated zones grow and shrink during recharge (Figures 3 and 4). For example, recharge can increase dissolved oxygen in the spring waters, thus altering redox conditions. The variability of the redox conditions is likely responsible for some of the observed concentration variations in redox-sensitive species such as iron, and it also has implications for the breakdown of nitrate and HE.

Spring-Water Chemistry Comparisons. To examine the overall chemical behavior of the springs and evaluate differences between them, we developed correlation matrices for 39 chemical parameters (including pH and temperature). Our results show generally similar correlations of chemical parameters between the springs, although there are some important differences in actual concentrations of the chemical parameters between the springs. The correlations between the major anions and HE species are statistically significant, which is evidence that the HE species are behaving conservatively (i.e., they are highly mobile). All the springs have elevated nitrate concentrations, and nitrate correlates significantly with HE and barium, the two main anthropogenic sources of nitrate at TA-16. Barium concentrations are also elevated, and barium is correlated with the other major cations.

Burning Ground and SWSC Springs have relatively small differences in chemistry, which reflects their close proximity and implies that they are part of the same flow system. As noted above, there are some differences in their flow behavior that reflect different degrees of connectivity to the saturated zone and the different fast recharge pathways from which the two springs receive water. There are significant differences between the chemistry of Martin Spring versus Burning Ground and SWSC Springs. Martin Spring has greater boron, HE, nitrate, and sulfate concentrations (as well as other chemical constituents) than both Burning Ground and SWSC Springs. In addition, Martin Spring has higher

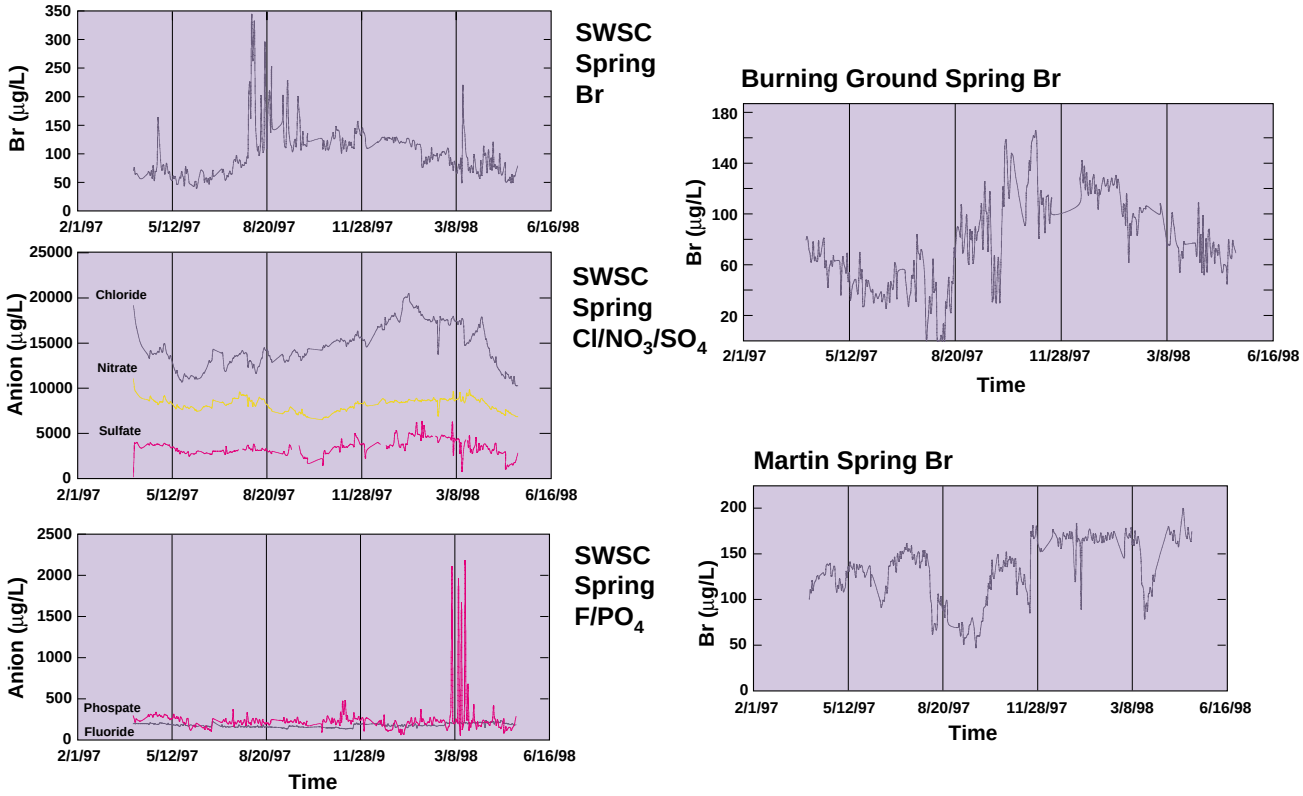

Figure 4. Bromide and Other Anion Concentrations.
The plots show constituent concentration (unfiltered data) versus time for the three springs.

stable isotope ($\delta^{18}O$ and δD) values than the other springs. The different flow behavior and chemistry in Martin Spring suggests that Martin may be part of a different flow system than SWSC and Burning Ground Springs or that it has an additional recharge source that is large enough to shift the spring chemistry away from that of the other springs.

Barium Colloids. A systematic bias occurs in barium concentrations for all three springs, where unfiltered barium concentrations are higher than filtered (0.45-mm filtration). This bias suggests that some of the barium inventory is being transported as either barite colloids or as sorbed barium on other colloidal minerals. Our geochemical modeling results using the code PHREEQC (Parkhurst 1995) suggest that barite ($BaSO_4$) colloids may be precipitating in the spring waters. The geochemical modeling results and filtered versus unfiltered analyses also suggest that iron and/or alumino-silcate mineral colloids may be precipitating in the springs. These minerals may act as a substrate for barium adsorption.

Tracer Study Results. We applied a potassium bromide tracer in the TA-16-260 outfall (Figure 1) during April 1997 and observed bromide breakthrough in SWSC Spring during August 1997 (Figure 4). This observation confirms the connection of the contaminated soils in the TA-16-260 outfall and the contamination in the springs.

The bromide tracer results suggest that fluid flow and contaminant transport are influenced by fractures. The nature of the bromide breakthrough suggests fluid flow through a porous media with a bimodal permeability distribution. The intermittent nature of the bromide peaks suggests a heterogeneous system and may reflect hydrologic dispersive effects. The rapid breakthrough (less than 6 months) is incompatible with flow through a homogeneous porous media with unsaturated hydraulic conductivities similar to those measured in the Bandelier tuff at TA-16 and suggests that fracture flow is an important recharge process.

Stable Isotopes and Tritium. Hydrogen (including tritium) and oxygen isotopes are excellent tracers of hydrologic processes. Hydrogen and oxygen stable isotope ratios and tritium activities can be measured accurately using modern spectrometric techniques. In low-temperature environments, the isotope ratios of hydrogen and oxygen are not strongly influenced by interactions with soil or rock matrix. Hence, stable-isotope ratios are extremely sensitive indicators of recharge source and of fluid-mixing processes. Stable isotope data are typically

expressed in delta (δ) notation in permil (‰) units.

Our measurements of oxygen stable isotope compositions in local precipitation show both seasonal and shorter-term variations. Summer monsoonal storms generally have higher $\delta^{18}O$ values than winter storms or snow. In addition, $\delta^{18}O$ can vary significantly (by up to 10‰) between individual precipitation events. This variability reflects the multiple precipitation sources that affect the Jemez Mountain region.

In contrast, the oxygen isotope compositions of the three springs vary less than local precipitation. SWSC and Burning Ground Springs vary by at most 3‰ in $\delta^{18}O$ and Martin Spring varies by at most 5‰. This damping of the oxygen isotopic signature reflects the mixing and dispersion that occur between recharge and discharge in the springs. However, most well-mixed springs show even less annual variability in $\delta^{18}O$, suggesting that the time frame of flow for the springs is short (less than a few years). Our preliminary mixing model calculations suggest that a large proportion (>30%) of the increased flow in response to some precipitation events is new water. In other words, significant amounts of water recharge the spring systems and are discharged within 24 hours of a given precipitation event. These data reinforce the concept of fast pathways and suggest that spring residence times are relatively short. Work is currently underway to examine the spring residence times more thoroughly.

The stable oxygen isotopic data also show strong similarities between the SWSC and Burning Ground Springs and suggest that Martin Spring has different recharge sources. As well as having a damped annual signal relative to Martin Spring, SWSC and Burning Ground Springs also are consistently lower in $\delta^{18}O$ than Martin Spring. A particularly important feature of the hydrogen and oxygen isotope compositions of precipitation is that they vary linearly with elevation. Higher-elevation precipitation has lower average isotopic values than lower-elevation precipitation. Because of this linear relation with elevation, spring stable-isotope compositions can be used to estimate recharge elevations. Using a simple (non-mass flux weighted) average, these data suggest that the recharge zone for the mass of water seen at Martin Spring may be about 900 ft lower in elevation than that for the other two springs. It is also possible that Martin Spring has received recharge from an evaporated source such as ponds on the mesa top. This type of input will result in an estimated recharge elevation that is too low. In any case, the difference in stable isotopes between Martin and SWSC/Burning Ground Springs is consistent with the major ion and contaminant data discussed above and supports a difference in recharge sources.

Tritium (^3H) can be used to trace young groundwater signatures because it has a short half-life (12.4 yr) and because it was produced during atmospheric nuclear testing during the 1950s and 1960s. All three springs contain elevated tritium (29–43 tritium units), suggesting young recharge sources. Assuming a piston-flow regime (Blake et al., 1995), the tritium model ages are less than 30 yr. However, this is a maximum age estimate, and ages are likely to be less than 5 yr.

Conclusions

Stable isotope, tracer, and water chemical data all suggest that the TA-16 springs are fed by complex hydrologic systems that tap a base-flow component, a young-recharge component, and a contaminated, anthropogenic component. Recharge for all three springs appears to be local, and the residence times for this precipitation in the hydrologic system discharged at the springs is probably short (less than a few years). SWSC and Burning Ground Springs have similar isotopic signatures, chemistries, and flow characteristics. Martin Spring appears to be distinct.

This hydrologic information is significant for the ongoing studies of HE contamination at TA-16 for three reasons. First, the short residence times for spring discharge suggest that the spring HE concentrations will decrease following removal of the principal HE sources on the TA-16 mesa top. Second, the contaminant flux information that is being derived in these studies will be vital to support both human health and ecological risk assessments for the site. Finally, the studies provide fundamental hydrologic information on the flow and transport of water in a semiarid, fractured hydrologic system. Fractured systems are among the most difficult to develop adequate conceptual models and, hence, simulate numerically. The empirical data collected in these studies will represent an excellent test of complex hydrologic codes used to simulate vadose zone flow in fractured systems. ■

Further Reading

Blake, W. D., F. Goff, A. I. Adams, and D. Counce. 1995. Environmental geochemistry for surface and subsurface waters in the Pajarito Plateau and outlying areas, New Mexico. Los Alamos National Laboratory report LA-12912-MS.

Chapman, J. B., N. L. Ingraham, and J. W. Hess. 1992. Isotopic investigation of infiltration and unsaturated zone flow processes at Carlsbad Cavern, New Mexico. *Journal of Hydrology* **133**: 343–363.

Clark, I., and P. Fritz. 1997. *Environmental Isotopes in Hydrogeology*. New York, NY: Lewis Publishers, 328 pp.

Groffman, A. R., and L. J. Crossey. 1999. Transient redox regimes in a shallow alluvial aquifer. *Chemical Geology* **161**: 415–442.

Hoefs, J. 1987. *Stable Isotope Geochemisty*. New York, NY: Springer-Verlag, 236 pp.

Moreno, L., and C. F. Tsang. 1994. Flow channeling in strongly heterogeneous porous media: A numerical study. *Water Resources Research* **30**: 1421–1430.

Parkhurst, D. L. 1995. User's guide to PHREEQC—A computer program for speciation, reaction path, advective-transport, and inverse geochemical calculations. USGS Water-resources investigation report 95-4227.

Rose, T. P., M. L. Davisson, and R. E. Criss. 1996. Isotope hydrology of voluminous cold springs in fractured rock from an active volcanic region, northeastern California. *Journal of Hydrology* **179**: 207–236.

Rozanski, K., L. Araguas-Araguas, and R. Gonfiantini. 1993. Isotopic patterns in modern global precipitation. In *Continental Isotope Indicators of Climate*. American Geophysical Union Monograph.

Shuster, E. T., and W. B. White. 1971. Seasonal flucuations in the chemistry of limestone springs: A possible means for characterizing carbonate aquifers. *Journal of Hydrology* **14**: 93–128.

Vuataz, F.-D., and F. Goff. 1986. Isotope geochemistry of thermal and nonthermal waters in the Valles Caldera, Jemez Mountains, northern New Mexico. *Journal of Geophysical Research* **91**(B2): 1835–1853.

Implications of the Shagan River Hole-Closure Shots for Nuclear Explosion Monitoring

W. S. Phillips (wsp@lanl.gov), D. C. Pearson, H. E. Hartse, S. R. Taylor, and L. K. Steck (EES-11)

In 1992, the United States and the former Soviet Union stopped underground nuclear testing and began the process of closing down their test sites. To ensure that boreholes and tunnels that had been dug at the Kazakhstan Shagan River Test Site would never be used, a series of chemical explosions to collapse and seal off the holes was conducted in 1997 and 1998. This event presented a unique opportunity for international collaboration on experiments to obtain information on the geology of the region, how that geology affects the transmission of seismic signals, how to locate the source of an explosion of interest with the utmost possible precision, and calibration of seismic monitoring stations. We were part of an international team that designed and carried out these experiments. In this paper, we will discuss our analysis and interpretation of the data we collected.

Background

The Comprehensive Test Ban Treaty (CTBT), which was opened for signature in 1996, tackles the issue of verification, a long-standing barrier to the cessation of nuclear testing, by creating an international monitoring and verification regime termed the International Monitoring System (IMS).

The IMS is composed of four sets of monitoring stations. Each day, these stations transmit enormous amounts of data via satellite to the International Data Centre in Vienna, Austria, which, in turn, distributes it to national data centers around the world.

Computers at the International Data Centre will process the raw data, associate segments of the data stream with specific events, and estimate the location of those events. Analysts will then review the processed data. National data centers will have the responsibility for making judgments about the true nature of a suspected event (was it a man-made but non-nuclear event, a natural occurrence such as an earthquake, or a nuclear explosion?).

If a particular event is determined to have a high probability of being nuclear, provisions in the treaty for an on-site inspection may come into play. The treaty requires location of the event to within 1,000 km^2 before an on-site inspection can be contemplated. However, it is easy to imagine situations for which much higher location accuracies might be called for, such as correlating suspected locations with additional information or determining where to drill within the area of an on-site inspection.

Although the U.S. Senate did not ratify the CTBT in 1999, it is possible that its initial concerns may be satisfied as the IMS matures. Whether the treaty enters into force or not, the U.S. will have a strong national security interest in monitoring, verifying, and locating nuclear explosions.

Because any group or nation that conducts a nuclear test now is likely to be condemned, there is strong incentive to avoid detection. As the IMS build-up continues, avoiding detection will mean conducting tests of devices with very small yield and using other technical means, such as decoupling some of the seismic energy from the Earth by excavating around the device being tested, to disguise the test.

For treaties previous to the CTBT, monitoring at great (teleseismic or greater than 2,000 km) distances was adequate to record the events allowed by the treaties. The CTBT, however, allows *no* events, so monitoring at regional (less than 2,000 km) distances to detect very small magnitude events is required.

Regional monitoring is more difficult than teleseismic because the seismic energy that reaches the sensors at the monitoring station will have traveled not through the Earth's core but through its crust, which has widely varying properties from region to region throughout the world.

For all these reasons, monitoring under a CTBT regime is dauntingly difficult. Data from experiments we conducted at the Shagan River Test Site (the Russian name is the Balapan Test Site) will improve understanding of the seismology of the region and its effect on the seismic signals. This information can also lead to improved location capability of the IMS and to calibrating the IMS seismic stations located near the former test sites.

Experimental Methodology

During 1997 and 1998, twelve chemical explosions were detonated by the U.S. in boreholes at the former Soviet nuclear test site at Shagan River in Kazakhstan. The depths of these explosions ranged from 2.5 to 550 m, and the explosive yield varied from 2 to 25 tons. Each explosion was recorded at local distances by a

network of seismometers operated by Los Alamos and the Institute of Geophysics for the Kazakhstan National Nuclear Centre. In 1997, a 50-m shot occurred in sedimentary rock; the others occurred in crystalline rock. Ground-truth location, time of origin, and other shot data may be found in Phillips et al. (2000).

We chose to restrict our study to IMS station data because, in the future, these data will be available on the most timely basis. In addition, it is important to test the ability of this sparse network to perform high-precision location.

The IMS stations used in this study are distributed unevenly, with four along northerly azimuths from the test site and only one along a southerly azimuth (Figure 1). Large azimuthal gaps exist in the east and southwest directions. The gaps are made larger by the virtual exclusion of data from the station at Zalesovo (ZAL) because of clock error. Station X02, at 86 km, is very close for verification monitoring; however, repeatable waveforms were also observed at arrays out to 6,689 km. Signals detected at the select set of teleseismic distance stations may result from favorable noise conditions, as well as focusing in the upper mantle beneath the source or receiver sites.

Seismic data were recorded by stations that reported to the prototype International Data Centre, as well as by stations deployed at the future IMS. Our approach was to use ground-truth information from one event to obtain relative locations of others in a blind manner, using IMS and surrogate stations and a standard earth model. The ground-truth information allows independent verification of results and calibration of data error, as well as assistance in evaluation of sources of error in the relative location procedure.

Seismograms were recorded on L4-C-3D, three-component, velocity sensors connected to Refraction Technology data loggers. Origin times for each event were obtained by a GPS-based timing system employed at each hole for shot-break time. The origin times were checked for consistency using an accelerometer and data-acquisition system placed near the test borehole.

Seven sites were selected at various azimuths to the proposed locations for the depth-of-burial experiment. For the 1998 series of hole closures, the seismic stations reoccupied the same depth-of-burial locales, except for S3, which was relocated because of technical

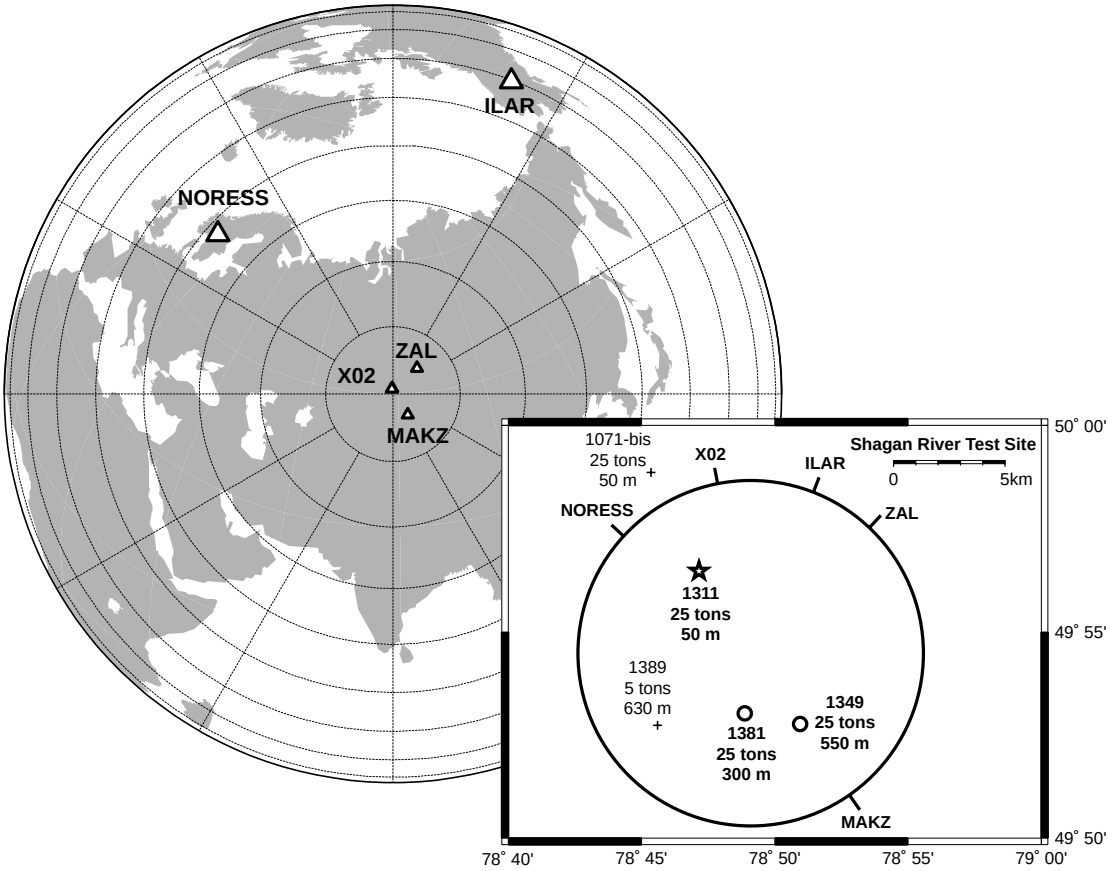

Figure 1. Shagan River Test Site Shots and IMS Stations Used in the Relative Location Test.
The master-event shot is designated by a star, relocated shots by open circles, and other shots mentioned in the text by crosses. Hole number, shot yield, and depth are also indicated. Azimuths to IMS stations are shown around the encompassing circle. The background map is an orthographic projection centered on the Shagan River, with triangles indicating station locations. Concentric grid lines represent distance from the site in 10° intervals, and radial grid lines represent azimuth from the site in 30° intervals.

problems. For the L4-C-3D sites, the data were sampled at 500 Hz, and the recorder was set up to use a trigger based on the ratio of the short-term to the long-term average value of the data. The data were then transferred to a workstation at Los Alamos for processing and analysis.

Regional Characterization

Quaternary sediments, including sands, clays, and gravel, now cover a large portion of the Shagan River Test Site. The area can be divided into two regions, a northeast region comprising alluvial deposits overlying folded and faulted Paleozoic sedimentary rocks, and a southwest quadrant comprising a large granodiorite body that intruded into the surrounding sedimentary rocks. This intrusive complex is encountered in two boreholes and can be inferred to connect beneath the alluvium. We conclude that these variations in the shallow geology cause a large range of *R*g group velocities.

Using a tomographic inversion technique, we can observe relatively high velocities to the southwest and lower velocities to the northeast. The boundary separating the two zones roughly coincides with the Chinrau fault. Sequences of tuffs and alluvium exist to the northeast of this boundary overlying Paleozoic sedimentary rocks, and to the southwest, crystalline rock is predominant.

Figure 2 is a tomographic map of *R*g velocities at t = 1 s and of event and station locations for the borehole closures at the test site.

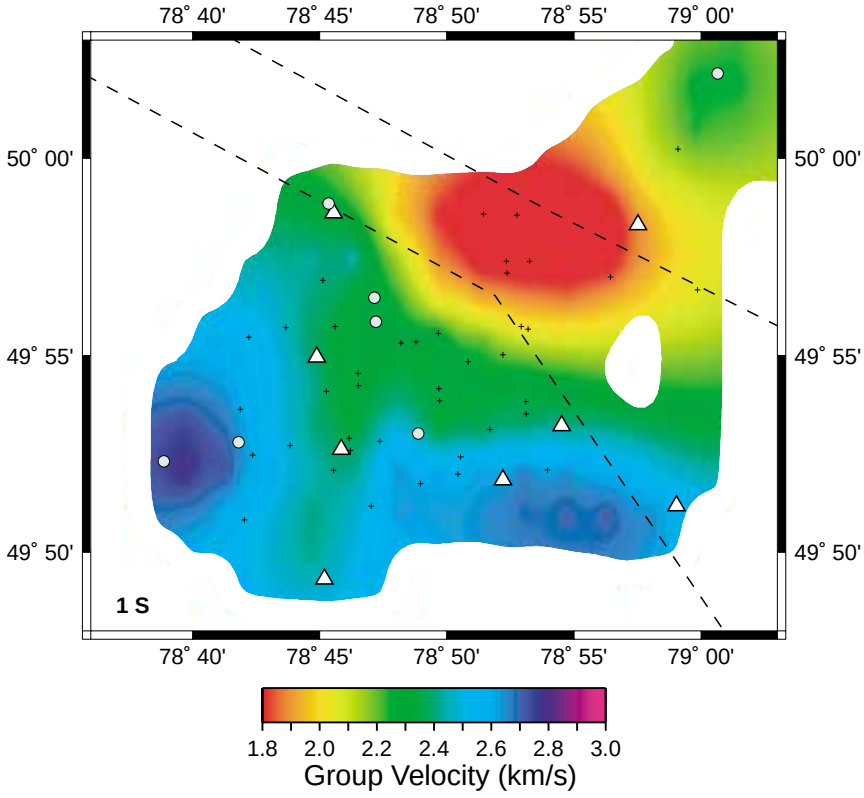

Figure 2. Tomographic Map of Group Velocities.
This plot of *R*g velocities at t = 1 s shows the locations of the borehole-closure explosive events (circles) and seismic stations (triangles) for the Shagan River Test Site. The midpoints for each path are shown as plusses. The dashed lines show the subregions of the test site as determined by magnitude residuals (Ringdal et al. 1992).

Effect of Regional Geology

Differences between the northeast and southwest regions at the test site have been known for some time on the basis of teleseismic *P*-wave spectral and waveform differences from nuclear explosions. Additionally, more recent studies have indicated contrasts in *L*g amplitudes for these two regions. Specifically, P. D. Marshall observed in 1985 that *P* waves from nuclear explosions at that site fell into two distinct classes: northeast and southwest.

The northeast *P* waveforms are more complex and have lower corner frequencies than those from southwest explosions of similar magnitude. The *P* waveforms from the northeast explosions exhibit a few cycles of ringing not observed on the simple waveforms from the southwest. It has been suggested that changes in source material properties are the cause of the observed differences, although very little geologic information was available at the time. In 1988, R. C. Stewart also noted that the northeast explosion *P* waveforms had a smaller, longer-period, first negative pulse (presumably *pP*) than those from the southwest. It has been suggested that the greater *(P – pP)* times and longer period *pP* pulses are due to greater scaled depth of burial or slower uphole velocities in the northeast.

More recent studies have also delineated zone differences in *L*g amplitudes across the test site. In 1992, F. Ringdal made maps of amplitude variations of magnitude residuals between *P* and *L*g waves across the site suggesting as much as 0.15 magnitude units between the northeast and southwest regions (with the southwest having larger values). At this time, more geologic information was available as a result of the activities associated with the Threshold Test Ban Treaty experiments and the Joint Verification Experiment. It was recognized that the northeast portion of the test site was characterized by larger-thickness sedimentary sequences than the southwest portion. This difference indicates that the northeast

explosions are characterized by some combination of lower-amplitude *P* waves and larger-amplitude *L*g waves relative to the southwest. Analysis of magnitudes from four nuclear explosions having announced yields suggested that the *P* waves were affected by the zonal differences, whereas the *L*g waves were not. However, this analysis is based on a very small data set, and it is possible that the results are not statistically significant.

In the experiments conducted in 1997 and 1998, we attempted to determine the lateral variations in the velocity structure at the former Soviet test site by using the properties of explosion-generated *R*g observed locally. For explosions detonated on or near the Earth's surface, *R*g is often the dominant arrival at local to near-regional distances. *R*g group velocities are controlled by the velocity variations in the upper few kilometers of crust along the propagation path. The phase is highly attenuated in regions of complex terrain and is most prominent on paths composed of low-velocity sediments or weathered rock.

The spatial variations in velocities from this study are consistent with the observations of teleseismic *P* waves and *L*g waves from the Shagan River Test Site nuclear explosions. For example, it is expected that explosions detonated in a region having low-velocity sedimentary layers overlying crystalline basement will show *P* waveforms that are more complex and lower-frequency than those detonated in crystalline rock. The complex waveforms and larger *pP* delays are presumably due to near-surface reverberations and lower uphole velocities.

As discussed above, it is possible that the northeast explosions have relatively larger amplitude *L*g waves than those from the southwest. *L*g signals from explosions are thought to be enriched by scattered *R*g waves in the frequency band from about 0.5 to 3 Hz. It is expected that explosions detonated in a region having a low-velocity surface layer overlying a crystalline basement will excite relatively large-amplitude *R*g that will scatter into *L*g (as suggested by Myers in 1999, as part of this same experiment). Thus, the spatial and depth variations in velocity observed as part of this study are consistent with an enhancement of *L*g amplitudes (partially through *R*g to *L*g scattering).

All of the above discussion neglects the effects of secondary sources such as spall and cavity rebound occurring in the near-source region. These secondary-source effects are very complex and will certainly depend on near-source material properties. Quantification of these effects can be undertaken through elastic and nonlinear modeling but will not be unique and are beyond the scope of this article. However, now that some more quantitative information on near-source velocity structure is available from this study, it may be possible in future work to improve our understanding of observed waveform differences across the Shagan River Test Site.

Location Accuracy of IMS Stations

During the course of these experiments, we were able to test how well three 25-ton chemical explosions (body wave magnitude m_{bLg} of 1.8 to 2.6) could be located using IMS seismic stations. Locations relative to the first, shallowest, and best-recorded explosion fell under 1 km from known locations. (We hope that the successful relocation of these small Balapan shots will support the role of calibration explosions in verification monitoring and special event studies, including on-site inspection).

Ground-truth data, that is, seismic data from well-documented earthquakes, mine explosions, or explosions carried out for seismic calibration purposes, provide travel-time path calibration, allowing high-precision location of nearby seismic sources relative to the ground-truth event. Using relative location methods, we have successfully matched nuclear explosions with satellite imagery. These explosions were of high magnitude (m_b of 4.8 to 6.1 for the Balapan tests studied by Thurber et. al, 1993), and studies employed data from many stations. Calibration using ground truth is especially important for small sources because, in general, few data are available, and results are heavily influenced by path-sensitive regional arrival times.

Fortunately, ground-truth sources provide more than travel-time path corrections; they also provide waveforms that can be used to obtain precise relative arrival times for use in special event studies. Waveform similarity and the precise determination of relative arrival times have been intensively investigated in verification work and used in high-precision relative location of nuclear tests. Successful demonstrations of such processing and relocation techniques, especially for small sources, will support the use of calibration shots as an effective component of treaty verification and on-site inspection. Calculated locations fell 590 and 960 m from the actual ground-truth epicenters, whereas origin times were delayed 45 and 115 ms from ground-truth shot times.

One could argue that this test benefited from a number of favorable conditions and thus portrays an optimistic view of the ability of the IMS to perform calibrated location. Favorable conditions include the similar source type and sizes, good propagation characteristics in the vicinity of the source region, and the abundance of regional stations, beginning at 86 km, around the test site. These factors have helped us obtain high-quality, similar waveforms of sufficient number to

constrain locations well. These facts should be kept in mind before extending results of this case study to other areas and to natural events.

However, the study suffered from a number of factors. The use of surrogate, three-component stations instead of the planned arrays resulted in poor azimuthal distribution and noise levels that degraded waveform similarity in a few cases. Clock error eliminated otherwise high-quality data from station ZAL, and there were the aforementioned modeling errors for crustal phases. In the future, improvements to the IMS network, such as uniform timing and upgrades to arrays, will increase the quality of available data and further lower magnitude thresholds for accurate relative location.

The Shagan River case study suggests a new method of calibration. A tripartite array of shots would allow the calibration of travel times and apparent velocities, enabling precise relative relocations to be performed without models and model error effects. This type of calibration would be especially effective in the reciprocal sense, where the tripartite array of shots is placed around IMS stations and currently operating or temporary stations cover the surrounding regions. Obviously, the expense of additional shots is a drawback, and whether or not the improved location ability justifies that expense would be a matter for discussion. However, the demonstration of such techniques in a well-covered and politically favorable region could lend support to arguments concerning the verifiability of a CTBT.

Conclusions

We took advantage of chemical explosions conducted in 1997 to 1998 to seal off boreholes at the former Soviet test site at Shagan River, Kazakhstan, to test the ability of the proposed IMS network to locate accurately small explosive sources (25 tons, m_{bLg} of 1.8 to 2.6) following path calibration based on ground-truth information from one shot. The study was carried out in a blind manner, after which the full suite of ground-truth data was employed to evaluate errors. Results obtained using the master-event technique fell within 1 km of known ground truth. The 90% confidence ellipses covered 12 to 13 km^2 (Figure 3), far less than the standard required by on-site inspection (1,000 km^2) and approaching the precision needed to associate events with overhead imagery. We hope the successful demonstration of relative relocation techniques will support the use of chemical explosions to calibrate the IMS and for special event studies, including on-site-inspection-related work.

Tomographic imaging based on dispersion of locally recorded *R*g waves shows that variations in geologic structure have a significant effect on *R*g group velocities at the Shagan River Test Site. Maps of *R*g group velocity show that the southwest region of the test site is characterized by faster velocities than the northeast section. As an example, *R*g waves with a period of 1 s propagate with velocities greater than 2.3 km/s for the southwest section of the test site while propagating at less than 2.3 km/s for the northeast section.

Surface geologic maps and borehole lithology logs for the region show that the slow region in the northeast section of the test site correlates well with sedimentary rocks and tuff deposits overlain by alluvium. A large granodiorite body that has intruded the sedimentary rocks appears to correlate well with the fast velocities in the southwest region. The inversions of the *R*g dispersion curves give shear wave velocities for the southwest region that are on average 0.4 km/s greater than the northeast region. At depths greater than 1.5 km, the standard deviations for the models begin to overlap, and the statistical

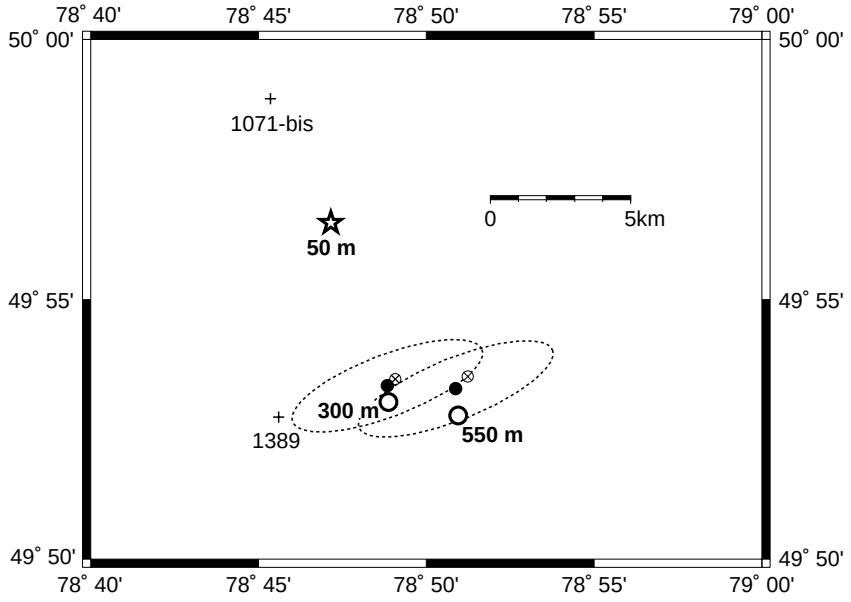

Figure 3. Confidence Ellipses for Shots at the Shagan River Test Site. The plot shows blind test, master-event locations, and 90% confidence ellipses for the 300- and 550-m shots at Shagan River. The 50-m master event is denoted by a star, and actual locations of 300- and 550-m shots are represented by open circles. Locations and errors for depths constrained to the depth of the master event are represented by closed circles and dashed lines, respectively. Locations for depths constrained to true depths are represented by circle-x symbols. Locations of depth-of-burial shots not used in the study are denoted by crosses.

difference between the models is no longer significant.

The systematic variation in the relative patterns of *P*-wave complexity as well as *P* and *L*g source size estimators across the test site correlate with the two geophysically distinct regions obtained from this study. Future studies should focus on the quantification of how the velocity structure at the test site influences the regional and teleseismic nature of *P*- and *L*g-wave seismograms. ■

Acknowledgments

We thank the National Nuclear Centre of Kazakhstan, the prototype International Data Centre, the IRIS Data Management Center, and Columbia University Lamont Doherty Earth Observatory for making data available for this study. We also acknowledge technical and processing assistance from many individuals, including Hans Israelsson, Keith McLaughlin, Howard Patton, George Randall, Brian Stump, Bob Herrmann, Luke Kluchko, C. L. Edwards, and Diane Baker. We used the LOCSAT routine (Nagy 1996), as well as GMT and SAC software.

Project Collaborator: J. L. Bonner, Southern Methodist University.

Further Reading

Bache, T. C., S. R. Bratt, and H. Bungum. 1986. High-frequency P-wave attenuation along five teleseismic paths from central Asia. *Geophysical Journal of the Royal Astronomical Society* **85**: 505–522.

Bungum, H., and E. S. Husebye. 1971. Errors in time-delay measurements. *Pure and Applied Geophysics* **91**: 56.

Gupta, I. N., W. W. Chan, and R. A. Wagner. 1992. A comparison of regional phases from underground nuclear explosions at East Kazakh and Nevada Test Sites. *Bulletin of the Seismological Society of America* **82**: 352–332.

Gupta, V. 1995. Locating nuclear explosions at the Chinese Test Site near Lop Nor. *Science and Global Security* **5**: 205.

Gupta, V., and D. Rich. 1996. Locating the detonation point of China's first nuclear explosive test on 16 October 1964. *International Journal of Remote Sensing* **17:** 1969–1974.

Israelsson, H. 1990. Correlation of waveforms from closely spaced regional events. *Bulletin of the Seismological Society of America* **80**: 2177.

Jih, R. S., and R. A. Wagner. 1992. Path-corrected body-wave magnitudes and yield estimates of Semipalatinsk explosions. Teledyne-Geotech TGAL-92-05. Alexandria, VA.

Kim, W. Y, et al. 1996. Broadband and array observations at low noise sites in Kazakhstan: Opportunities for seismic monitoring of a comprehensive test ban treaty. In *Monitoring a Comprehensive Test Ban Treaty*, E. S. Husebye and A. M Dainty, editors. The Netherlands: Kluwer Academic Publishers, p. 836.

Kocaoglu, A. H., and L. T. Long. 1993. Tomographic inversion of *R*g wave group velocities for regional near-surface structure. *Journal of Geophysical Research–Solid Earth* **98**: 6579–6587.

Marshall, P. D., et al. 1985. Body wave magnitudes and locations of Soviet underground explosions at the Semipalatinsk Test Site. AWRE report no. 0 16/84 (re-issue) HMSO.

Myers, S. C., W. R. Walter, K. Mayeda, and L. Glenn. 1999. Observation in support of *R*g scattering as a source of explosion S waves: Regional and local recordings of the 1997 Kazakhstan depth of burial experiment. *Bulletin of the Seismological Society of America* **89**: 544–549.

Nagy, W. 1996. New region-dependent travel-time handling facilities at the IDC: Functionality, testing and implementation details. SAIC technical report 96/1179, p. 57.

Patton, H. J., and S. R. Taylor. 1995. Analysis of *L*g spectral ratios from NTS explosions: Implications for the source mechanisms of spall and the generation of *L*g waves. *Bulletin of the Seismological Society of America* **85**: 220–236.

Phillips, W. S., et al. 2000. Precise relative location of 25-ton chemical explosions at Balapan using IMS stations. Submitted to *Pure and Applied Geophysics* (PAGEOPH).

Ringdal, F. 1990. Teleseismic event detection using the NORESS array, with special reference to low-yield Semipalatinsk explosions. *Bulletin of the Seismological Society of America* **80**: 2127–2142.

Ringdal, F., P. D. Marshall, and R. W. Alewine. 1992. Seismic yield determination of Soviet underground nuclear explosions at the Shagan River Test Site. *Geophysical Journal International* **109**: 65–77.

Shearer, P. M., and L. Astiz. 1997. Locating nuclear explosions using waveform cross-correlation. In *Proceedings of the 19th Annual Seismic Research Symposium Mon. CTBT*, p. 301. Alexandria, VA: Defense Special Weapons Agency.

Stewart, R. C. 1998. P-wave seismograms from underground explosions at the Shagan River Test Site recorded at four arrays. AWE report O 4/88, Aldermaston, UK.

Sykes, L. R., J. S. Deng, and P. Lyubomirskiy. 1993. Accurate location of nuclear explosions at Azgir, Kazakhstan, from satellite images and seismic data: Implications for monitoring decoupled explosions. G*eophysical Research Letters* **20**: 1919–1922.

Thurber, C. H., H. R. Quinn, and R. Saleh. 1994. Catalog of locations of nuclear explosions at Balapan, Kazakhstan, 1965 to 1985. *Bulletin of the Seismological Society of America* **84**: 458–461.

Thurber, C. H., H. R. Quinn, and P. G. Richards. 1993. Accurate locations of nuclear explosions in Balapan, Kazakhstan, 1987 to 1989. *Geophysical Research Letters* **20**: 399–402.

Volcanic Risk Studies for the U.S. and Japanese Geologic Repository Programs

F. V. Perry (EES-9, fperry@lanl.gov), G. A. Valentine (EES-6), and B. M. Crowe (EES-9)

The major concern surrounding storage of high-level radioactive waste in a geologic repository is the possible release of radionuclides to the environment. The most likely mechanism for such a release is by gradual dissolution of waste, followed by transport of radionuclides in groundwater. In tectonically active regions, another mechanism, a volcanic eruption, might directly or indirectly lead to radionuclide release. Since the early 1980s, we have assessed volcanic risk as it relates to the potential U.S. repository for storage of high-level radioactive waste at Yucca Mountain, Nevada, and more recently, for the Japanese high-level waste disposal program.

As the lead Department of Energy team for volcanic hazard studies for the Yucca Mountain Site Characterization Project (YMP), we have developed methods for assessing the probability of volcanic disruption of the potential repository and for assessing the consequences of a volcanic disruption, primarily by conducting studies of analog volcanic systems. These studies ended in 1996. In the past two years, we have focused on supporting the YMP Site Recommendation and License Application by analyzing and integrating new information with previous studies.

Since 1998, we have expanded on our Yucca Mountain work by conducting volcanic risk studies for the Japan Nuclear Cycle Development Institute (JNC) to support the Japanese geologic repository program. Using an analog composite volcano, Summer Coon, in southwestern Colorado, we have assessed the hazard and consequences of a composite volcano disrupting a Japanese geologic repository.

Yucca Mountain Project Studies

The need to assess the possibility of a volcanic eruption disrupting the potential repository at Yucca Mountain is driven by the occurrence of eight small-volume (<1 km^3) Quaternary (<1.6 million years) basaltic volcanoes within 50 km of Yucca Mountain. Six of these volcanoes lie within 20 km of the repository site (Figure 1). For our site characterization studies for the YMP, we have used geochronology techniques to establish the age and recurrence rate of volcanism and field and geochemistry studies to understand the mechanisms of volcano formation in the region.

Determining the ages of volcanoes older than approximately 1 million years has been relatively straightfor-

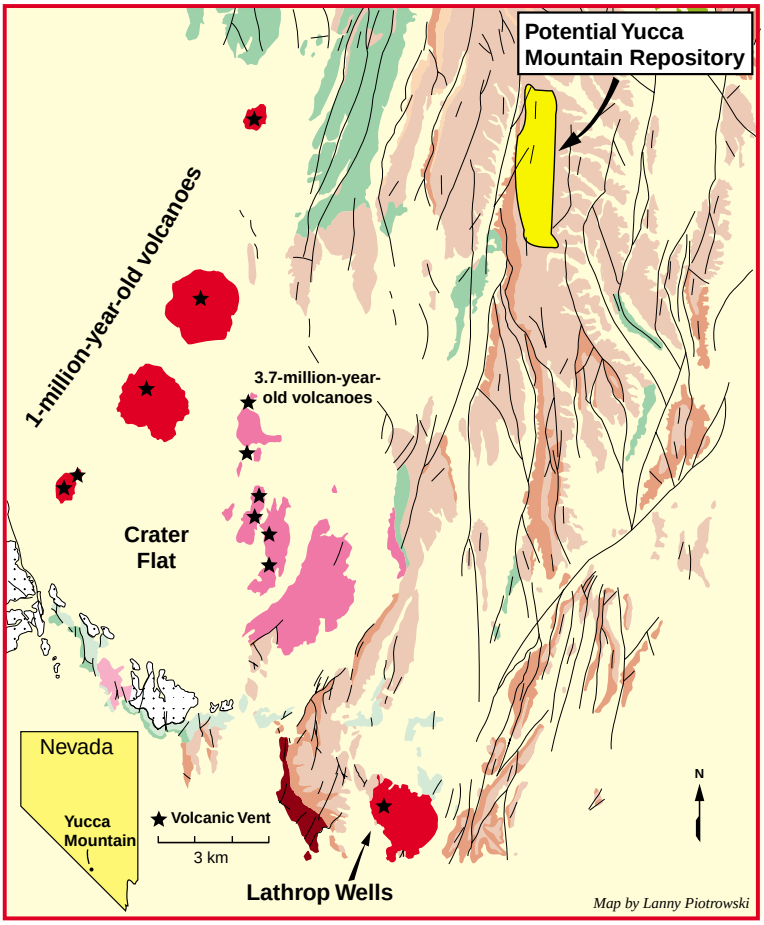

Figure 1. Volcanoes Near Yucca Mountain.
A dozen volcanoes are within 20 km of the potential repository site. Six volcanoes have been active within the last million years; the other six, within the last 4 million years. The youngest volcano, at Lathrop Wells, is 75,000 years old.

ward using $^{40}Ar/^{39}Ar$ techniques. Determining a reliable age for the Lathrop Wells, the youngest volcano near Yucca Mountain, has been technically challenging. We have applied multiple chronology techniques, which have yielded ages ranging from approximately 10,000 to 150,000 years. Using $^{40}Ar/^{39}Ar$ isotopic methods to date both whole-rock basalt and thermally reset sanidine from tuff xenoliths, we have determined only recently that Lathrop Wells is approximately 75,000 years old.

Probabilistic Methods. For the YMP, our major goal has been to assess the probability that magmatic processes will disrupt the potential repository during the performance period of waste containment (10,000 years as set by the Environmental Protection Agency regulation). Using results of site characterization studies of Yucca Mountain as the geologic framework, we estimated the probability that a new volcano will form in the Yucca Mountain region over the next 10,000 years. Given that a new volcano does form, we determined the probability that it will disrupt the repository.

We expressed the probability of magmatic disruption as the annual probability that a volcanic event will disrupt (or intersect) the repository, conditional on a volcanic event occurring during the time period of concern. In its simplest form, the probability of disruption is calculated by multiplying the recurrence rate of volcanism by the intersection ratio (repository area/area in which volcanism occurs), taking into account uncertainties in each value. We formulated the disruption of a repository by a volcanic event as a conditional probability

$$Pr_{dr} = Pr(E2 \text{ given } E1)Pr(E1),$$

where Pr_{dr} is the probability of magmatic disruption of a repository, *E1* denotes the rate of occurrence of volcanic events, defined as the formation of a *new* small-volume basaltic volcanic center in the Yucca Mountain area, and *E2* is the probability of intersection of the repository or repository area by that volcanic event. This probability is expressed mathematically as

$$Pr[\text{no magmatic event before time } t] = \exp^{(-ltp)},$$

where l is the recurrence rate, t is time, and p is the probability that an event is disruptive. This probability model assumes a homogeneous Poisson distribution of volcanic events in space and time. Critical assumptions of a Poisson distribution are that the events occur independently, they are exponentially distributed in time t, and the probability of more than one event occurring at the same time is vanishingly small.

Our early calculations of the annual probability of magmatic disruption of the Yucca Mountain Site produced estimates of between 5×10^{-8} to 3×10^{-10} disruptions per year (Figure 2). It is important to note that these calculations were conducted in the early 1980s, while the YMP was still in the initial stages of site characterization studies. Our estimates, along with those of researchers at Sandia National Laboratories and the U.S. Geological Survey, led to general, but not universal, acceptance that the Yucca Mountain site would not be disqualified as a location for a repository because of the risk of volcanic hazards.

Our volcanism studies at Los Alamos continued through the mid-1990s, while the YMP shifted its emphasis from site characterization studies to constructing an exploratory test facility at the site. During this interval, an attempt was made to complete probability modeling through application of Monte Carlo simulation modeling. We used Monte Carlo simulation modeling to examine each attribute of the conditional probability model systematically. Both the recurrence rate and the disruption ratio were assessed using all combinations of alternative models, including models developed by the State of Nevada and the Nuclear Regulatory Commission.

We modified the resulting probability distributions to eliminate combinations of spatial and structural models that excluded volcanic events. This important effect was not included in probability calculations where *E1* and *E2* were independently estimated. The modified matrix of probability distributions was solved using simulation modeling to give aggregate distributions of the annual probability of disruption for a repository block in Yucca Mountain. Our results indicated that the mean probability of disruption of the potential YMP repository is $1.9 \times 10^{-8} \pm 1.6 \times 10^{-8}$ per year.

In an attempt to bring probability estimates to resolution, the DOE convened a formal expert judgment panel in 1995 to independently assess the probability of volcanism at Yucca Mountain. A 10-member panel of volcanism experts nominated by their scientific peers was assembled, and the panel completed a probabilistic volcanic hazard assessment (PVHA).

Each panel member independently estimated probability distributions, which were then aggregated. The aggregate result yielded a mean annual probability of magmatic disruption of 1.5×10^{-8}, with a 90-percent confidence interval of 5.4×10^{-10} to 4.9×10^{-8}. The mean and confidence interval of this distribution was virtually identical to our previous probability estimates, as can be seen in Figure 2.

Analog Studies

To conduct a comprehensive risk assessment, one must know both the probability and the consequences of volcanic events. For our first type of consequences study, we attempted to constrain the amount of debris that could be exhumed from repository depths by studying the concentration and composition of shallow crustal

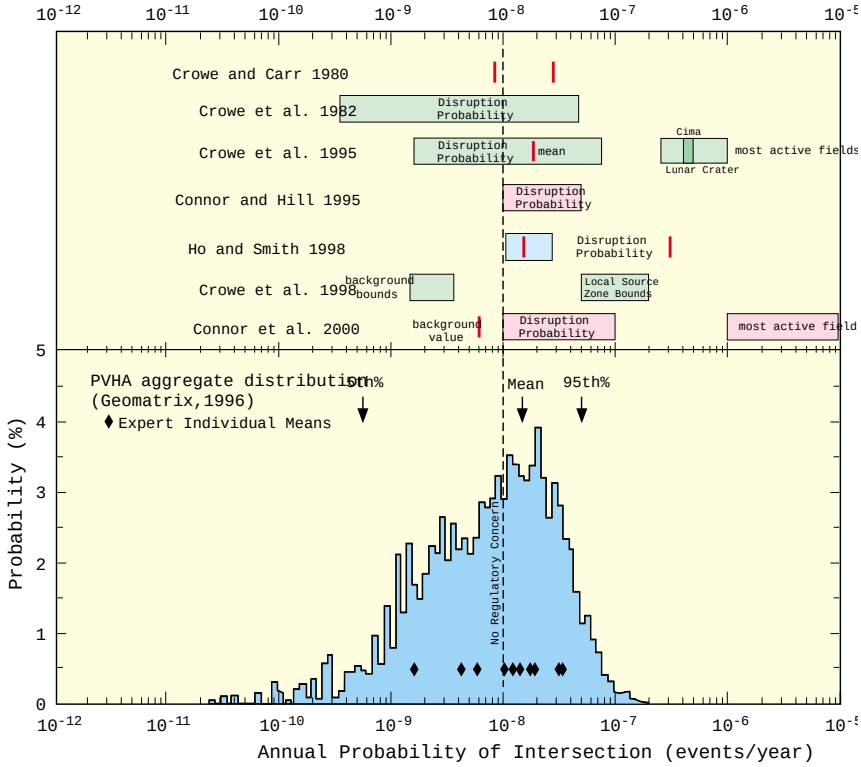

Figure 2. Probability of Future Volcanic Activity at Yucca Mountain.
A number of researchers has analyzed the likelihood of a volcano disrupting a repository at Yucca Mountain. Their probability point estimates (single lines) and ranges (rectangles) are compared here with estimates made by a panel of experts convened by the DOE to assess the hazard (PVHA distribution). The ranges labeled "most active fields" and "Local Source Zone Bounds" represent upper bounds for the probability and assume that the repository is placed in an active volcanic field. The background bounds and value represent lower bounds that assume the repository does not lie in an active volcanic field but lies in a region that produces only sporadic eruptions. Most estimates put the disruption probability at a little greater than 10^{-8} events per year, which translates to a 1 in 7000 chance that volcanic activity could disrupt the repository.

xenoliths at several analog volcanoes that encompass the range of eruptive processes that might occur in the Yucca Mountain region. These analog volcanoes are located in areas in which there are good constraints on subsurface, layer-cake geology from a combination of regional exposures and water and petroleum wells. This fact enabled us to quantify the erosion of wall rock as a function of depth and eruptive process.

Unfortunately, the applicability of these studies has decreased with the recent changes in repository design, in which the waste packages will sit in open, rather than backfilled, drifts. This new design raises the possibility that, given an igneous event at the repository (with or without an attendant eruption), hundreds to thousands of waste packages could be partially destroyed by explosive fragmentation of magma into the drifts. The largest potential effect of destroying the integrity of the waste packages this way is on the subsequent groundwater transport of dissolved radionuclides.

In our second type of analog study, we focused on the hydrothermal and mechanical effects associated with intrusion of basalts into silicic tuffs. Results of studies in which the host tuffs are both vitric and altered suggest that alteration is limited to within a few meters of the tuff-basalt contacts. These studies are being reopened from a new perspective, and we are using the sites as analogs to study the effects of repository thermal loading (from radioactive decay) on the surrounding rocks.

Studies for the JNC

The Japanese islands are in a complex plate-tectonic setting, and as a result, they are one of the more tectonically and volcanically active areas on the Earth. Approximately 350 volcanoes have been active in Japan in the past 2 million years. Thus, within the next 100,000 years, it can be expected that several new volcanoes will form in Japan. In terms of volcanism, we must consider two primary factors when selecting the site for a geologic repository in Japan. These factors are (1) the rate of new volcano formation in a particular region and (2) the distance at which a volcano presents a hazard to a nearby repository.

As part of our studies for the JNC, we used the Oligocene Summer Coon volcano in southern Colorado, with its well-exposed system of radial dikes (Figure 3), as an analog for similar composite volcanoes in Japan. Using Summer Coon, we were able to estimate the probability of repository disruption by a radial dike system, conditional on a volcano forming nearby.

Erosion has removed much of the original volcanic edifice at Summer Coon, exposing an extensive radial dike system that is probably typical of large composite volcanoes in Japan. Intruding early mafic cone-breccia deposits are numerous (>100–200) at Summer Coon; and basaltic andesite and andesite (mafic) dikes with typical widths of 1 to 3 m are also present. Intruding both the early mafic and silicic cone breccias are about 25 dacite (silicic) dikes with typical widths of 10 to 20 m. The silicic dikes are on the average longer than the mafic dikes (Figure 3) and form prominent topographic features.

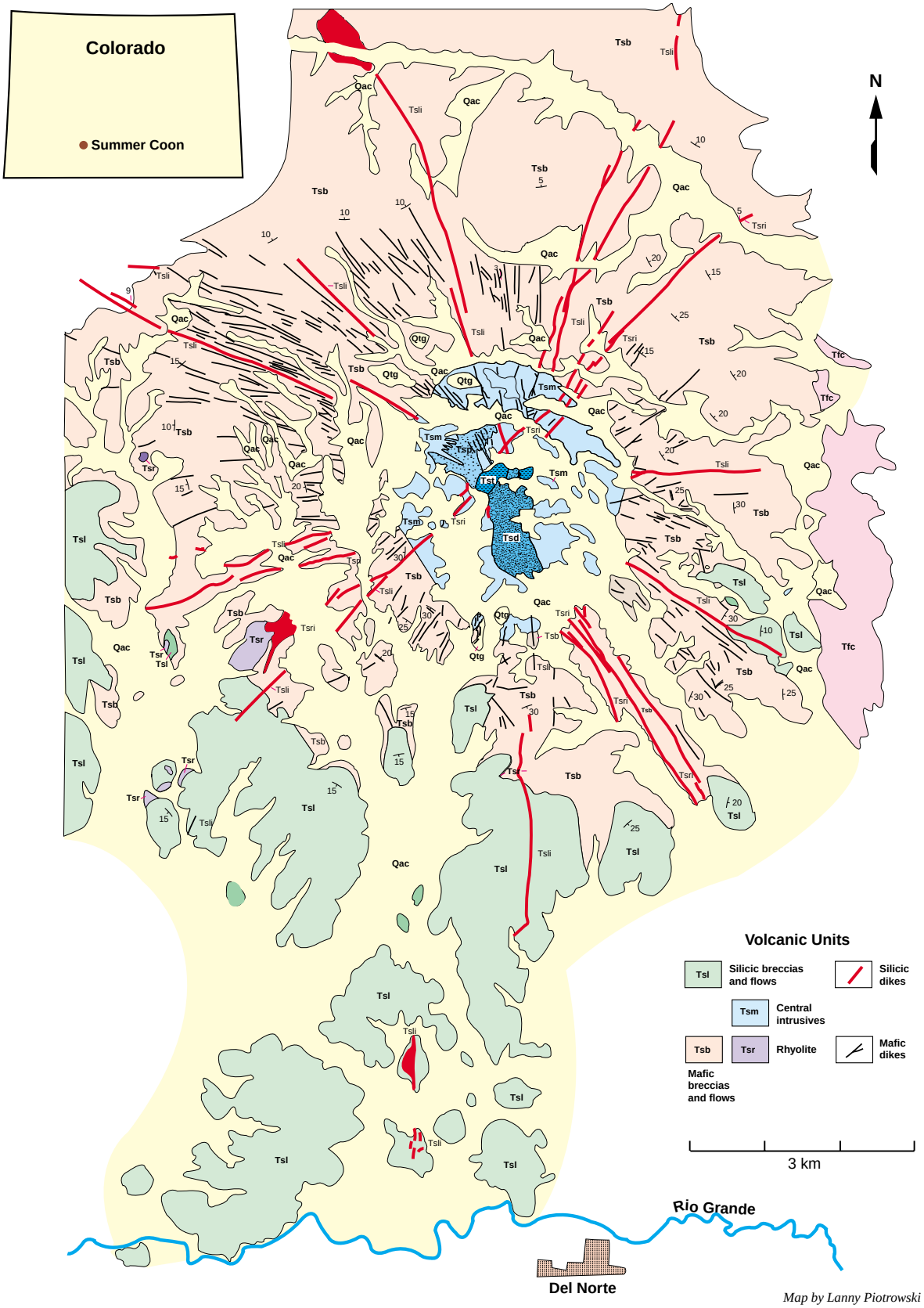

Figure 3. Summer Coon.
A geologic map of the Summer Coon volcano.

We developed a Monte Carlo simulation model that estimates the probability of dike intersection as a function of (1) distance from the center of a composite volcano, (2) repository area, and (3) radial dike density and length. Although we have assessed the hazard of a dike intersecting a geologic repository for the case of small-volume basaltic volcanism at Yucca Mountain, we are not aware of any previous analysis of the hazard to a repository from the radial dike system of a large composite volcano.

Summer Coon Studies. To estimate the conditional probability that a dike from a new volcano will intersect a repository, we estimated the number of dikes and their spatial distribution, the distribution of dike lengths, and the area and shape of the repository. We based the number of dikes on dike counts at Summer Coon, and we chose a log-normal distribution to represent both the mafic and the silicic dike-length distributions, based on dike-length data from Summer Coon. For the repository area, we used two values, 4 km^2 and 8 km^2, that encompass a range of areas typically proposed for repository designs internationally; and for geometric simplicity, we assumed that the shape was circular.

The mathematical logic for the probability model is based on the trigonometry of a right triangle (Figure 4). The probability model was programmed (using Microsoft Excel Visual Basic and Decisioneering Crystal Ball add-in functions for Excel) to sample probability distributions using Monte Carlo simulation. The model simulates the geometry of dike emplacement and tests for two conditions, which, if true, result in a dike intersection of a repository: (1) Does the radial dike have an orientation that could result in a dike intersection (i.e., is within the angle 2θ)? (2) If the first condition is true, is the dike long enough to intersect the repository?

A single Monte Carlo realization of a complete radial dike emplacement (120 mafic dikes, 30 silicic dikes) is shown in Figure 4. For the Summer Coon cases, 1,000 realizations of the Monte Carlo simulation were run for each combination of distance and repository area calculated. In addition, a bounding case was run based on fissure length data from Mount Etna, to assess the effect of a larger radial dike system on the probability of intersection. Finally, sensitivity calculations were run (using 2,500 realizations) to assess the effect of doubling mean dike length, standard deviation of the dike length, dike density (number of dikes), and repository area.

Results are presented as the conditional probability of intersection calculated at incremental distances from the volcano center (Figure 5). Sensitivity calculations to assess the effect of doubling each of the key parameters are presented as the relative change from the base case for silicic dikes (Figure 5, inset).

Separate probabilities of intersection were calculated for the mafic and silicic dike sets at Summer Coon for both a 4 km^2 and an 8 km^2 repository (Figure 5). In all cases, the probability values decline rapidly with distance from the volcano due to the decrease in dike density dictated by the divergence of radial dikes away from the volcano center (Figure 4).

Although the silicic dikes are longer on average than the mafic dikes, they are also less numerous, causing the probability curves for mafic and silicic dikes to cross at distances of 5 to 6 km from the volcano center (Figure 5). At 4 km and less, the probability of intersection is 1 for the mafic dike set because of high dike density. For the longer, silicic dike set, a probability of 1 is reached at a distance of 2 or 3 km, depending on the repository area.

The shorter length and smaller dispersion in the length of the mafic dikes result in a steeper drop in probability values compared to the

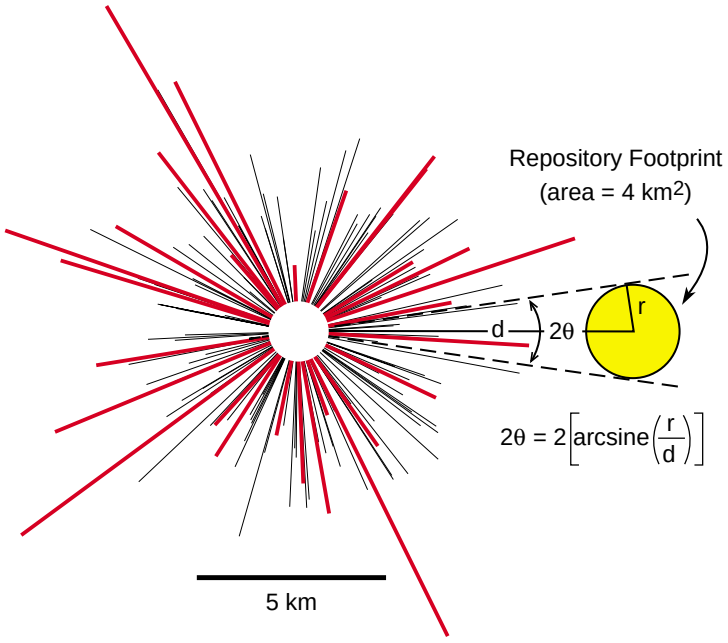

Figure 4. Mathematical Basis for Monte Carlo Simulation of Probability of Dike Intersection.
Probability of dike intersection is dependent upon the dike density and length on the area of the repository (dependent on the radius, *r*), which, together with distance to the volcano (*d*), define the 2θ angle that dikes must fall within to be able to intersect the repository. An example of a single simulation realization is shown, using the dike length parameters from Figure 2, assuming 120 mafic dikes, 30 silicic dikes, and a uniform radial distribution of dike orientations.

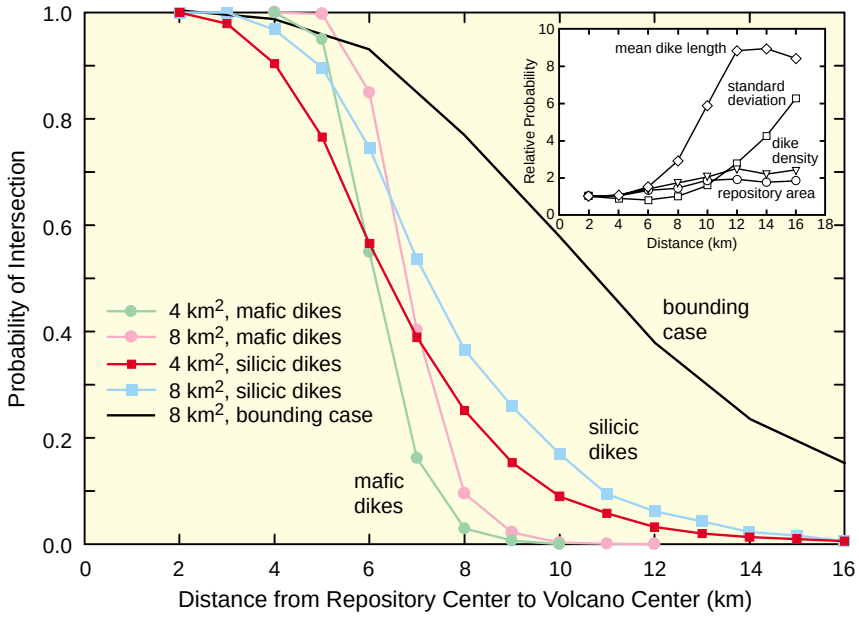

Figure 5. Distance of the Repository Center from the Volcano Center Versus the Probability of Dike Intersection of a Repository.
Probability of intersection for both mafic and silicic dikes based on data from Summer Coon volcano are shown, as well as a bounding case using dike lengths approximately double those of silicic dikes at Summer Coon. Results are shown for repository areas of 4 and 8 km^2. Inset shows sensitivity of the probability of dike intersection (expressed as relative probability compared to the base case for silicic dikes at Summer Coon and a repository area of 4 km^2) to doubling of dike length, dike density, and repository area. The probability of intersection is most sensitive to dike length and relatively insensitive to repository area or dike density.

silicic dikes; the probability of intersection is $<10^{-2}$ beyond 10 km distance for both repository cases. Conversely, the longer length and larger dispersion in the length of the silicic dikes results in a more gradual drop in probability values with distance. The probability of intersection for silicic dikes is $\leq 10^{-2}$ at ~14- to 15-km distance and $\leq 10^{-4}$ at 30-km distance for both repository cases.

Scientists in Japan have used several criteria to assess the distance at which a volcano can perturb the surrounding geologic environment. These criteria include geothermal gradient, heat flow, size of hydrothermal convection systems, pH and anion index of hot springs, and $^3He/^4He$ of groundwater. Collectively, these criteria suggest that the geologic environment is not perturbed beyond about 15 km from an existing volcano.

The results of our assessment indicate that the conditional probability of a radial dike intersecting a repository is $<10^{-2}$ beyond a distance of approximately 15 km from the center of a typically sized composite volcano. The Japanese data and our probabilistic assessment suggest that the volcanic hazard to a geologic repository is minimal if the new volcano forms at a distance greater than about 15 to 20 km from the repository. ■

Acknowledgments

Many Los Alamos staff and students have contributed to the studies, including David Vaniman, Larry Auer, Richard Beckman, Lynn Bowker, Emily Desmarias, Kean Finnegan, Carl Gable, Fraser Goff, Gordon Keating, Karen Carter Kroug, Mike Murrell, Jane Poths, Nina Rosenberg, Phil Stauffer, Giday WoldeGabriel, and Rick Warren.

Collaborators

University of New Mexico
New Mexico Institute of Mining and Technology
Golder and Associates
Geomatrix, Inc.

Further Reading

Coppersmith, K. J., R. C. Perman, M. W. Pendleton, and J. L. Younker. 1996. *Probabilistic Volcanic Hazard Analysis for Yucca Mountain, Nevada*. BA0000000-01717-2200-00082, REV 0. Report DE-AC01-91RW00134, 331 pp. Las Vegas, Nevada: Civilian Radioactive Waste Management System Management and Operating Contractor.

Crowe, B. M. 1986. Volcanic hazard assessment for disposal of high-level radioactive waste. In *Active Tectonics*, pp. 247–260. Washington, D.C.: National Academy Press.

Crowe, B. M., M. E. Johnson, and R. J. Beckman. 1982. Calculation of the probability of volcanic disruption of a high-level radioactive waste repository within southern Nevada, USA. *Radioactive Waste Management* **3**: 167–190.

Heizler, M. T., F. V. Perry, B. M. Crowe, L. Peters, and R. Appelt. 1999. The age of Lathrop Wells volcanic center: An Ar-40/Ar-39 dating investigation. *Journal of Geophysical Research* **104**: 767–804.

Lichtner, P. C, G. Keating, and B. Carey. 1999. A natural analogue for thermal-hydrological-chemical coupled processes at the proposed nuclear waste repository at Yucca Mountain, Nevada. Los Alamos National Laboratory report LA-13610-MS.

Perry, F. V., B. M. Crowe, G. A. Valentine, and L. M. Bowker, editors. 1998. Volcanism studies: Final report for the Yucca Mountain Project. Los Alamos National Laboratory Report LA-13478-MS, 554 pp.

Perry, F. V., G. A. Valentine, E. K. Desmarias, G. WoldeGabriel. 2001. Probabilistic assessment of volcanic hazard to radioactive waste repositories in Japan: Intersection by a dike from a nearby composite volcano. *Geology* **29**: 255–258

Field Studies at Yucca Mountain

M. Peters (EES-7, mtpeters@lanl.gov)

Field studies have played a major role in the Yucca Mountain Project Site Characterization (YMP) since the 1970s. They have ranged from the initial surface-based borehole studies that began in the 1970s to tests conducted in the Exploratory Studies Facility (ESF), an elaborate underground installation built at the site in 1997, to various present-day experiments being conducted at remote sites around the Yucca Mountain region. In this paper we will discuss surface-based borehole testing, the Cross Drift Test and other tests in the ESF, and the Busted Butte Unsaturated Zone Test.

Borehole Studies

In the 1970s, 1980s, and early 1990s, surface-based borehole testing was the major focus of field studies at Yucca Mountain. To characterize the unsaturated and saturated zones, over 300 boreholes were drilled, many of them thousands of feet deep, above and below the water table. In Figure 1, we see an example of a typical rig used for borehole drilling.

Throughout this 20-year period, borehole-based research was conducted in a number of areas: (1) lithostratigraphy of the volcanic sequence; (2) mineralogic-petrologic characteristics of the lithostra-tigraphic units; (3) hydrologic properties of the hydrostratigraphic units; (4) thermal and mechanical properties of the thermal-mechanical units; (5) near-surface hydrology, using data from shallow boreholes; (6) hydrologic monitoring of the unsaturated zone; (7) potentiometric surface determination in the Yucca Mountain region; and (8) hydraulic and transport testing in deep boreholes to investigate the saturated-zone volcanic and carbonate aquifers.

Characterization of the core from a borehole typically consists of examining and analyzing the extracted core, and the use of geophysical techniques, such as neutron and video logging, to obtain downhole information. When the drilling is completed, instrumentation in the form of packer strings or other configurations is installed downhole to make a myriad of measurements, which provide additional data.

Figure 1. Drilling into Yucca Mountain.
A typical rig used to drill one of the 317 boreholes in Yucca Mountain.

The ESF

In the late 1980s and early 1990s, the YMP continued the surface-based borehole testing program; in addition, YMP began to cite an underground test facility, the ESF, which would be used to conduct experiments to further characterize the unsaturated zone above and within the potential repository horizon.

Several design alternatives were evaluated, including many different shaft and ramp-type tunnels; the design selected was the ramp type consisting of a north ramp, main drift, and south ramp. In Figure 2, we see the ramps of the ESF, bordered by the potential repository.

The ESF construction began in 1994 and was completed in 1997; the 5-mile loop was excavated using a 25-foot-diameter tunnel-boring machine. This machine tunneled through rocks of the Tiva Canyon, Paintbrush nonwelded tuff (PTn), and upper parts of the Topopah Spring tuff formations. The upper portion of the potential repository horizon (primarily the Topopah Spring middle nonlithophysal unit) is exposed in the ESF.

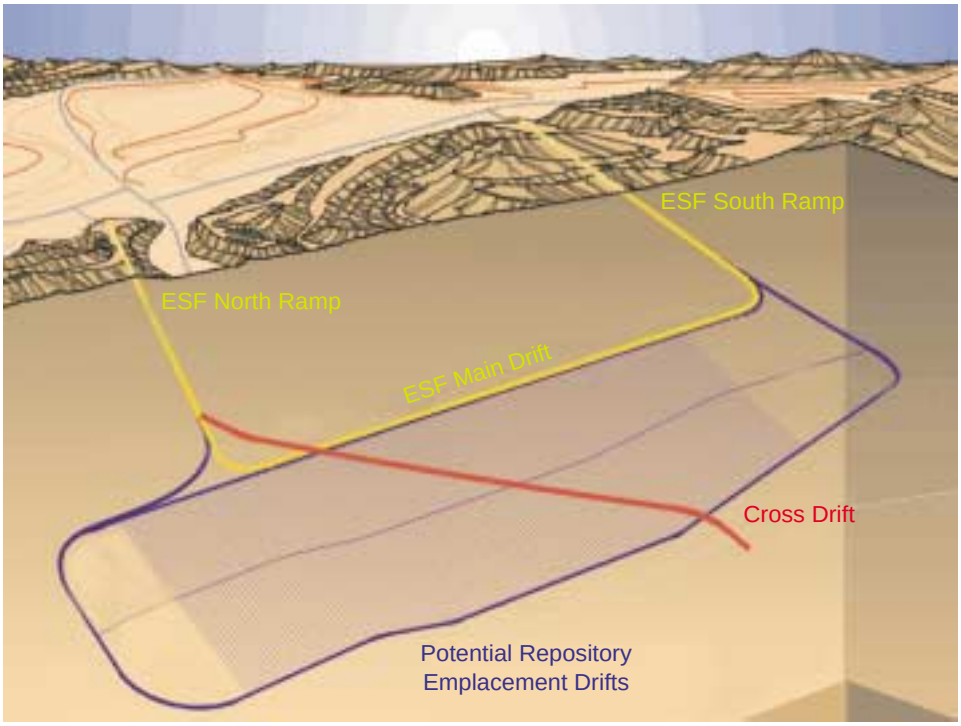

Figure 2. Potential Yucca Mountain Repository.
This cutaway shows the ramps and main drift for the Exploratory Studies Facility (yellow), completed in 1997, and the Cross Drift (red), completed in 1998, which are used to carry out a variety of tests in support of site characterization. The potential repository block is shown in blue.

Numerous research activities have been conducted in the ESF. They include geologic mapping, construction monitoring, and systematic sampling and characterization of the hydrologic, mineralogic-petrologic, thermal-mechanical, and geochemical properties of the stratigraphic units in the unsaturated zone.

A series of alcoves and niches were excavated in the ESF (Figure 3) so more specific experiments to characterize hydrologic and thermally coupled processes further could be conducted. These tests included characterizing hydrologic properties of the Tiva Canyon and PTn (Alcoves 1, 3, and 4) and of the faults in the Yucca Mountain region, namely the Bow Ridge Fault and Ghost Dance Fault (Alcove 2 and Alcoves 6 and 7, respectively). The tests also investigated thermally coupled processes in potential repository horizon rocks (Topopah Spring middle nonlithophysal unit) in Alcove 5 (Single Heater and Drift Scale Test).

Drift Scale Test. The largest and most visible test executed by the YMP in the ESF to date is the Drift Scale Test, located in Alcove 5. This test is centered around a 47-m-long simulated emplacement drift loaded with nine simulated waste packages. The drift and surrounding rock mass is instrumented with thousands of sensors, and the rock mass is heated to 200°C.

The purpose of this test is to evaluate the thermal-hydrologic-mechanical-chemical coupled processes in the potential repository horizon rocks at field scale. Results for the three (of four) years of planned heating suggest that heat transfer is conduction-dominated, with a key role played by convection of moisture. The results also indicate that pore water mobilized by heat tends to move below the heated region rather than stay "ponded" above the drift. As expected, coupled process phenomena also occurr at sub-boiling temperatures.

Other Studies in the ESF. In the mid-1990s, the Project dedicated considerable effort to understanding (1) surface infiltration, (2) the role of the PTn (nonwelded vitric tuff) in attenuating and dampening of infiltration fluxes, and (3) the resultant percolation fluxes in the potential repository horizon. Researchers used geochemical and mineralogic-petrologic evidence to better understand these important phenomena, especially percolation flux in the potential repository horizon.

Two notable data sets resulted from these studies: (1) findings on the distribution of ^{36}Cl and Cl and (2) geochronologic and geochemical results on fracture-filling minerals (primarily calcite and opal) and systematic rock samples (Sr isotope data in particular) throughout the ESF.

This work provided very useful data for the calibration of the unsaturated-zone site-scale flow and transport model. More important, the investigations of percolation flux led to the construction of four testing niches in the ESF within the Topopah Spring middle nonlithophysal unit (Niches 1, 2, 3, and 4). Testing in these niches has focused on the relationship between percolation flux and seepage into drifts (i.e., how much of the percolation flux actually enters, or "seeps," into an opening). This issue is now a key factor in understanding the performance of the natural system at Yucca Mountain because of its implication as to how much moisture may be expected to contact the waste packages eventually.

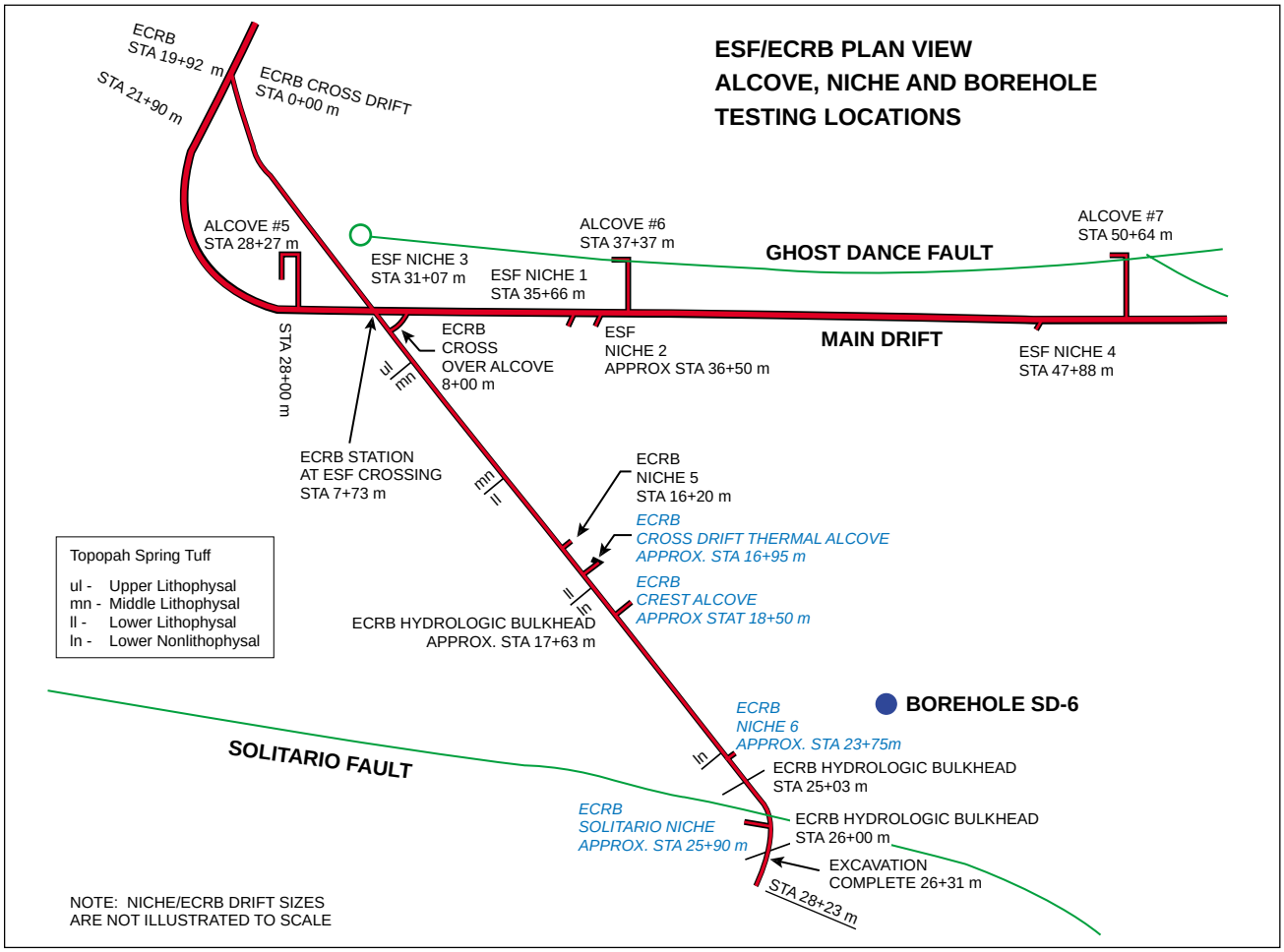

Figure 3. Plan View of the Exploratory Studies Facility and the Enhanced Characterization of the Repository Block (ECRB). The plan shows the locations of the various boreholes, alcoves, and niches used for testing, as well as the locations of the Ghost Dance and Solitario faults. The extent of the layers of the Topopah Spring Tuff are indicated with abbreviations along the Cross Drift.

In summary, the ESF niche studies suggest that the percolation flux needed to initiate seepage may be much higher than is currently observed or would even occur under wetter climate conditions in the future.

The Cross Drift Studies

One of the limitations of the ESF is that it does not expose the majority of the potential repository horizon rocks (most of the Topopah Spring lower lithophysal unit and all of the Topopah Spring lower nonlithophysal unit). Based on these limitations and numerous interactions with external oversight bodies (particularly the Nuclear Waste Technical Review Board), the YMP initiated a planning effort, termed the Enhanced Characterization of the Repository Block (ECRB), in 1997.

This effort was aimed to plan a way to characterize the potential repository block further. The result of this effort was the construction of an additional tunnel (termed the Cross Drift) across the potential repository block to expose the potential repository horizon units and the Solitario Canyon fault zone. The Cross Drift is shown in Figures 2 and 3.

Construction of the Cross Drift started in late 1997 and was completed in October 1998. Initial activities in the Cross Drift included geologic mapping, systematic sampling and analyzing hydrologic and geochemical properties, and hydrologic monitoring (all within the Topopah Spring tuff formation and the Solitario Canyon fault zone).

As in the ESF, a series of testing alcoves and niches are being developed for the Cross Drift over the next couple of years. These studies will address flow, transport, and seepage properties (Hydrologic Bulkhead Studies, Crossover Alcove, Niches 5 and 6, and Crest Alcove). Thermally coupled processes (Cross Drift Thermal Test) within the potential repository horizon rocks and the hydrologic properties of the Solitario Canyon fault zone (Hydrologic Bulkhead Studies and Solitario Canyon Fault Alcove Testing) will also be studied.

Busted Butte Unsaturated Zone Transport Test

In addition to surface and underground tests, there are experiments being conducted at remote sites around Yucca Mountain. The most notable test is the Busted Butte Unsaturated Zone Transport Test.

The goals of this testing program are to evaluate the influence of heterogeneities on flow and transport, including other aspects of the system such as fracture/matrix interactions and permeability contrast boundaries. It also considers colloid migration in the unsaturated zone. The tests are conducted in a 25-m-long underground alcove excavated at Busted Butte (Figure 4). The alcove is at the end of a long access tunnel from the surface.

Our observations so far suggest that porous media flow dominates in the vitric Calico Hills. Data both from boreholes surrounding the repository and from Busted Butte will build confidence in the unsaturated-zone flow and transport models used by the YMP. These data may show that measured sorption values for Busted Butte (vitric) rocks are greater than those currently used in models.

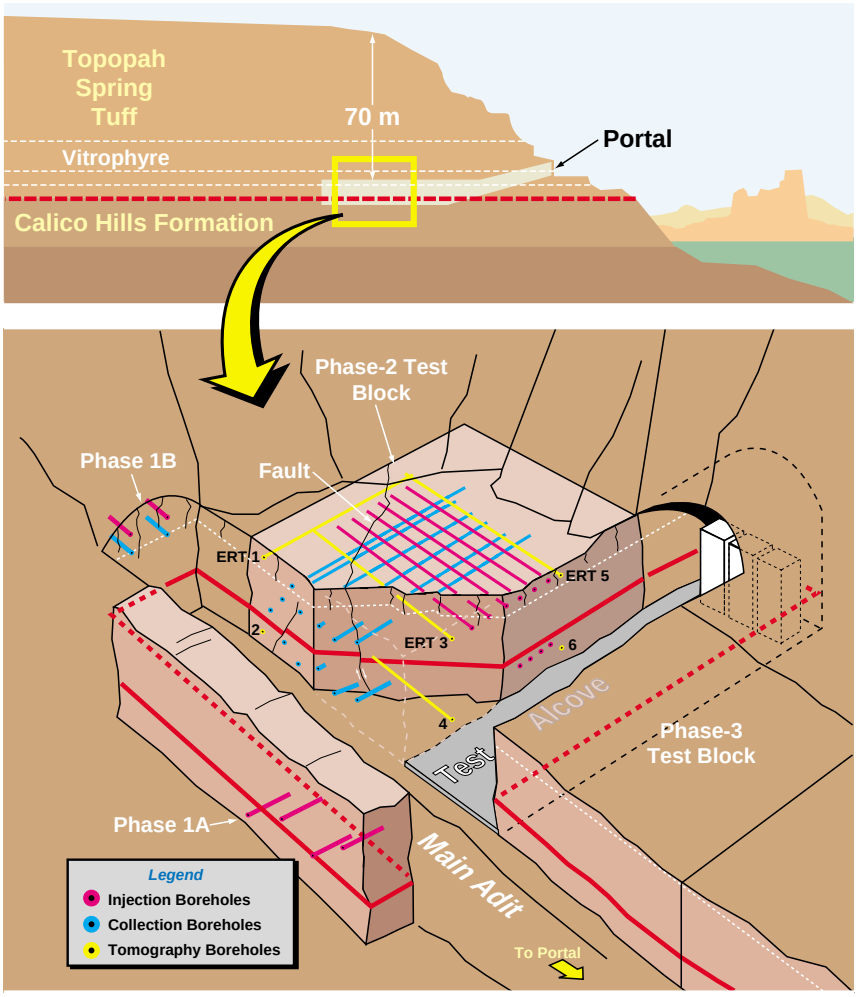

Figure 4. Busted Butte Unsaturated Zone Transport Test.
The diagram shows the layout of the field test taking place in Busted Butte that uses tracer solutions to study transport through the unsaturated zone.

Conclusions

Results from field tests at Yucca Mountain continue to provide a significant portion of the technical basis for process models, performance assessments, and repository design to support key programmatic milestones such as the 1998 Yucca Mountain Viability Assessment and the upcoming Yucca Mountain Site Recommendation. ■

Further Reading

CRWMS M&O (Civilian Radioactive Waste Management System Management and Operating Contractor). 2000. *Yucca Mountain Site Description*. TDR-CRWGS-00001, REV 01, ICN 01. Las Vegas, NV: U.S. Department of Energy, Yucca Mountain Site Characterization Office.

Bussod, G. Y., H. J. Turin, and W. E. Lowry. 1999. Busted Butte unsaturated zone transport test: Fiscal Year 1998 status report. Los Alamos National Laboratory report LA-13670-SR.

Advances in Seismic Imaging and Modeling for the Petroleum Industry

L. House (house@lanl.gov), M. Fehler, L. Huang, and P. Roberts, with S. Hildebrand, D. Alde, and C. Aprea (EES-11)

The oil and gas industry has relied on seismic reflection methods as its primary exploration tool for more than 50 years. During that time, the quantity of data being collected and the amount of time needed to analyze these data has increased dramatically, and the quality of the data has improved remarkably as well. The increasing use of three-dimensional (3-D) seismic methods is an example of this. Using these methods, we have gained extraordinary new insights into the structure, stratigraphy, and rock properties of the subsurface, but a single 3-D survey may generate hundreds of gigabytes of data, which creates huge demands on the computing resources needed to process it properly. We recently developed a suite of four new seismic imaging methods, termed dual-domain methods (for space and wave-number domains), that attempt to address these issues.

To process seismic reflection data fully requires many steps, beginning with initial trace editing and ending with "imaging," or migration. Imaging is the most time-consuming step in the processing sequence, and for areas of complicated geological structure, it is the single most important step in the processing sequence. Imaging of a full 3-D survey may take many months, mainly because of the computing time required. Industry has recently explored for oil and gas in geological settings that are extremely difficult to image properly, such as subsalt areas, where 3-D seismic imaging is crucial. Subsalt imaging is difficult because of the large seismic velocity contrast between the salt body and the surrounding sediments. In addition, the generally irregular surfaces of salt bodies bend, reflect, and convert seismic waves in directions and ways that are almost unpredictable.

Unraveling the extreme effects that salt bodies can have on seismic waves as they go downward into the Earth and then return to the surface is the essential work done by the imaging step. The reliability of the resulting image depends on the quality of the seismic data and the reliability of the velocity model of the subsurface that is used. Unfortunately, defining the velocity model usually requires the results of the imaging. Thus, several iterations of improving the velocity model and running the imaging may be needed to get a reliable final image. Since a single imaging step may require months of computing to carry out, industry has devoted considerable resources to finding ways to speed up the imaging step.

All practical imaging methods use carefully chosen approximations to the exact imaging methods so they can run as fast as possible. Unfortunately, each approximation may also introduce inaccuracies into the resulting image. An important part of imaging research is to understand and evaluate the potential negative effects of the various approximations on the image. Test data sets, for which the proper image is known, are very important for understanding the effects of the imaging approximations.

The Kirchhoff imaging method is the fastest practical imaging method but involves the largest number of approximations. In spite of this limitation, it is the method most commonly used by the industry. Other imaging methods have been developed that are more reliable than Kirchhoff, but they can be so computing intensive that they are not practical for routine use. Our objective is to develop new imaging methods that fulfill two objectives: first, to produce more reliable images than the Kirchhoff method; and second, to keep the computing time required short enough to be practical.

In addition to developing higher-quality imaging methods, a crucial part of imaging research is to use seismic (forward) modeling to validate imaging methods and the velocity models they depend on. Researchers produce synthetic seismic data from specified structures, and the resulting synthetic data are then used to test and validate the imaging.

As with imaging, seismic modeling is an extremely computing-intensive procedure. Nevertheless, reliable, fast, and versatile seismic modeling is an essential part of testing and verifying imaging results and interpretations. Seismic modeling is also an increasingly important part of other aspects of seismic processing. With the increased use of three- and four-component data collection, the ability to carry out full 3-D elastic model calculations is increasingly important. Even with the fastest computers, 3-D elastic modeling is slow, and new, faster methods are needed to keep pace with the demands of the industry.

New Seismic Imaging Methods

Four new seismic imaging methods described below use slightly different approximations to the wave equation and are best suited to specific types of subsurface velocity fields. We named each of the four methods for the approximation they make to solve the wave equation: (1) Born, (2) Rytov, (3) quasi-Born, and (4) globally optimized Fourier finite-difference. The Born method assumes that lateral velocity perturbations are small in magnitude but may be abrupt in space. The Rytov method assumes that velocity perturbations are smooth but may be large in magnitude. The quasi-Born method adds a factor to the Born integral that improves the accuracy and the computational stability of the Born method. The increased stability allows use of a coarser computational grid, so fewer computing steps are needed, thus, the imaging is faster. Finally, the globally optimized Fourier finite-difference method is a hybrid method in which lateral derivatives of the wave field are computed in two parts—one is exact and the other has an approximation with relatively small error.

All four methods involve a recursive extrapolation of the recorded wave field downward into the Earth. The extrapolation at each depth step operates on the result of the previous depth step. The depth extrapolation is followed by an imaging step, which produces the image of the subsurface at the level of the current depth step. These imaging methods are almost as accurate as methods based on the full wave equation but require much less computer memory and are as much as 100 times faster.

Using these new imaging methods, we have successfully produced high-quality images of structures beneath salt bodies, which is an extremely challenging imaging situation. Figure 1 shows an example structure (top) and the image (bottom). The image was obtained with the globally optimized Fourier finite-difference method. In this case, the characteristics of the image are known exactly because it was generated from a synthetic data set. This figure shows what is arguably one of the best images ever obtained from this test data set, and many researchers have tested their imaging methods using it.

Improvements to the Kirchhoff Imaging Method

The Kirchhoff imaging method has been the imaging workhorse for the oil and gas industry for many years. It is much faster than other imaging methods, although it involves assumptions and approximations that often produce poorer images than those of other, slower methods. With the need to minimize time and cost, however, industry often finds that the slower methods are just not practical. Yet the images produced by conventional Kirchhoff migration are inadequate in complex geological structures. An essential part of the Kirchhoff method is computing the travel times of seismic waves along ray paths between every source and receiver. Conventional Kirchhoff imaging methods use fast, but simple, methods of computing the travel times. These methods provide excellent results in simple structures but rather poor results in more complicated structures, such as subsalt, where ray paths may be bent severely and cross other ray paths. Another major problem with

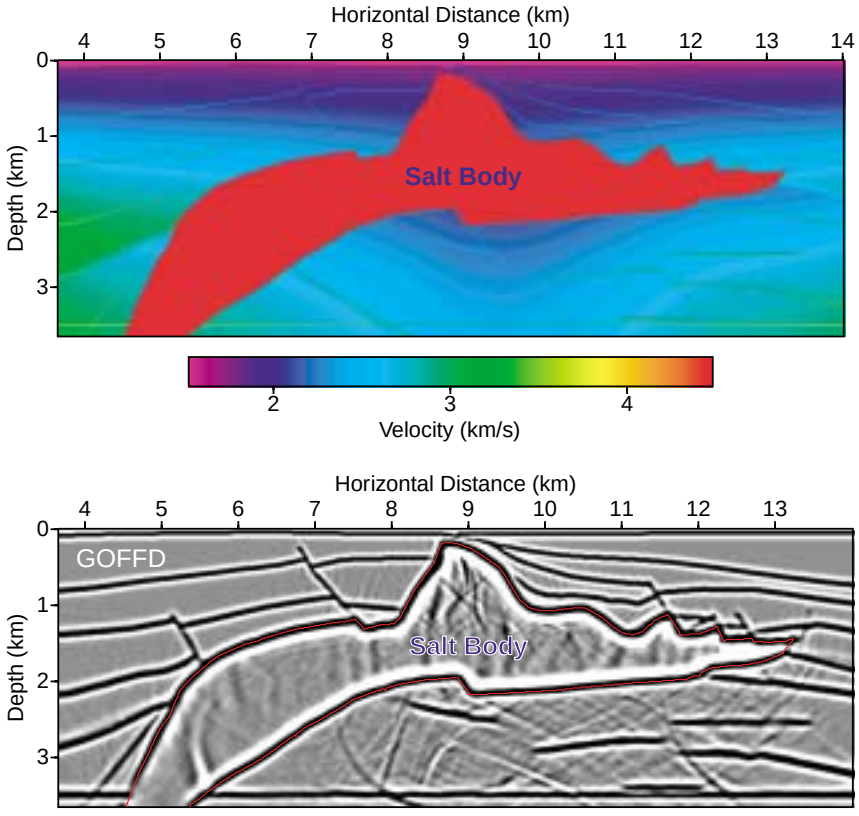

Figure 1. Image of a Salt Structure.
The top diagram is a 2-D vertical slice from a model of a hypothetical salt body. Note the extreme contrast in seismic velocity between the salt body and the surrounding sediments. Synthetic seismic data were computed from this model for testing imaging methods. The bottom panel is an image from a 2-D prestack migration of the synthetic data. This image was produced by the globally optimized Fourier finite-difference method and is an excellent image from this complicated structure.

conventional Kirchhoff imaging methods is that they exploit only first-arriving seismic waves. These waves may have followed such complicated ray paths that they only have small amplitudes and make minor contributions to the image.

To improve the imaging ability of Kirchhoff imaging methods and still retain their speed advantage, we have developed two techniques: wave-front construction and multiple-arrival Kirchhoff imaging. These techniques provide more reliable travel times and allow the use of multiple arrivals in the imaging. Although adding these techniques slows down the Kirchhoff imaging, it is still faster than other, more exact, imaging methods.

The new technique of wave-front construction provides a more robust method for computing travel times. The basic concept is that a wave front, composed of many individual seismic rays, is propagated through the velocity model, and travel times are computed from the advance of the entire wave front rather than from individual ray paths.

The propagation of the wave front is stable, even in velocity structures in which individual ray paths may shift drastically with only slight changes in their starting or ending positions. With more reliable travel times, the wave-front construction method produces better images from the Kirchhoff imaging method, particularly in complicated structures such as those beneath salt.

The second new technique addresses the problem of first arrivals being so small that they make little contribution to the image. In this situation, improving the image requires using the energy in several seismic arrivals. Multiple-arrival Kirchhoff imaging promises to produce better, more reliable, and more interpretable images from complicated structures. On the other hand, computing multiple travel times adds to the computational burden of Kirchhoff imaging. This method should still be fast enough so that it can be a practical imaging method, especially for getting initial images.

New Seismic Modeling Methods

At the opposite end of the spectrum of seismic reflection methods from imaging are seismic modeling methods. Using seismic modeling, one takes a known geological structure and computes the synthetic seismic response that would be recorded at specified sources and receivers. These forward methods are usually more precise than imaging methods and are crucial for testing imaging methods.

We devised two new seismic modeling methods that adapt the lattice-Boltzman microscale approach from fluid-flow modeling to simulate the physical processes of seismic wave propagation. These fully discrete methods can simulate all wave phenomena resulting from the complexity of a medium, using essentially no approximations. The methods simulate wave propagation through microscopic physical processes of the quasi particles that carry the wave field. These processes include transport between lattice nodes, reflection/transmission, and collisions.

The two new methods differ slightly in the way the quasi particles interact. They can accurately simulate wave propagation in media with sharp interfaces, strong contrasts in velocities, large topography, and viscosity/attenuation. In contrast, conventional finite-difference wave modeling methods require that the medium have only smooth changes in properties, which is often an unrealistically simplified view of the Earth. The lattice-Boltzman seismic modeling methods are also well suited for taking advantage of the currently available parallel computing systems. An example snapshot of a synthetic wavefield from one of the lattice-Boltzman modeling methods is shown in Figure 2. This figure illustrates the ability of the methods to model the topography at the surface of the model accurately and easily, which is difficult for finite-difference wave-equation modeling methods to do. The figure depicts a homogeneous velocity model (green background) with surface topography (the green and purple interface near the top of the figure). The calculated waves from a source at the middle of the figure are shown in red and purple. The circular wave front has reached the bottom of the model, from which there was no reflection because of the absorbing boundary condition on it. The wave front has nearly reached the sides of the models. The most interesting part of the figure is the interaction between the model waves and the topography, which has produced a complicated series of reflected waves and numerous multiples.

Project Collaborators

In addition to developing the new imaging and modeling methods discussed above, we are collaborating with researchers at Stanford University, the University of California at Santa Cruz, and the Lawrence Livermore National Laboratory to develop and test other methods for imaging and modeling. One new imaging method exploits the regular geometry of marine seismic data to make it faster. The method should be able to speed up wave-equation-based imaging by a factor of 10 or more yet still retain the inherently better-resulting image of wave-equation-based methods. The modeling method is a fully elastic 3-D method that effectively uses parallel computing to help speed up the calculations. It has been used and validated by many

oil and gas and service companies. The capabilities of the method are still being enhanced and improved.

In addition to the collaborators at Stanford University and the Lawrence Livermore National Laboratory, this work is being done as collaborations with companies from the oil and gas industry. The projects have more than two dozen collaborating companies. These collaborators provide guidance, insights, test data sets, new algorithms, and many hours of their own time to each project. The collaborations have been essential to the success of the research projects. The industry collaborations, which continued even through the most recent down-cycle in the industry, demonstrate the high level of interest by industry in this research and underscore the importance of the substantial contributions the projects have made in seismic imaging and modeling.

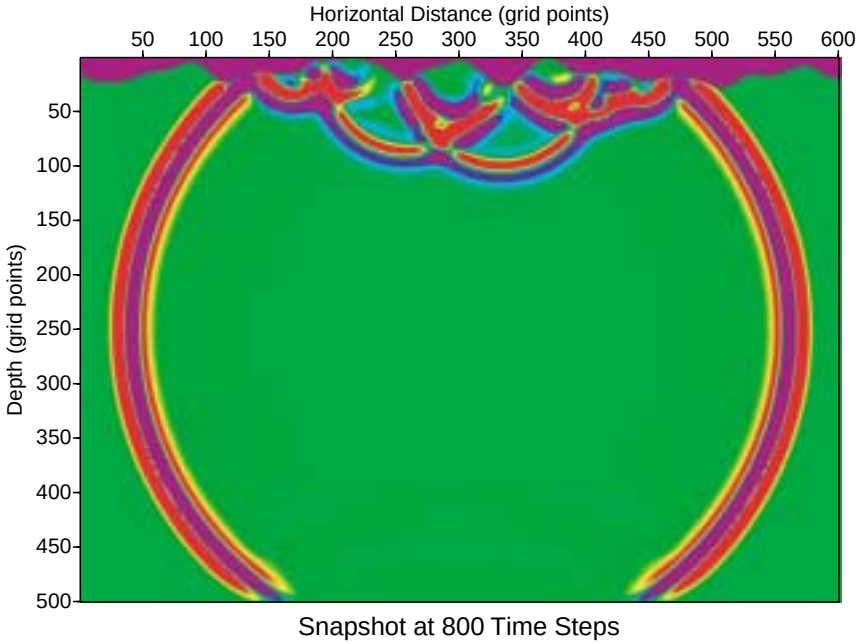

Figure 2. Lattice-Boltzmann Modeling.
The figure is a 2-D slice of a wave-propagation simulation in a homogeneous velocity medium (indicated by the green background color) with large surface topography. The surface topography is the irregular interface between the blue and green materials. This is a situation that is difficult to model properly using conventional finite-difference methods. It was successfully modeled with the lattice-Boltzmann modeling method.

Conclusions

We have developed several new methods for imaging seismic reflection data that have significant advantages compared to conventional imaging methods. These advantages include substantially reduced computing requirements with little or no degradation of the final image.

We have also developed new methods for more accurately computing synthetic seismic data. These can also be used to compute synthetic data from subsurface models that are beyond the abilities of conventional modeling methods. Accurate imaging and modeling methods are crucial for making maximum use of large 3-D seismic data sets. ■

Further Reading

Fehler M., H. Sato, L.-J. Huang. 2000. Envelope broadening of outgoing waves in 2D random media: A comparison between the Markov approximation and numerical simulations. *Bulletin of the Seismological Society of America* **90**: 914–928.

Fehler, M., L.-J. Huang, D. Alde, S. Hildebrand, and C. Burch. 1998. Comparison of images obtained from a 2D Gulf of Mexico subsalt dataset using different migration approaches. *Expanded Abstracts, Society of Exploration Geophysics, 1998 Annual Meeting*.

Huang L.-J., P. Mora, M. C. Fehler. 2000. Absorbing boundary and free-surface conditions in the phononic lattice solid by interpolation. *Geophysical Journal International* **140**: 147–157.

Huang L.-J., and M. C. Fehler. 2000. Quasi-Born Fourier migration, *Geophysical Journal International* **140**: 521–534.

Huang, L.-J., M. C. Fehler, P. M. Roberts, and C. C. Burch. 1999. Extended local Rytov Fourier migration method, *Geophysics* **64**: 1535–1545.

Huang, L.-J., M. C. Fehler, and R.-S. Wu. 1999. Extended local Born Fourier migration method. *Geophysics* **64**: 1524–1534.

Huang L.-J., and M. C. Fehler. 1998. Accuracy analysis of the split-step Fourier propagator: Implications for seismic modeling and migration. *Bulletin of the Seismological Society of America* **88**: 18–29.

Roberts, P., L.-J. Huang, C. Burch, M. Fehler, and S. Hildebrand. 1997. Prestack depth migration for complex 2D structure using phase-screen propagators. *Expanded Abstracts, Society of Exploration Geophysics, 1997 Annual Meeting*, p. 1282.